STRUCTURE AND MAGNETISM OF Mn-DOPED Si THIN FILMS GROWN BY MOLECULAR BEAM EPITAXY

by

Samer C. Kahwaji

Submitted in partial fulfillment of the requirements
for the degree of Doctor of Philosophy

at

Dalhousie University
Halifax, Nova Scotia
April 2013

© Copyright by Samer C. Kahwaji, 2013

DALHOUSIE UNIVERSITY

DEPARTMENT OF PHYSICS AND ATMOSPHERIC SCIENCE

The undersigned hereby certify that they have read and recommend to the Faculty of Graduate Studies for acceptance a thesis entitled "STRUCTURE AND MAGNETISM OF Mn-DOPED Si THIN FILMS GROWN BY MOLECULAR BEAM EPITAXY" by Samer C. Kahwaji in partial fulfillment of the requirements for the degree of Doctor of Philosophy.

Dated: April 17, 2013

External Examiner: Dr. Andrea Damascelli

Research Supervisor: Dr. Theodore Monchesky

Examining Committee: Dr. Kimberley Hall

Dr. Ian Hill

Departmental Representative: Dr. Ian Folkins

DALHOUSIE UNIVERSITY

DATE: April 17, 2013

AUTHOR: Samer C. Kahwaji

TITLE: STRUCTURE AND MAGNETISM OF Mn-DOPED Si THIN FILMS GROWN BY MOLECULAR BEAM EPITAXY

DEPARTMENT OR SCHOOL: Department of Physics and Atmospheric Science

DEGREE: Ph.D. CONVOCATION: October YEAR: 2013

Permission is herewith granted to Dalhousie University to circulate and to have copied for non-commercial purposes, at its discretion, the above title upon the request of individuals or institutions. I understand that my thesis will be electronically available to the public.

The author reserves other publication rights, and neither the thesis nor extensive extracts from it may be printed or otherwise reproduced without the author's written permission.

The author attests that permission has been obtained for the use of any copyrighted material appearing in the thesis (other than brief excerpts requiring only proper acknowledgement in scholarly writing), and that all such use is clearly acknowledged.

Signature of Author

To Pauline

Table of Contents

List of Tables

List of Figures

Abstract

The structure and magnetism of ultrathin Mn layers grown by molecular beam epitaxy (MBE) on Si(001) are investigated. X-ray absorption fine structure (XAFS) shows that a metastable MnSi phase with a B2-like (CsCl) crystal structure forms and superconducting quantum interference device (SQUID) magnetometry measurements reveal that the B2 structure is ferromagnetic with a Mn moment of 0.33 μ_B and a Curie temperature $T_C > 400$ K. A change in the Si capping layer growth temperature, T_{Si}, produces a MnSi phase with a B20-like structure, which exhibits a small moment and a T_C below 20 K.

Surfactant mediated growth of Mn δ-doped Si films and co-deposited $Si_{1-x}Mn_x$ alloys shows that a Pb surfactant strongly alters the structure and magnetism of these systems. For the δ-doped films, analysis of the crystal structure and magnetic properties over a range of growth parameters identified three distinct Mn-Si phases. With Pb, a sample with a coverage $\theta_{Mn} = 0.26$ monolayer (ML) and $T_{Si} = 200$ °C develops a ferromagnetic phase with a Mn moment of 1.56 μ_B and a $T_C > 400$ K, whereas T_C drops to zero for a sample grown without Pb. For $T_{Si} > 200$ °C, nano-disks with MnSi-B20 type structure form with a $T_C \approx 170$ K. A possible correlation exists between the remanent moment and the fraction of Mn occupying Si substitutional sites, which suggests that a dilute $Si_{1-x}Mn_x$ may be forming in the matrix. Density functional theory (DFT) shows that Pb lowers the formation energy of Si vacancies by 0.92 eV, which enhances the substitutional incorporation of Mn.

In the absence of Pb, the co-deposited $Si_{1-x}Mn_x$ films undergo a 2D spinodal decomposition and form nanocolumns. The nanocolumns are amorphous and paramagnetic. In contrast, in the samples grown with Pb, $MnSi_{1.7}$ nanorods form in the plane of the films and exhibit two ferromagnetic transitions at $T_{C1} \approx 40$ K and $T_{C2} > 400$ K when $x = 0.5\%$. While T_{C1} is consistent with T_C of bulk $MnSi_{1.7}$ crystals, T_{C2} is believed to originate from Mn diluted in the Si matrix.

List of Abbreviations and Symbols Used

A_{Mn-Mn}	area under the Mn-Mn profile function
$B_j(x)$	Brillouin function
E	incident x-ray energy
E_0	energy of the core electron
E_t	energy of target atoms (RBS)
E_{i0}	energy of incident ions (RBS)
E_{i1}	energy of backscattered ions (RBS)
$F_i(k)$	effective scattering amplitude
H	applied magnetic field
H_c	coercive field
H_{sat}	saturation magnetic field
I_0	incident intensity
I_F	fluorescence intensity
K	kinematic factor
K_a	magnetic anisotropy energy density
M_i	mass of incident ions (RBS)

M_t	mass of target atoms (RBS)
N_d	number of data points
N_i	coordination number of a given shell
N_{Ip}	number of independent datapoints
$R(\%)$	percent residual
R_i	coordination distance of a given shell
$S(E)$	stopping power
S_0^2	amplitude reduction factor
T	temperature
T_B	blocking temperature
T_C	Curie temperature
T_N	Néel temperature
T_g	growth temperature
T_{Si}	Si cap growth temperature
U	Coulomb interaction
V	volume of nanoclusters
ΔR	data range in R-space

$\Delta\mu(E_0)$	height of step edge
Δk	data range in k-space
$\boldsymbol{G}$	reciprocal lattice vector (RHEED)
$\boldsymbol{k'}$	diffracted wavevector (RHEED)
$\boldsymbol{k_0}$	incident wavevector (RHEED)
$\chi(E)$	EXAFS function in terms of energy
$\chi(k)$	EXAFS function in terms of wavenumber
χ^2	goodness of fit parameter
χ_D	diamagnetic susceptibility
$\eta_d(\epsilon_F)$	density of d-states at the Fermi level
$\hbar$	Plank constant/2π
$\lambda(k)$	mean free path parameter
$\mu(E)$	x-ray absorption coefficient
$\mu_0(E)$	x-ray absorption coefficient of an isolated atom
μ_0	permeability of free space
μ_B	Bohr magneton
μ_{B2}	magnetic moment of Mn in MnSi-B2 structure

μ_{Mn}	Mn saturation moment
μ_{Si}	chemical potential of Si
μ_{sub}	magnetic moment of substitutional Mn
σ_i^2	mean square relative displacement
σ_{exp}	experimental error
τ_0	attempt time
τ_m	measurement time
θ_{Mn}	Mn coverage
$\varphi(k)$	phase shift
a_{Si}	Si lattice constant
g	Landé factor
h_{epi}	critical epitaxial thickness
j	total angular momentum quantum number
k	wavenumber
k_B	Boltzamnn contant
m	magnetic moment
m_e	electron mass

m_r	remanent moment
m_{sat}	saturation moment
x_t	distance traveled by incident ions before collision
x_{sub}	fraction of substitutional Mn
y_{exp}	experimental data point
y_{th}	theoretical data point
E(formation)	formation energy
E(reference)	total energy of Si slab
E(vac)	total energy of Si slab with one atom removed
E	electric field vector
AES	Auger electron spectroscopy
AFM	atomic force microscopy
CMS	condensed magnetic semiconductor
DFT	density functional theory
DI	deionized water
DMS	dilute magnetic semiconductor
DRS	diffuse reflectance spectrometer

EDX	Energy dispersive x-ray spectroscopy
EXAFS	extended x-ray absorption fine structure spectroscopy
FLAPW	full potential linearized augmented plane wave
FM	ferromagnetic
FT	Fourier transform
GAD	glancing-angle detector
GMR	giant magnetoresistance
HARPES	hard x-ray angle-resolved photoemission spectroscopy
HM	helical magnet
ID	insertion device
ip	in-plane
MBE	molecular beam epitaxy
ML	monolayer
Mn_{int}	interstitial Mn
Mn_{Si}	Mn in Si substitutional lattice site
$Mn_{channel}$	Mn concentration from channel RBS orientation
Mn_{random}	Mn concentration from random RBS orientation

MPMS	Magnetic Property Measurement System
MRAM	magnetic random access memory
oop	out-of-plane
$Pb_{channel}$	Pb concentration from channel RBS orientation
Pb_{random}	Pb concentration from random RBS orientation
PBE	projected augmented wave
PNC/XSD	Pacific Northwest Consortium/X-ray Science Division
RBS	Rutherford backscattering spectrometry
RHEED	reflection high energy electron diffraction
RSO	reciprocating sample option
SADP	selected area diffraction pattern
SIMS	secondary ion mass spectrometry
SLD	scattering length density
SQUID	superconducting quantum interference device
STM	scanning tunneling microscopy
TEM	transmission electron microscopy
TM	transition metal

TMR	tunneling magnetoresistance
UHV	ultra high vacuum
UPS	ultraviolet photoemission spectroscopy
WAD	wide-angle detector
XAFS	x-ray absorption fine structure
XANES	x-ray absorption near edge spectroscopy
XPS	x-ray photoelectron spectroscopy
XRR	x-ray reflectometry
XSTM	cross-sectional scanning tunneling microscopy

Acknowledgements

I would like to express my deepest gratitude to my supervisor Prof. Theodore Monchesky for giving me the chance to work on this project and for his guidance and encouragement over the last years. Through our discussions and the many opportunities he gave me to collaborate with other physicists, I surely have benefited a lot on both the academic and personal levels. I am also thankful to my thesis committee members, Prof. Kimberley Hall and Prof. Ian Hill for their valuable advices and suggestions.

It has been a great experience getting to meet and work with Dr. Robert Gordon and Prof. Daryl Crozier. I am grateful to all their support during my trips to the Advanced Photon Source and for teaching me a lot about XAFS. It was also a pleasure to work with Prof. Michael Robertson and his students at Acadia University and I thank them for all the hard work in measuring and analyzing my samples with TEM. I also thank Prof. Manfred Jericho for assisting with the AFM imaging, Prof. Sjoerd Roorda at Université de Montréal for conducting the RBS measurements and Dr. Junyi Zhu at the National Renewable Energy Laboratory for performing the DFT calculations. I also gratefully acknowledge the technical support of Kevin Borgel and Andy George. My special thanks go to my colleagues at the MBE lab, Murray Wilson, Dr. Eric Karhu and Dr. Zeynel Bayindir, who left good memories.

Above all, I am greatly indebted to my wife Souad. I cannot thank her enough for all the support, care and love she has provided me. I am also deeply grateful to my parents Georgette and Camille, my brother Chadi and his family, my brother Fadi, and my sister Pauline for their continuous love and encouragement.

My commitment to this project prevented me from spending more time with my sister and being on her side when she needed it the most. I dedicate this thesis to her.

Chapter 1

Introduction

1.1 Overview

Since the discovery of giant magnetoresistance (GMR) effect by Albert Fert [1] and Peter Grünberg [2] in the late 1980's, the emerging field of spintronics has radically transformed modern technology. In addition to the charge, spintronics manipulates the spin of the electron to sense, process and transmit information. Ten years after the discovery, IBM launched the first hard drive that uses GMR in a spin-valve read head, enabling a great improvement of data storage technology with more than 1000-fold increase in magnetic hard disk drive storage capacity in three years [3]. In another spintronic application, the tunneling magnetoresistance effect (TMR) produced in magnetic tunnel junctions is used to create a magnetic random access memory (MRAM). MRAM promises an improved performance over conventional semiconductor RAM owing to its higher speed, higher density and non-volatility. At present, TMR sensors are also used in all hard drive read heads. Both spintronic applications use spin-valves and magnetic tunnel junctions fabricated with metal-based layered structures, using elements such as Fe. However, spintronics would have an even greater impact if the spin functionalities could be integrated into semiconductors. Spintronic semiconductors open the opportunity for entirely new applications with low-power, high-speed multifunctional devices that combine electronics, photonics and magnetism in a single chip. The possible development of a spin transistor as described by Datta and Das [4] and the development of spin-optoelectronic devices such as the spin-polarized LEDs [5] demonstrate potential examples of such integration.

The efforts to produce robust spin polarization in semiconductors has largely focused on two different approaches [6, 5, 7]. The first method injects spin by passing an electrical current from a metal layer grown onto the semiconductor. This system requires materials that have a minimal lattice mismatch in order to overcome the structural instability that weakens the spin-polarization at the interface [8]. Interfacial intermixing and the large conductivity mismatch between the metal-semiconductor are also key issues that limit the efficiency of spin injection in this system. In the second method, the semiconductor is turned ferromagnetic by doping with a few atomic percent of a $3d$ transition metal (TM). Depending on the structure that results from the doping process, two distinct classes of ferromagnetic semiconductors can be identified. Dilute magnetic semiconductors (DMS) belong to the first class, where dilute amounts of TM impurities randomly substitute for semiconductor atoms in the lattice. In the second class, the magnetic impurities react with the semiconductor to form nanometer-sized ferromagnetic precipitates that distribute within the host. A system where the precipitates contain a relatively large concentration of magnetic ions is commonly described as condensed magnetic semiconductor (CMS) [9]. Although more studies focus on the growth of homogenous (precipitates-free) DMS and on ways to increase their generally low T_C's, the nanocrystalline precipitates are interesting in their own right and proved to be useful for applications [10, 11, 12], especially since they can induce a ferromagnetic order with a T_C exceeding room temperature. The interest in DMS stems from the nature of their ferromagnetic coupling, which is mediated by free carriers. In GaAs, for example, a substitutional $3d$ element such as a Mn on a Ga site, gives rise to a local moment with $S = 5/2$ while simultaneously doping the semiconductor with holes due to its lower valence. For a Mn concentration of a few percent, enough holes are generated to mediate an exchange coupling between the local moments. The higher the hole density, the stronger the exchange coupling

and, consequently, the higher the T_C. Carrier-mediated magnetism is fundamental to achieve electrical or optical manipulation of ferromagnetic states in a semiconductor or, alternatively, to control the electrical current by a magnetic field. This property makes DMS promising for the development of novel materials that combine data processing and storage capabilities and for the development of qubit devices that could be used in quantum computing. For instance, promising results on the persistence of spin coherence, a major requirement for qubit operations, were reported for Mn-doped magnetic semiconductor quantum wells [13] and the optical control of the Mn spin states in group II-VI quantum dots have been experimentally demonstrated [14, 15]. Increasing the hole density in DMS is, however, hampered by the low solubility of the $3d$ metal under equilibrium conditions. For GaAs, the equilibrium solubility limit of Mn is 0.1% [16], whereas theoretical models predict that a Mn concentration of 10% is needed for T_C to reach room temperature [17]. In Ge and Si, the solid solubility limit of Mn is also well below 1% [8, 18].

To overcome the thermodynamic solubility limit, non-equilibrium growth techniques such as ion implantation, sputtering and low-temperature molecular beam epitaxy (MBE) have been used effectively. An important difference between MBE and sputtering or ion implantation is the low energy of the evaporated atoms. This enables the growth of higher quality interfaces. In MBE, the growth normally takes place under ultra high vacuum conditions (base pressure $< 10^{-9}$ Torr) and elementary processes, such as surface diffusion, desorption and nucleation, that govern the growth mode and the incorporation of impurities can be indirectly controlled by varying the growth parameters. These parameters include the flux rate, the substrate temperature and the crystallographic orientation or lattice constant of the substrate. In the early 1990's, MBE led to the successful growth of ferromagnetic $In_{1-x}Mn_xAs$ and $Ga_{1-x}Mn_xAs$ by incorporating a Mn concentration of up to 5% [19, 20, 21]. These experiments triggered an intensive research effort on DMS based on these materials,

driven by their compatibility with a group of semiconductors that are widely used in device applications and as models to study the fundamental physics of ferromagnetic semiconductors.

In most DMS studies, Mn is dominantly chosen as the magnetic dopant due to its half-filled $3d$ shell, which gives an isolated Mn atom a magnetic moment of 5 Bohr magneton (μ_B), the largest among the transition metals. A large moment favors a strong exchange interaction and a high T_C. Manganese was also shown to have a more uniform doping in semiconductors with a lower clustering rate and higher ability of substitutional incorporation relative to other $3d$ metals such as Cr and Fe [22].

DMS based on group III-V and II-VI elements have been extensively studied over the last two decades (see Ref. [16] and the publications database [23]). Increasing the T_C beyond the current record of 185 K (in $Ga_{1-x}Mn_xAs$) [24] remains a major obstacle for this system. Surprisingly, less progress has been achieved in the technologically important group IV DMS despite the mean-field theory predictions of a high T_C in Mn doped Si [25] and the works of Park [26] and Li [27] and their coworkers on ferromagnetic Mn_xGe_{1-x} with a T_C up to 114 K. Group IV elements not only provide a simpler model for the study of fundamental theory of DMS, but there is also a greater technological advantage if a Si-based DMS can be realized, given the prevalence of Si in the semiconductor industry. Silicon is also interesting because its low spin-orbit coupling enhances the spin coherence time and length [8, 22], which is an important requirement for spin-based quantum computing [28].

One of the reasons that little attention has been given to Si-based DMS is that a homogenous substitutional incorporation of Mn in Si is hard to achieve. This is related to the behavior of Mn in bulk Si where, unlike the case of Ge and GaAs, Mn does not favor substitutional sites but rapidly diffuses into tetrahedral interstitial sites [29]. The phase diagrams of Mn-Si and Mn-Ge [30, 31] are also different and show that there are many more Si-rich Mn-Si phases as compared to Ge-rich Mn-Ge phases,

which makes a $Si_{1-x}Mn_x$ more difficult to achieve than $Ge_{1-x}Mn_x$. Density functional theory (DFT) also predicts that it is energetically more favorable for Mn to occupy subsurface interstitial sites when grown on a Si(001) surface [18, 32]. Interstitial Mn is not desirable for DMS since it acts as a donor and leads to carrier compensation and precipitate formation. On the other hand, the high temperature required for MBE growth of Si (as high as 600 °C), or the post-growth annealing of sputtered and ion-implanted Mn_xSi_{1-x} alloys, drives the system toward the thermodynamically stable phases [33, 34]. Mn-rich precipitates also contribute to carriers compensation and when nonmagnetic or metallic phases form, their presence can be detrimental to the ferromagnetic and semiconducting character of a DMS. However, numerous studies reported on intriguing properties in precipitate-rich samples. In the case of Mn-doped Ge, Mn-rich nanocolumns form with an above room temperature T_C and a large magnetoresistance [35], whereas the $MnSi_{1.7}$ nanocrystallites that form in Mn_xSi_{1-x} samples have been proposed to be the origin of ferromagnetic ordering with a $T_C > 400$ K [36, 33, 37, 38], even though bulk $MnSi_{1.7}$ has a $T_C \simeq 45$ K [39]. More recently, this interpretation was brought into question [34].

Nearly all experimental attempts to create a Mn-doped Si DMS reveal phase separation or clustering of magnetic dopants. Reducing the unwanted precipitates while at the same time increasing substitutional Mn and preserving the crystalline quality of Si is still a challenging task. Hence, whether a homogenous Si DMS can be realized remains an open question. On the other hand, an understanding of how to control the phase, size and distribution of nanocystallites is also important to be able to exploit their properties in functional FMS materials, and to assist the theoretical studies that are trying to explain the origin of their high T_C. Overall, these two issues call for novel approaches to control the Mn incorporation in Si, which is the main focus of this thesis. In particular, this thesis explores how the growth of metastable phases, δ-doping and surfactant-mediated growth can provide new directions to control the Mn

incorporation and precipitates formation in Si. A combination of x-ray absorption fine structure (XAFS), transmission electron microscopy (TEM), Rutherford backscattering spectrometry (RBS) and superconducting quantum interference device (SQUID) magnetometry techniques are employed to study the correlation between growth parameters, structure and magnetism of Mn-doped Si layers and Mn_xSi_{1-x} alloys grown by MBE.

In the following section, I present an overview of the Si:Mn system in the dilute doping limit and of the growth on the Si(001) surface. This is followed by a brief description of δ-doping and surfactant mediated growth techniques. I conclude this chapter with an outline of the thesis.

1.2 Magnetism and Structure of the Si:Mn System

1.2.1 Ferromagnetic Coupling in Homogeneous DMS

The mechanism behind the ferromagnetic coupling in Mn-doped Si DMS is generally discussed in the context of the models developed to explain the magnetism in (Ga,Mn)As, since (Ga,Mn)As is the best understood DMS. The availability of a homogeneous (Ga,Mn)As alloy makes the interpretation of experimental studies of this system easier, in contrast to (Ge,Mn) and (Si,Mn) where the presence of inhomogeneities obscures some of the underlying physics. Although the fundamental mechanisms governing the ferromagnetic behavior may differ in group IV DMS, the global picture discussed here remains relevant to these systems.

The magnetism in TM-doped semiconductors depends on the interaction between the *d*-shells of the impurities and the valence and conduction bands of the host atoms. Dietl et al. [25] proposed the kinetic exchange mechanism based on the Zener model of ferromagnetism in transition metals [40] to explain this interaction. According to

the proposed model, the localized magnetic moments introduced by Mn atoms occupying substitutional sites interact with the spins of the free carriers through a $sp-d$ orbital hybridization. In the case of GaAs, Ge and Si, the free carriers are holes generated in the valence band of the semiconductor by Mn, which acts as an acceptor in these hosts [16, 8]. The hybridization with the d-shell of the magnetic ions leads to a spin-polarization of the carriers surrounding the localized moments [25, 16]. The spin-polarized carriers then mediate an indirect and long-range interaction between the impurities spins, which also assume a ferromagnetic alignment. In the absence of free carriers, and provided that the electrons in the d-shell remain localized, a superexchange interaction between the open d-shells of Mn favors an antiferromagnetic configuration. Therefore, for a given Mn concentration and hole density, the magnetic signature of the system depends on a competing process between the direct Mn-Mn antiferromagnetic coupling and the indirect hole mediated ferromagnetic interaction. DFT calculations of Mn_xGe_{1-x} and the experimental results reported in Ref.[26] show a strong antiferromagnetic coupling between nearest-neighbors Mn and a weak ferromagnetic coupling beyond nearest-neighbors distance, which supports the existence of a competing mechanism.

The $sp-d$ kinetic exchange model explains many aspects of DMS and successfully calculates the T_C of $Ga_{1-x}Mn_xAs$ and that of $Zn_{1-x}Mn_xTe$ [25] and interprets many experimental results (see discussion in [41] and references therein). However, there is still a controversy about the itinerant character of the carriers and it has been shown that the spin-spin coupling depends on the density of the free carriers relative to that of magnetic impurities. Li et al. [27] interpret the ferromagnetism in Mn_xGe_{1-x}, where $0 < x < 0.09$, to be due to localized carriers moving in the impurity band and forming a magnetic polaron with the Mn spins. In this picture, holes tightly bind to the spins of Mn ions to form a bound magnetic polaron. The radius of the polaron increases when the temperature is decreased and a ferromagnetic transition

occurs when the individual polarons overlap at T_C [8, 42]. Bound magnetic polarons are generally the accepted model of the ferromagnetism in the highly dilute limit or when the density of carriers is low [16, 41, 8, 43], such as in the case of insulating Mn_xGe_{1-x} samples [27].

A comprehensive work conducted by Stroppa et al. [44] using full potential linearized augmented plane wave (FLAPW) method of DFT is consistent with the picture described above. The calculations show that substitutional Mn is a source of holes in Si and that it assumes a local magnetic moment of 2.75 μ_B, which is less than the value of 5 μ_B expected for one Mn atom, due to a strong $p-d$ hybridization. The results also show that the system favors a ferromagnetic state which becomes more stable with increasing Mn content.

However, the first-principles calculations of Ref. [45] showed that interstitial Mn could also induce ferromagnetism in a dilute system. In contrast to most DFT studies, the cited work was not restricted to a model with homogeneous substitutional distribution of Mn, but also explored other configurations. This study determined that the most energetically stable configuration is an ensemble consisting of 2 tetrahedral-interstitial and one substitutional Mn atoms. This configuration results in a dominant ferromagnetic state.

Beyond the dilute regime, in CMS systems where nanocrystals with a high concentration of magnetic dopants form in a semiconducting matrix, the mechanisms of ferromagnetic coupling are not well understood. Besides the $sp-d$ Zener model, superexchange and double exchange interactions between neighboring ions become possible [9]. Stoner-type ferromagnetism is also likely to occur if the d-band electrons of the TM delocalize due to the short distance between the atoms in a nanocluster [9]. Given that parameters like the phase and structure of the nanocrystals enter into play, the origin of ferromagnetism becomes highly system-dependent.

1.2.2 Magnetism in Grown Si:Mn Structures

The overwhelming majority of experimental studies using different growth techniques report phase separation in Si:Mn samples. However, the observation of a $T_C > 400$ K in sputtered Mn-doped Si [46] and in Si ion-implanted with 0.1% and 0.8% atomic concentrations of Mn [33] motivated the search for the origin of ferromagnetism in these structures. The report of $T_C > 400$ K is surprising given the low T_C of all known bulk Mn-Si phases, which include Mn_3Si, an antiferromagnet (AF) with a Néel temperature $T_N = 23$ K [47], Mn_5Si_3 (AF, $T_N = 99$ K) [48], MnSi, which is a helical magnet (HM) with $T_C = 29.5$ K [49] and the higher manganese silicide $MnSi_{1.7}$ family (HM, $T_C \simeq 45$ K) [50, 39]. Later studies that employed high resolution structural characterization techniques, including electron diffraction, TEM and synchrotron source x-ray diffraction, revealed that $MnSi_{1.7}$ is the most common phase of precipitates that form in these samples [36, 37, 34], as expected from the Mn-Si phase diagram. The magnetism in these samples is sensitive to the preparation conditions [37] and has been suggested to be due to the presence of Mn impurities in the $MnSi_{1.7}$ phase [51]. A more comprehensive model was recently proposed by Men'shov et al. [38]. Their study explains the ferromagnetism in terms of local moments on Mn defects inside the precipitates that are coupled through spin-fluctuations in the weakly itinerant $MnSi_{1.7}$ ferromagnet. Moreover, the model assumes that the high concentration of local moments that also exist at the boundary between the precipitates and the Si matrix contribute to the enhancement of the ferromagnetic order. The latter model plausibly explains the discrepancy between the measured values of the magnetic moment, up to 5 μ_B in ion implanted samples [33], and that of Mn in $MnSi_{1.7}$, which is close to 0.012 μ_B [39]. Through first-principles calculations, Yabuuchi et al. [52] showed that the boundary between $MnSi_{1.7}$ and Si, as well as the strain and the fluctuations in the stoichiometry, significantly influence the magnetic properties of

these nanoparticles and account for the inconsistency with experimental observations. Another interpretation suggests that carrier-mediated ferromagnetism is due to Mn impurities in the Si matrix that surrounds the precipitates and is responsible for the high T_C [34]. Since DFT predicts that either substitutional or interstitial Mn will have a moment of 3 μ_B [44, 53, 38], a $Si_{1-x}Mn_x$ DMS matrix would be expected to contribute a significant fraction to the total magnetic moment of $MnSi_{1.7}$-containing samples, given the moment in bulk $MnSi_{1.7}$ of only 0.012 μ_B [39].

Extensive theoretical studies investigated the initial growth mode, structures and magnetism of Mn on Si(001) as a function of Mn coverage in a range from 0.25 to 3 monolayers (ML) [32, 54, 55]. DFT calculations found that a metastable MnSi with a tetragonally distorted B2 (CsCl) crystal structure is energetically more favorable on Si(001) than a B20 crystal structure, which is the stable bulk phase of MnSi, owing to a lattice mismatch of only 2% as opposed to 16% for MnSi-B20/Si(001) (Fig. 1.1). The 2% lattice mismatch is the same as that observed experimentally for FeSi-B2 and CoSi-B2 stabilized on Si(111) [56, 57]. It is understood that the MnSi-B2 structure is created from Mn diffusing to its preferred subsurface sites where it forms a CsCl-type coordination with the neighboring Si atoms. Interestingly, thin films of MnSi-B2/Si(001) were predicted to be ferromagnetic, with a T_C reaching 328 K and a Mn moment varying between 1.11 μ_B (Mn in inner layer) and 1.90 μ_B (Mn in interfacial layer) for a 2 ML MnSi-B2/Si(001) [55]. This MnSi-B2 structure was not reported in any of the ion implanted or sputtered Si:Mn samples.

1.2.3 Mn Incorporation in Si

The electronic and magnetic properties of Mn doped Si are highly dependent on the Mn distribution in the Si host and on their local environment, which in turn are manipulated by the growth conditions. Several theoretical studies that employed DFT methods to address the issue of Mn incorporation in Si found that Mn prefers the

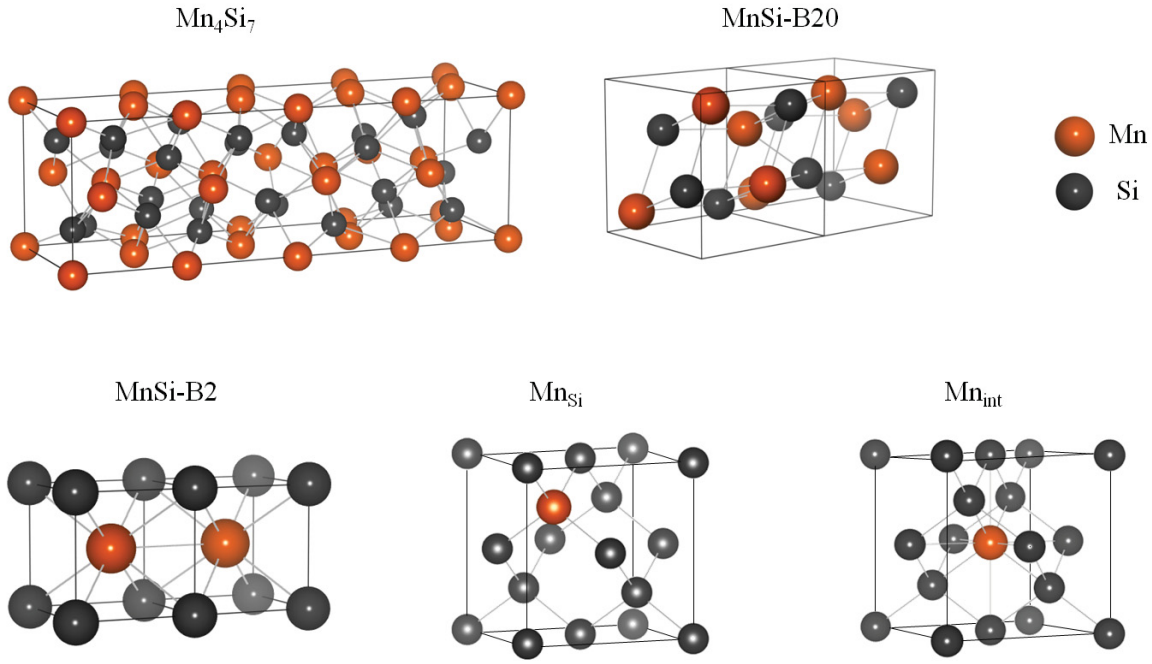

Figure 1.1: The different crystal structures of MnSi discussed in this thesis. Substitutional (Mn_{Si}) and tetrahedral-interstitial (Mn_{int}) Mn in a Si lattice are also shown. Mn_4Si_7 has a tetragonal structure with lattice constants $a = 5.526$ Å and $c = 17.516$ Å [39], and MnSi-B20 is a cubic structure with $a = 4.560$ Å [58]. The metastable MnSi-B2 is a cubic structure (CsCl) with an estimated lattice parameter $a = 2.715$ Å. A tetragonally distorted MnSi-B2 is predicted to grow on Si(001) [55].

tetrahedral interstitial site (Fig. 1.1), which is also the subsurface site below a Si dimer of the Si(001) surface [59, 60, 32, 54, 61]. It has been shown that this preferred incorporation is due to chemical and not volume effects [62]. Scanning tunneling microscopy (STM) studies of 0.1 ML Mn/Si(001) annealed between 300 °C and 700 °C confirmed that Mn occupies subsurface sites [63]. On the other hand, some calculations demonstrated that Mn can be driven into Si substitutional sites in the presence of a strain field [64, 61] or by co-doping the Si with a n-type impurity [65]. However, according to Ref. [66], it is in principle possible to create a DMS in Si with interstitial Mn.

X-ray absorption fine structure (XAFS) is one technique that has been used effectively to elucidate the local environment of Mn atoms in Si. XAFS measurements on cosputtered $Si_{1-x}Mn_x$ found that Mn incorporates into Si substitutional sites for x up to 0.08 where it coordinates to 4 Si nearest-neighbors located at 2.35 Å [67]. Note that the simulation of the XAFS spectra in this study was limited to the first shell. However, XAFS spectra of the Mn ion-implanted samples of Ref. [68] did not show evidence for substitutional Mn. Instead, Mn in these samples is found in a cluster with a disordered MnSi-type structure where it has 5 to 8 Si nearest-neighbors, depending on the implantation conditions. Moreover, the analysis of XAFS spectra in Ref. [51] revealed a local coordination reminiscent of $Mn_{15}Si_{26}$ structure (a member of the $MnSi_{1.7}$ family of phases). Rutherford backscattering spectrometry (RBS) used in channeling mode is another technique that has been employed to reveal the localization of Mn in Si by measuring the fraction of substitutional atoms [69, 70, 37].

The initial growth stages of Mn are inferred from STM studies. For submonolayers of Mn deposited on Si(001) at room temperature, Mn atoms organize in monoatomic nanowires [71, 72, 73] that appear to nucleate at vacancies on the Si surface [74]. At higher Mn thicknesses, MnSi nanocrystallites with various microstructures and phases

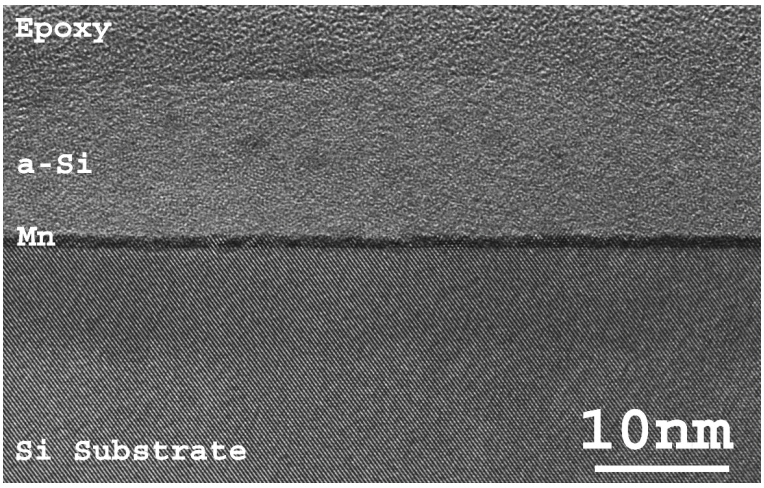

Figure 1.2: Cross-section of a Mn delta-doped Si layer prepared by MBE and imaged with a high resolution transmission electron microscope.

are commonly reported. The MBE growth of 1 and 1.5 ML of Mn at room temperature produces a disordered structure [75]. After annealing at 450 °C and 480 °C, STM images show a bimodal growth of MnSi-B20 and Mn_5Si_3 crystallites described as pancake-stack-like and hut-like islands, respectively. In a different method of MBE growth, the co-deposition of 50 nm-thick $Si_{1-x}Mn_x$ films with $0.005 \leq x \leq 0.035$ leads to a 2D spinodal decomposition of the alloy into Mn-rich nanopipes [69].

1.3 δ-doping

Mn δ-doping of Si is one of the methods I investigate in this thesis. This method (also referred to as digital-doping) is based on the confinement of a sheet of Mn impurities to a narrow distribution profile in Si (Fig. 1.2). The width of the distribution can be of the order of the lattice constant and can be created with growth techniques such as MBE.

δ-doping has been widely used for the fabrication of complex heterostructures, where the sharp interfaces and the spatial localization of a high carrier density were shown to greatly improve the performance of electronic and optoelectronic devices [76, 77, 78]. For the growth of DMS, δ-doping was first applied to (Ga,Mn)As and

(Ga,Mn)Sb systems [79, 80]. An enhanced Curie temperature was reported when this technique was employed to grow multilayers of Mn δ-doped GaAs [81, 82]. On the other hand, fewer studies were reported for Mn δ-doped Si, with only one experimental investigation [83]. Qian et al. [84] evaluated the magnetic and electronic properties of a Mn δ-doped layer in Si by performing density functional theory calculations. In their simulation of the δ-doped layer, they placed Mn atoms in Si substitutional sites. Their calculations showed that this 2D structure exhibits properties of a half-metal and an energetically favorable ferromagnetic (FM) ordering with a predicted $T_C >$ 400 K. A similar study that was later performed simulated the δ-doped layer with Mn in interstitial instead of substitutional sites [66]. For all three Mn coverages examined (0.25, 0.5 and 1 ML), it was found that a FM state was (slightly) more stable than an antiferromagnetic (AFM) state. Moreover, the structure with a 0.25 ML Mn layer had a half-metallic behavior whereas a high spin polarization of 85% was obtained when the coverage increased to 0.5 ML. In a recent publication, Otrokov et al. [53] presented a more comprehensive DFT study of the digital Si:Mn structure by considering all possible Mn occupation sites: substitutional, interstitial and a combination of both sites. Their results indicated that the magnetism in this structure strongly depends on the Mn incorporation site. A stable FM state was obtained when Mn substituted Si, whereas a strong AFM interaction was predicted when Mn occupied interstitial sites and a more complex, non-collinear and temperature dependent magnetic ordering was associated with the mixed occupancy configuration. Experimentally, Mn δ-doping was employed to grow multilayers of [Si(20 Å) / Mn(x)]$_{30}$ by MBE [83]. These structures exhibited a room temperature ferromagnetism for $x = 1.0$ and 1.5 Å. However, the origin of ferromagnetism is uncertain since a clear evidence of the absence of precipitates was not provided. Moreover, the multilayers that were grown on Al_2O_3 substrates at room temperature were amorphous and there was no structural analysis to verify the quality of the growth or to confirm the

δ-doping profile.

1.4 Surfactant Mediated Growth

A good control over the growth temperature is necessary to preserve the δ-doping profile and to prevent the clustering of Mn and the formation of undesired secondary phases. An x-ray reflectivity (XRR) study [85] showed that a single Mn δ-doped layer in Si can be annealed up to 300 °C without a significant increase in the Mn distribution profile. Above 300 °C, the width of the profile increases rapidly. In contrast, the homoepitaxial growth of Si typically requires a substrate temperature above 600 °C. As the growth temperature is lowered, the film undergoes a crystalline-to-amorphous transition due to the reduced mobility and the short surface diffusion length of the Si adatoms. This transition occurs at a critical thickness of the deposited Si layer, h_{epi}, which varies exponentially with temperature [86]. One method used to control the growth kinetics is to deposit an atomically thin layer of a low surface energy element. Strain and surface energy will enable some elements to float to the surface during the deposition of a second species. Such elements are referred to as *surfactants* in surface science literature [87, 88, 89]. It is important to note that, although the term surfactant more commonly relates to the *thermodynamic* process of a species that lowers the surface free energy, the term surfactant in epitaxy mostly refers to a surface segregating species that changes the growth *kinetics* of atoms during deposition [88]. The presence of the surfactant also modifies the formation energies of the dopants, as found in GaP [90, 91, 92]. Within this context, Pb is explored in this thesis as a means to control the growth mode of Mn and Si in the samples discussed in Chapters 4 and 5. Pb was chosen as a surfactant in this study because (1) it was shown to increase the surface diffusion length of Si [87] and to improve the homoepitaxy on Si(111) at temperatures as low as 310 °C [93], (2) it is a group IV element that has the same electronic configuration of Si and therefore does not

act as a dopant in Si, (3) its relatively large atomic size inhibits its incorporation in subsurface layers and facilitates its migration to the growth front and (4) it is unable to form a stable alloy with Mn.

1.5 Outline of the Thesis

In Chapter 2, I describe the MBE growth procedures of the Si:Mn samples and the techniques used to analyze them. This includes a discussion of the basic principles and theory of reflection high-energy electron diffraction (RHEED), Rutherford backscattering spectrometry (RBS), XAFS and SQUID magnetometry.

The work of Chapter 3 is an investigation of the growth of ferromagnetic ultrathin MnSi films. This study was influenced by the DFT predictions of ferromagnetic MnSi-B2 structure [32, 55], as discussed previously. Furthermore, our previous finding of a MnSi-B2 structure in a submonolayer of Mn/Si(001) [94] motivated the attempt to grow thicker layers of this structure.

The lack of experimental studies on Mn δ-doped Si and the promising results of Mn δ-doped III-V and DFT predictions inspired the experiments discussed in Chapter 4. In this chapter, I explore the influence of a Pb surfactant on the structure and magnetism of Mn δ-doped Si layers. δ-doping represents one approach to locally induce a high concentration of magnetic moments in Si. Another advantage of δ-doping is that it separates the growth of Mn and Si, therefore permitting the deposition of Mn dopants at a lower temperature than the Si. This is important because, while it is necessary to deposit Mn at a low temperature in order to suppress the formation of metallic clusters and unwanted MnSi phases [95], a much higher substrate temperature is required to maintain the epitaxial growth of Si.

Chapter 5 includes a study of dilute $Si_{1-x}Mn_x$ alloys grown by co-deposition and an investigation of the effect of Pb on their morphology and magnetism. Part of this study is aimed to reproduce the $Si_{1-x}Mn_x$ nanocolumns reported in Ref. [69] and

to measure their magnetic properties. While the cited work did not report magnetic measurements, a similar study on $Ge_{1-x}Mn_x$ [35] found that the nanocolumns have an above room temperature T_C and a large magnetoresistance.

Chapter 2

Experimental Techniques

In this chapter, I describe the procedures used to grow thin films by molecular beam epitaxy (MBE) and the techniques used to analyze their properties. I present a brief discussion of reflection high-energy electron diffraction (RHEED) and Rutherford backscattering spectrometry. I also discuss the theoretical and experimental principles of x-ray absorption fine structure (XAFS), which I employed to probe the local structure of Mn. The chapter concludes with a description of the SQUID magnetometry measurements, with details about the procedures of background subtraction and magnetization data analysis.

2.1 Samples Growth by MBE

The samples discussed in this thesis were grown by VG-V80 MBE system in an ultra-high vacuum (UHV) environment with a base pressure of 5×10^{-11} Torr. Si was evaporated from a pure Si source by an electron-beam gun and the Si flux rate was measured by a quartz crystal microbalance. A thermal effusion cell was used to evaporate Mn, whose flux rate was determined from a Bayard-Alpert ionization gauge placed in the Mn beam and calibrated from RBS and x-ray reflectometry (XRR) measurements. The thin films were deposited on both low-resistivity (10-20 Ω cm) and high-resistivity (600-1200 Ω cm) boron-doped Si(001) substrates with a thickness of 250-500 μm. Prior to each deposition, I prepared the Si substrates by following a two-step process adapted from standard Si industry procedures [96, 97, 98]. The first step consisted of a chemical treatment with semiconductor grade chemicals with the aims

to (i) degrease the Si wafer and remove the surface contaminants that accumulated from packing and storage and (ii) etch the native silicon oxide layer - that also trapped contaminants - and replace it with a cleaner layer through chemical re-oxidation of the Si surface. The reformed chemical oxide is also easier to thermally desorb in UHV. I started the chemical cleaning with an acetone rinse of the Si wafer followed by 15 minutes ultrasonic baths of acetone then methanol. Before removing the wafer from the methanol bath, the beaker was filled with deionized (DI) water and the contents were allowed to overflow in order to remove the hydrocarbon contaminants that float to the surface during the cleaning process. This was found to be important to prevent the contaminants from redepositing on the surface when the wafer is removed from the bath. The wafer was then rinsed again in a DI water beaker then soaked for 10 minutes in a 1:1:5 solution of ammonium hydroxide (NH_4OH), hydrogen peroxide (H_2O_2) and DI water, heated to 75 °C. After a thorough DI rinse, the Si wafer was blown dry with nitrogen and directly transferred to the load-lock of the MBE system. The sample and its Mo holder were then outgassed overnight at 450 °C. Then, I desorbed the chemically formed oxide by heating the substrate in the MBE deposition chamber to 800 °C for 20 minutes and subsequently raised the temperature and held it at about 900 °C for 40 minutes. I monitored the desorption of the silicon oxide layer by *in situ* reflection high energy electron diffraction (RHEED) system (see below) that revealed the characteristic Si(001) (2×1) surface reconstruction pattern (Fig. 2.1) at the end of the oxide removal.

A series of experiments were performed to optimize the substrate preparation method, specifically to obtain a uniform oxide desorption that minimizes the surface roughness. For the adopted method, an Auger electron spectroscopy (AES) system attached to the MBE chamber revealed no contaminants and an oxide-free surface. Atomic force microscopy (AFM) measurements showed an rms surface roughness of $5-7$ Å (Fig. 2.2). The final step of substrate preparation consisted of the deposition

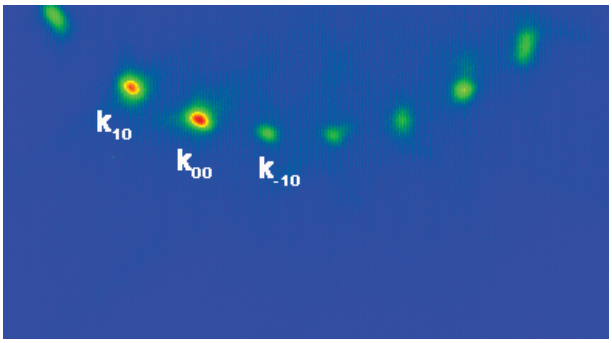

Figure 2.1: RHEED (2×1) surface reconstruction pattern observed after oxide desorption from the Si(001) surface. The specular spot is designated by k_{00}.

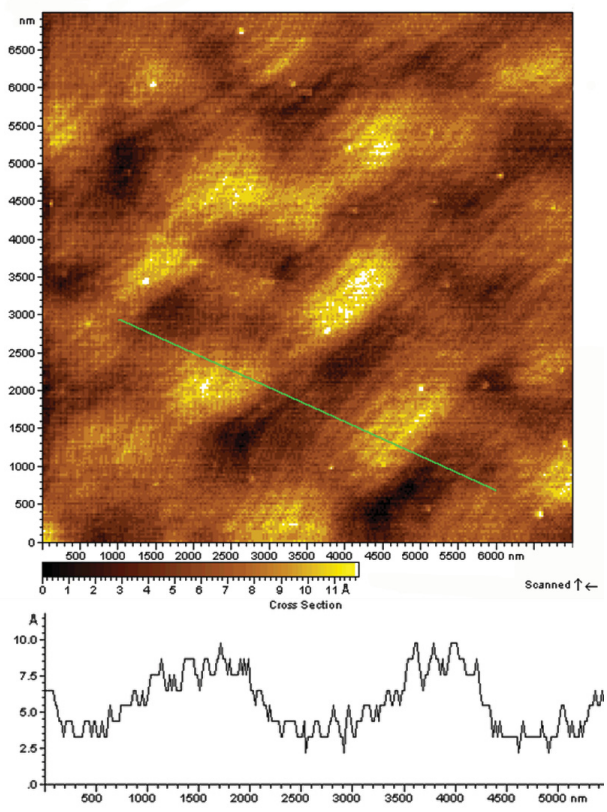

Figure 2.2: AFM image of a typical Si(001) substrate surface after oxide removal and growth of the Si buffer layer. The line scan shows the variation of the surface roughness.

of a Si buffer layer with a thickness of either 20 nm or 100 nm at 600 °C.

For the investigations of the influence of a Pb surfactant, I deposited two ML of Pb from a home-built thermal effusion cell at a substrate temperature $T = 25$ °C. Surface

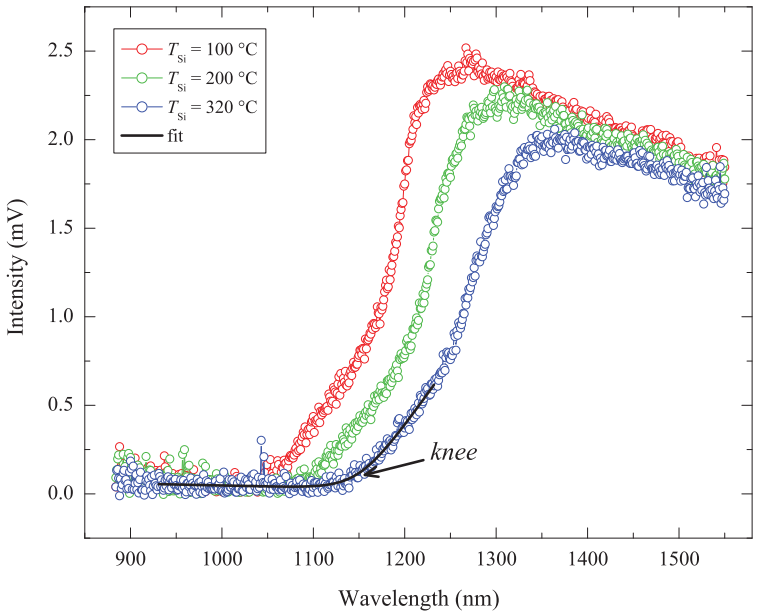

Figure 2.3: Calibration of the DRS. Diffuse reflectance intensity versus wavelength collected at three different temperatures of a Si wafer in UHV. The wafer temperature was measured with a thermocouple in contact with the Si surface. The position of the knee in the absorption spectrum was determined from a fit using an asymptotic function [99] and used as a measure of the temperature.

segregation of Pb was confirmed by *ex-situ* x-ray photoelectron spectroscopy (XPS), secondary ion mass spectrometry (SIMS) depth profile and RBS measurements. For the XPS experiments, a sample was prepared with 2 ML of Pb deposited onto Si(001) and capped by a 12.4 nm Si layer. XPS measurements on this sample showed that (oxidized) Pb is the topmost surface layer. After the sample was soaked in carbonated water, which is known to etch Pb, XPS did not detect a Pb peak.

As I will show in the next chapters, the local structure and magnetism of the Mn doped Si change significantly within a narrow growth-temperature range. Therefore, it was necessary to have an accurate control over the substrate temperature during deposition. The Si substrate was heated in UHV with a C filament embedded in a BN plate. The temperature of the heater was measured with a thermocouple in contact with the backside of the BN plate. However, the difference between the heater and substrate temperature was as much as 200 °C for heater temperatures greater than

1000 °C. To overcome this inconsistency, the temperature of the Si substrate was measured optically with a home built diffuse reflectance spectrometer (DRS) as described in Ref. [99]. DRS determines the substrate temperature from a measurement of the bandgap. For these measurements, the wafers that are polished on one side, and roughened on the backside are used. The diffusively scattered light from the wafers is therefore from light that passed through the polished surface and scattered from the rough backside. Hence, these measurements are in fact transmission experiments. The band edge is shown for 3 temperatures in Fig. 2.3, as denoted by the arrow for $T_{Si} = 320$ °C. The DRS spectrometer was calibrated from the knee of the absorption spectrum as a function of the Si substrate temperature, which was determined by a thermocouple in mechanical contact with the Si wafer in the MBE chamber.

2.2 Reflection High Energy Electron Diffraction

The surface quality during the growth of Si:Mn films was monitored *in-situ* with a Staib Instruments RHEED system attached to the MBE deposition chamber. RHEED is based on the diffraction of electrons from the surface atoms of the substrate and provides real-time information about the evolution of the surface crystal structure, thin film coverage and surface roughness during the epitaxial growth. This information is inferred from the diffraction pattern observed on a fluorescent screen. A beam of electrons with energy in the range of $10 - 60$ keV is provided by an electron gun and is incident on the surface of the sample at a grazing angle, normally $1° - 3°$ (Fig. 2.4(a)). Grazing incidence makes RHEED a surface sensitive technique, with a penetration depth of only few atomic layers. The geometry of the RHEED pattern can be explained by the kinematic scattering theory, which invokes elastic scattering (neglects multiple and inelastic scattering) and the Laue condition of constructive interference to locate the intensity maxima of the pattern [100]. To satisfy the Laue condition, the difference between the diffracted and incident wavevectors $\boldsymbol{k'}$ and $\boldsymbol{k_0}$

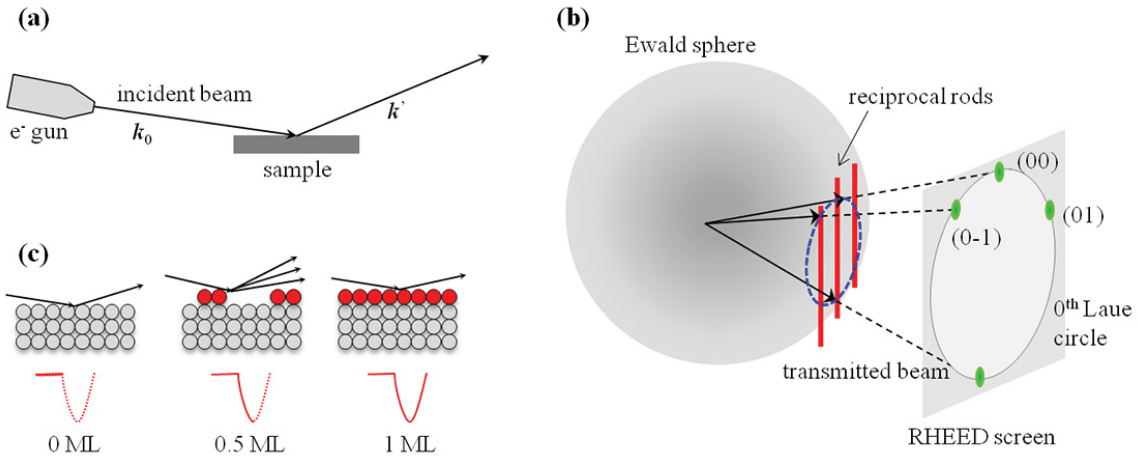

Figure 2.4: (a) RHEED setup showing the incident and reflected wavevectors. (b) The intersections of Ewald sphere and reciprocal lattice rods are projected on the screen to form the RHEED diffraction pattern. (c) Schematic illustration showing the relationship between thin film coverage and specular spot intensity oscillations based on the interference model.

must be equal to a reciprocal lattice vector $\boldsymbol{G}$:

$$\boldsymbol{k'} - \boldsymbol{k_0} = \boldsymbol{G}. \tag{2.1}$$

For elastic scattering, the relationship between the two wavevectors becomes:

$$|\boldsymbol{k'}| = |\boldsymbol{k_0}|. \tag{2.2}$$

The direction of diffracted intensity maxima is determined from the construction of Ewald sphere, which is a geometrical representation that combines the conditions of conservation of crystal momentum (2.1) with conservation of energy (2.2). In this construction, the Ewald sphere has a radius $|\boldsymbol{k_0}|$ and it is formed by placing the tip of the incident wavevector $\boldsymbol{k_0}$ on a reciprocal lattice rod. Given that the electrons experience the potential from the surface atoms, in the case of a perfect surface the sample behaves as a two-dimensional potential. In reciprocal space, this 2D arrangement of atoms translates to a two-dimensional array of infinitely thin rods that

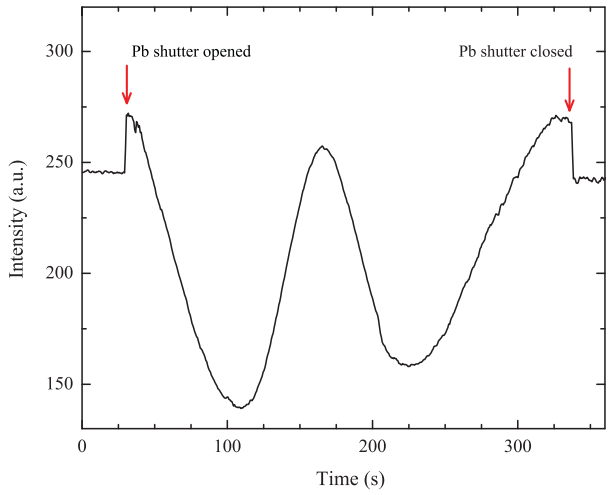

Figure 2.5: RHEED specular spot intensity oscillations during the growth of 2 ML Pb on Si(001).

are perpendicular to the surface (Fig. 2.4 (b)). The diffraction condition is satisfied when a rod intersects the Ewald sphere, as illustrated in Fig. 2.4(b). For atomically flat single crystalline surfaces, the rods are very thin so that their intersection with the sphere occurs at *points* on the surface of the sphere, which project as sharp spots on the screen. These diffraction spots lie on concentric circles, known as Laue circles, centered at the point on the screen which is the projection of the parallel component of $\boldsymbol{k_0}$ [100]. For most angles accessible to the system, only the zeroth order Laue circle is visible, as demonstrated in Fig. 2.1, where the diffraction spots are designated by the Miller indices (hk), where k specifies the zone and k_{00} corresponds to the specular spot. Streaks also appear in the diffraction pattern and are due to a broadening of the rods, which results from surface disorder, such as surface steps [101]. Other RHEED patterns observed in the growth of the Si:Mn material system include concentric rings instead of spots (or streaks) indicative of the growth of a polycrystalline structure.

RHEED also provides a powerful tool to determine the growth rate and coverage of thin films. This can be done by monitoring the intensity of the specular spot, which can oscillate as a function of time as more layers are grown on the surface. The period of one oscillation corresponds to the time required to deposit a single atomic

layer. One simple model explains this behavior by an interference effect during the layer-by-layer growth mode. In this model, the intensity oscillations are associated with changes in the surface coverage during growth. The reflection of the electrons from the islands and from the flat layer underneath changes the path length of the diffracted beam and leads to a reduced intensity of the specular spot, which reaches complete destructive interference when the path length difference is equal to half an odd integer multiple of the wavelength (anti-Bragg condition). As the growth proceeds, the islands coalesce and the number of edges on the surface decreases, therefore reducing the interference of the reflected beam and increasing the intensity of the specular spot again (Fig. 2.4 (c)).

Here, I used RHEED intensity oscillations to determine the Pb coverage on Si(001), as shown in Fig. 2.5 for the deposition of 2 ML Pb. Note that, during the growth of the first Pb ML, the Si (2×1) surface reconstruction gradually disappeared. At the end of the second layer, a Pb (2×1) reconstruction appeared, in agreement with previous reports [102, 103].

2.3 Rutherford Backscattering Spectrometry

Rutherford backscattering spectrometry was used to determine the amount of Mn in the samples and the fraction of Mn atoms that occupy substitutional sites. In RBS, a beam of energetic ions is incident on the sample and the number and energy of the backscattered ions are analyzed in order to determine the composition and depth distribution of the elements in the sample. As the incident ions penetrate the surface, they overcome the electron-cloud shield, undergo an elastic collision with the nuclei of the target atoms and backscatter out of the surface. For the RBS experiments conducted in this work, a beam of 2 MeV He ions provided by a 1.7 MV Tandetron accelerator was used and the backscattered particles were detected with a solid state surface barrier detector located at a scattering angle of 170°. The penetration depth

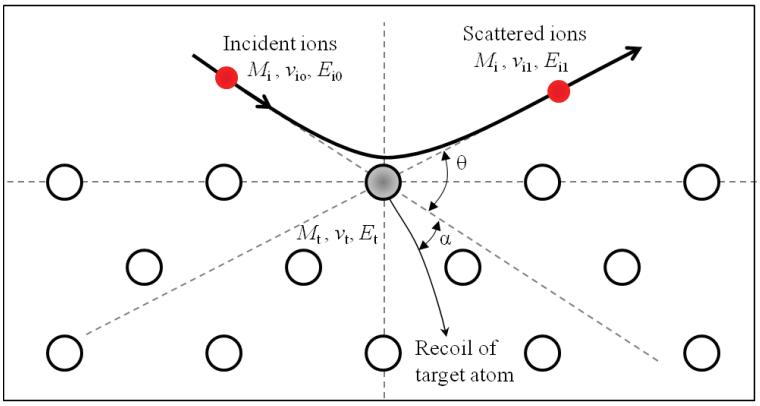

Figure 2.6: Scattering geometry used to determine the kinematic factor of RBS.

for a 2 MeV He beam is close to 2 μm.

The scattering process in RBS is illustrated in Fig. 2.6. The scattering is governed by a Coulomb repulsion between the impinging ion and the nucleus of the target atom and the energy transfer in this process is calculated by applying the principles of conservation of energy and momentum [104, 105]. For an incident beam of particles with known mass M_i and energy E_{i0}, the energy E_{i1} after the collision is related to E_{i0} by the *kinematic factor* K:

$$E_{i1} = K E_{i0}, \tag{2.3}$$

where

$$K = \left(\frac{M_i \cos\theta + \left(M_t^2 - M_i^2 \sin^2\theta\right)^{1/2}}{M_i + M_t} \right)^2 \tag{2.4}$$

is found for M_i less than the target atom mass, M_t, from the conservation of kinetic energy and the conservation of momentum.

The detector measures E_{i1} at fixed angle. For elements on the surface, peaks are observed in the spectra at energies corresponding to M_t as given by (2.4). The concentration of a given element can then be found from the height of the corresponding peak. Fig. 2.7 shows a RBS spectrum collected for one of the Si:Mn samples.

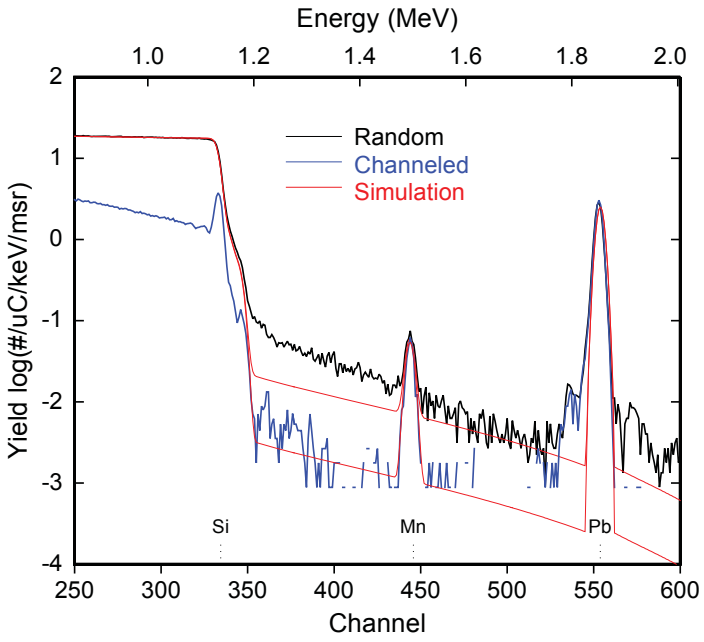

Figure 2.7: RBS spectra of one of the samples collected in random and channeled orientations. The step in the Si peak around 1.15 MeV (random) is due to scattering from Si at the surface (higher energy) and from Si in the substrate (lower energy). The Mn substitutional fraction x_{sub} is calculated from the difference between the areas of Mn peaks in both orientations.

While the ions penetrate the surface, the energy transferred depends not only on the scattering of the ions from the nuclei of the target atoms, but also on the inelastic scattering from electrons in the sample. The incident ions continuously lose energy due to collisions with electrons at a rate that is linear with the distance traveled (x_t). This is normally expressed by the stopping power of the material $S(E)$:

$$S(E) = \frac{-dE}{dx_t} \tag{2.5}$$

Consequently, ions scattered from atoms near the surface have higher energies than those scattered from atoms deeper in the sample. The stopping power depends on the type of incident ions, their energy, the elements present in the sample and the density of the sample [105]. For different materials and incident ions, $S(E)$ can be

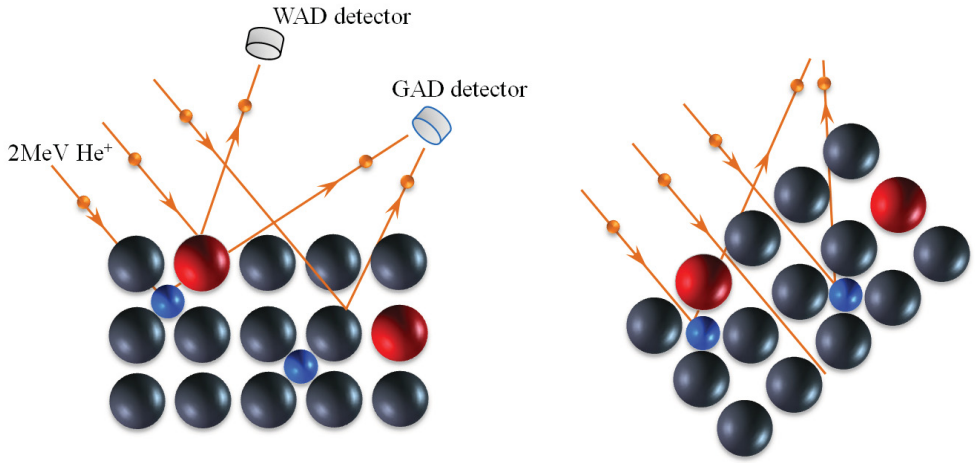

Figure 2.8: Schematic illustration of the RBS setup with the sample aligned in random (left) and channeling (right) orientations relative to the incident He ions beam. Substitutional (interstitial) atoms are shown in red (blue). For the samples discussed in Chapter 4, two detectors were used: a wide angle detector (WAD) and a glancing angle detector (GAD), positioned relative to the backscattering angle.

found from tabulated data (see for example Ref. [106]). Typical $S(E)$ range for 2 MeV He is $100 - 800$ eV/nm. Energy loss due to electron scattering is manifested in the RBS spectrum by a broadening or a gradual shift of the backscattered peaks towards lower energy. Therefore, by measuring the shift and width of the peaks one can find the depth and thickness of a particular layer of the sample.

Besides the composition and depth profiling, information about the crystal structure can be obtained from RBS when the experiments are conducted in channeling orientation. In channeling RBS, the incident beam is aligned with a high symmetry axis of the single crystalline sample so that the impinging ions travel into the channels of the crystal (Fig. 2.8). This configuration decreases the probability of backscattering from atoms in crystalline lattice sites and increases the backscattered yield from elements that are not in registry with the lattice, namely interstitial atoms. In Chapter 4, channeling was used in conjunction with measurements where the sample was oriented in a random (non-channeling) orientation in order to find the fraction of substitutional Mn, x_{sub}, in the Si:Mn samples (Fig. 2.7). This fraction was estimated

from the difference in the integrated Mn signal of both orientations:

$$x_{sub} = 1 - \frac{\mathrm{Mn}_{\mathrm{channel}}}{\mathrm{Mn}_{\mathrm{random}}} \tag{2.6}$$

2.4 X-ray Absorption Fine Structure

The behavior of the transition metal ions in semiconductors is highly sensitive to the local structure around the ions. Even when dilute concentrations of magnetic dopants lead to the formation of nanocrystalline composites, conventional techniques such as x-ray diffraction are not capable of detecting their crystal structure. Alternatively, x-ray absorption fine structure spectroscopy (XAFS), which employs high intensity x-rays from a synchrotron radiation source, has emerged as a valuable technique to probe the atomic structure of lightly doped systems such as the Mn-doped Si of this study. I used XAFS in this work in order to investigate how the local environment of Mn affects the magnetic properties of the samples. This section includes a brief review of the theory of XAFS, along with a discussion of the experimental setup and procedures of data analysis pertinent to the samples discussed in Chapters 3 and 4.

2.4.1 Theory of XAFS

XAFS is an element specific technique based on the measurement of the x-ray absorption coefficient as a function of incident x-rays energy, $\mu(E)$ [107, 108, 109]. The energy is typically scanned from 200 eV below to 1000 eV above a particular x-ray absorption edge of a specimen. At the onset of x-ray absorption, a core electron is emitted as a photoelectron, while an electron at a higher energy level drops to fill the core hole created from the emission, and releases a fluorescence x-ray or an Auger electron either of which can be used to measure the absorption. The emitted photoelectron can be described as a spherical wave that propagates from the absorber atom,

backscatters from neighboring atoms and then interferes with an outgoing photoelectron wave as it returns to the absorber. A schematic illustration of the XAFS process is shown in Fig. 2.9(a). The interference of the scattered and outgoing waves at the absorber atom affects the probability of x-ray absorption and causes oscillations in $\mu(E)$ (Fig. 2.9(b)). For a given incident x-ray energy, a constructive interference occurs and a maximum appears in the oscillations of $\mu(E)$ if the two waves are in phase. When the incident energy increases, the wavelength of the photoelectron shortens, and since the average distance between the absorber and scattering atom does not change, the two waves gradually become out of phase and a minimum is observed in $\mu(E)$. Therefore the oscillations, or *fine structure*, of $\mu(E)$ contain information about the local environment of the absorber, which include the identity, the number, the bond length and the level of bonding disorder of the neighboring atoms [108, 109].

The XAFS spectrum can be divided into two regions that contain different information about the system: In the near-edge region, x-ray absorption near-edge spectroscopy (XANES) is performed to decode the valence and oxidation states of the system, whereas above the edge, extended x-ray absorption fine structure spectroscopy (EXAFS) contains information about the local bonding of a selected element. It is the EXAFS part of the spectrum that is of interest here. In XAFS nomenclature, atoms at the same radial distance from the absorber are said to belong to a *shell* and their number is the *coordination number*. When the photoelectron scatters from one neighboring atom and returns to the absorber, the distance travelled (absorber-scattering atom-absorber) is a *single scattering path*, while a *multiple scattering path* refers to the total distance after scattering from two or more atoms, such as in the triangular path shown by the dashed arrows in Fig. 2.9(a). Multiple scattering depends on the bond angles and generally has a low probability to occur within the first shell [109]. For the analysis conducted in this work, multiple scattering did not have any significant contribution to the spectra and was thus omitted.

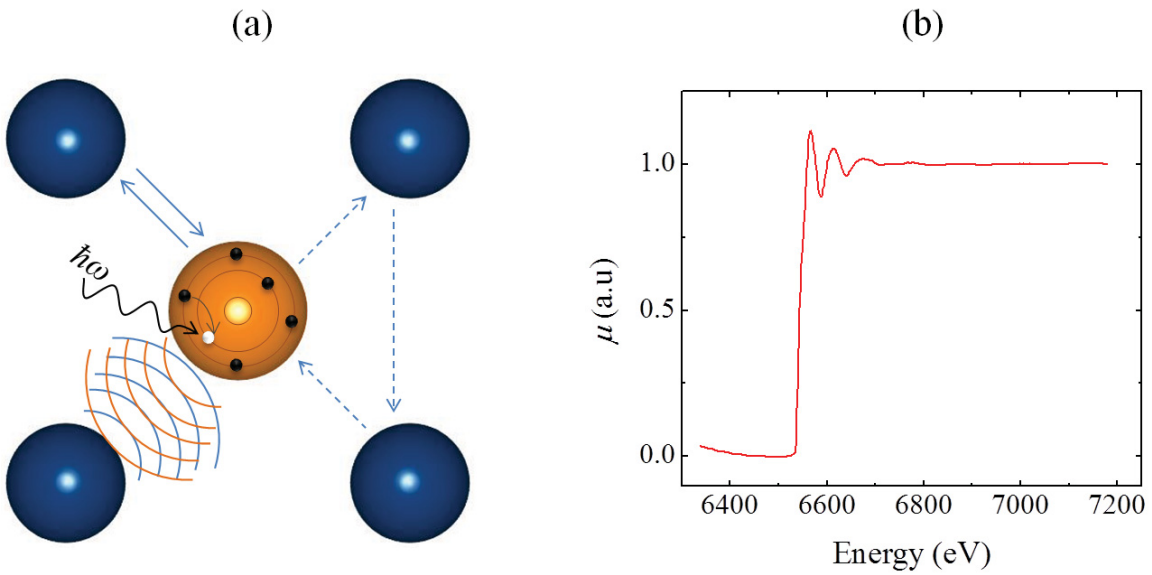

Figure 2.9: (a) Illustration of the XAFS process: a photoelectron wave (orange) emitted from the absorber atom after absorption of an incident x-ray of energy $\hbar\omega$ leaves a core hole (white circle), which is then filled by a higher energy level electron. The photoelectron backscatters from neighbouring atoms through a single scattering (solid blue arrows) or a multiple scattering (dashed blue arrows) process. (b) X-ray absorption coefficient as a function of incident energy, $\mu(E)$, below and above the Mn K-edge. Constructive and destructive interferences between the emitted and backscattered photoelectron waves lead to oscillations in $\mu(E)$ above the absorption edge.

The EXAFS signal $\chi(E)$ results from the interaction of the photoelectron with neighboring atoms and its contribution to the absorption process can be included as a correction factor [108, 110] in the expression of $\mu(E)$:

$$\mu(E) = \mu_0(E)\ [1 + \chi(E)], \tag{2.7}$$

where $\mu_0(E)$ is the x-ray absorption coefficient of an isolated absorber atom. Consequently, $\chi(E)$ normalized to a single x-ray absorption is written as:

$$\chi(E) = \frac{\mu(E) - \mu_0(E)}{\mu_0(E)}, \tag{2.8}$$

and is often converted to $\chi(k)$, where the wavenumber k of the photoelectron is expressed in terms of the difference between the incident x-ray energy E and the energy of the core electron E_0:

$$E - E_0 = \frac{\hbar^2 k^2}{2m_e}, \tag{2.9}$$

$$k = \sqrt{\frac{2m_e(E - E_0)}{\hbar^2}}. \tag{2.10}$$

Several theories were proposed to derive an expression for $\chi(k)$ [111, 112, 113, 114]. The simplest derivation was given by Stern [112] who considered a plane-wave approximation to develop what is now known as the standard EXAFS equation. The theory provides a good description of most experimental data when $k > 3$ $\mathrm{\AA}^{-1}$ or when the energy is $\gtrsim 80$ eV above the edge [110]. At lower k values, spherical wave theory [113, 114] is needed for a more accurate description. The $\chi(k)$ equation sums the contribution of each scattering path i and is given by [115, 116]:

$$\chi(k) = \sum_i \frac{N_i \; S_0^2 \; F_i(k)}{kR_i^2} \; \sin[2kR_i + \varphi_i(k)] \; e^{-2\sigma_i^2 k^2} \; e^{\frac{-2R_i}{\lambda(k)}}, \tag{2.11}$$

where N_i is the coordination number of the atoms of type i located at a distance R_i from the absorber atom. Each of these atoms has an effective scattering amplitude $F_i(k)$ that depends on their atomic number. A formalism to calculate $F_i(k)$ was given by Rehr and Albers [117] and implemented in the computer code FEFF [118]. The constant S_0^2 is the amplitude reduction factor: it accounts for the relaxation of the remaining electrons of the absorber in the presence of a core hole. S_0^2 is strongly correlated to N and its value varies between 0.7 and 1.0 (element dependent) and is usually determined from a standard sample. For example, $S_0^2 = 0.7$ was found for Mn using a reference MnSi sample [119]. The sine term describes the oscillatory part of the EXAFS signal. Its argument comprises the phase acquired by the photoelectron wave over a single scattering path ($2kR$), and the phase shift $\varphi(k)$ that results from the interaction of the photoelectron with the nuclei of the absorber and the neighboring atom. In the first exponential term of Eq. (2.11) σ_i^2 is the mean-square displacement parameter that accounts for the fluctuations in the bond length R_i due to thermal and structural disorder. The finite lifetime of the scattering process is represented by the mean free path parameter $\lambda(k)$ of the photoelectron. It is this parameter that makes EXAFS a *local probe* technique since it limits the contribution to the EXAFS signal to atoms within $\sim$ 10 Å from the absorber atom [109]. Similar to $F_i(k)$, the FEFF code is used to determine $\lambda(k)$ and the phase $\varphi(k)$, whereas N, R and σ^2 are normally determined by fitting the experimental data.

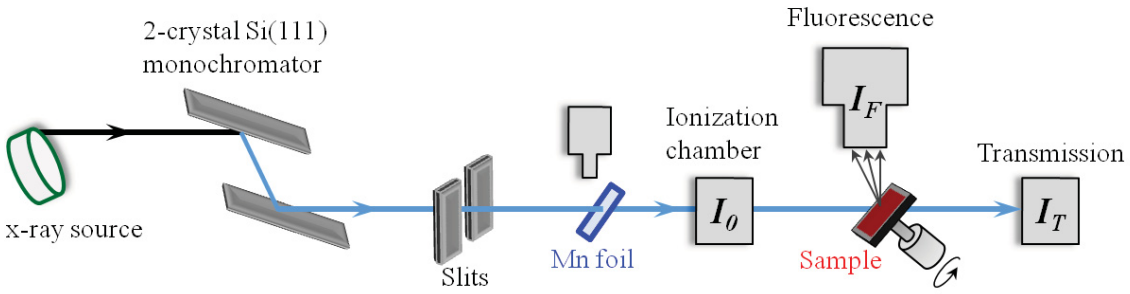

Figure 2.10: Basic experimental setup of XAFS. Both fluorescence and transmission modes are shown.

2.4.2 XAFS Experiments and Data Analysis

I performed the XAFS experiments on Mn doped Si samples at Sector 20 of the Advanced Photon Source (APS- Argonne National Laboratory) using the facilities of PNC/XSD ID beamline [120]. All measurements discussed in this work were collected at the Mn K-edge in fluorescence mode (Fig. 2.10), which is more convenient than the conventional transmission mode when the concentration of the element of interest is low (< 10 wt. %). In fluorescence mode, the absorption coefficient $\mu(E)$ is determined by measuring the fluorescent yield I_F from the sample at a given incident x-ray intensity I_0, where

$$\mu(E) \propto \frac{I_F}{I_0}. \tag{2.12}$$

A He-filled ionization chamber and a multi-element solid state detector were used to measure I_0 and I_F, respectively. A Si(111) double-crystal monochromator was used to set the energy of the x-ray from the white beam of the synchrotron source and scan it around the Mn K-edge energy (6539 eV). The monochromator was detuned by 20% at 6750 eV (normally ~ 200 eV above the absorption edge) in order to filter out the higher harmonic energies in the x-ray beam [109]. To correct for drifts in the monochromator crystals that normally occur over the duration of a measurement, the energy of the monochromator was calibrated by simultaneously measuring a Mn foil that served as an energy reference sample. The beam was focussed on the sample

to a typical size of 5 μm $\times$ 5 μm using Kirkpatrick-Baez mirrors. I mounted the samples on a spinner turning at a rate of 30 - 40 Hz to minimize the contributions from Bragg peaks to the EXAFS signal, and I performed polarization dependent measurements by changing the sample orientation relative to the electric field vector, **E**, of the linearly polarized x-rays. For the out-of-plane (oop) polarization, **E** was within $2^\circ - 7^\circ$ off the [001] substrate normal direction, depending on the experiment, whereas the in-plane (ip) polarization measurements were averaged over all in-plane orientations perpendicular to [001]. Given the high symmetry of the [001] direction in Si, no orientation-dependence was expected in the ip XAFS signal.

Typically, I collected 20 or more scans for each sample in a given orientation. When glitches (such as Bragg peaks) in an individual spectrum were identified, they were removed using the *deglitching* feature of the WinXAS software [121]. In another computer program, ATHENA [122], the multiple scans were weighted according to noise level and averaged to a give the spectrum of $\mu(E)$ used to extract the EXAFS function $\chi(k)$. The data processing steps are summarized in Fig. 2.11, which involved the subtraction of the pre- and post-edge backgrounds, the evaluation of the edge energy E_0 and the normalization of the $\mu(E)$ spectrum. To subtract the pre-edge background, which normally contains instrumental background and absorption from other edges, I used a linear function to fit a short range of datapoints in the pre-edge region. A smooth spline function (quadratic or cubic) was used for the post-edge removal. The subtracted post-edge represents absorption of the "isolated atom", $\mu_0(E)$ in Eq. (2.7). Since the edge energy E_0 lies within an energy region of $\mu(E)$, its value is not precisely defined. The centroid of the derivative $\frac{d\mu(E)}{dE}$ was selected for all data sets as a best estimate of E_0. I then calculated k from E_0, as given in Eq. (2.10). Finally, $\mu(E)$ was normalized prior to calculating $\chi(k)$, which transforms $\mu(E)$ to the absorption per one Mn atom and eliminates the contribution from factors that vary between samples, such as the detector response and the Mn concentration

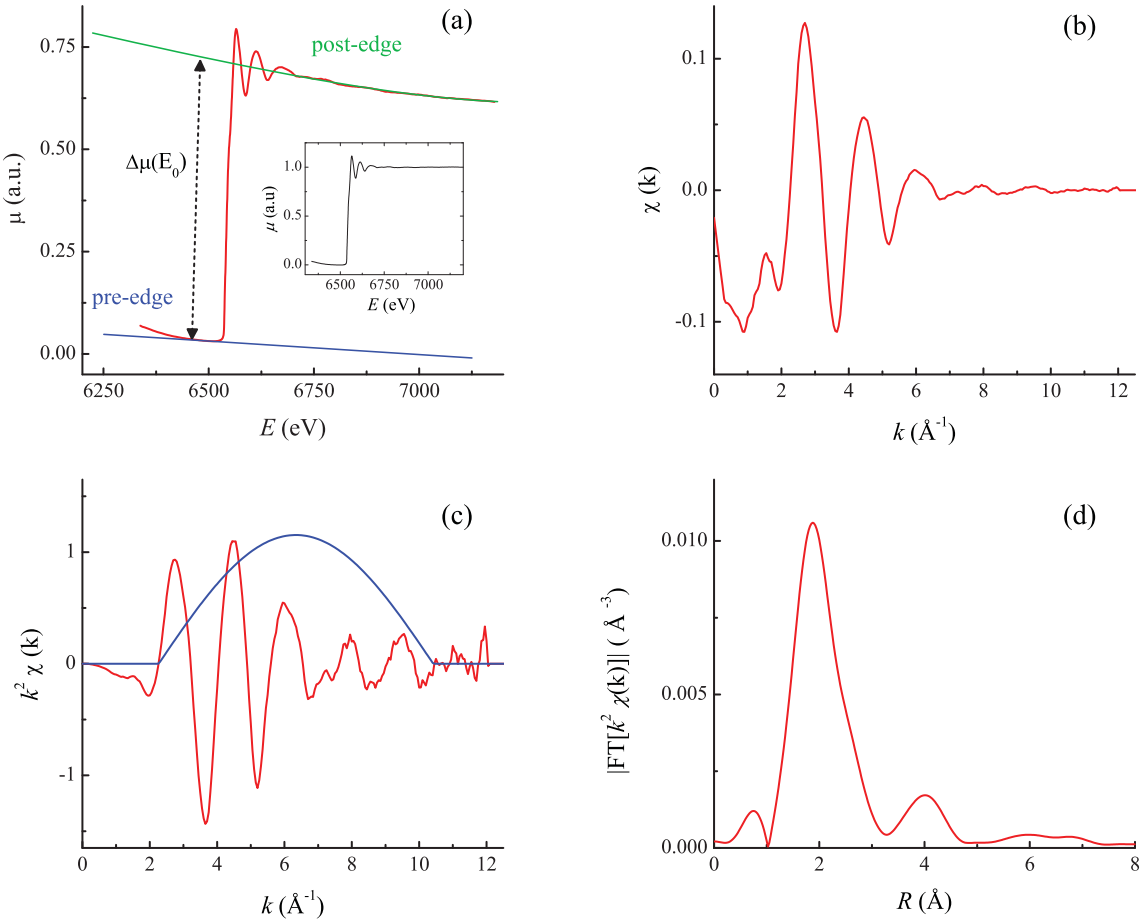

Figure 2.11: The different steps of XAFS data analysis shown here for the Mn K-edge. (a) Background subtraction from the averaged $\mu(E)$ using fits to the pre-edge and post-edge regions. The height of the edge-step $\Delta\mu(E_0)$ is calculated and used to normalize $\mu(E)$ (inset). (b) XAFS function $\chi(k)$ obtained from Eqs. 2.8 and 2.10. (c) A k^2 weighting factor multiplies $\chi(k)$ to amplify the oscillations at higher k values, and a window function (blue curve) is applied before the Fourier transform (FT). (d) Magnitude of the FT of $k^2\chi(k)$. The position of the peaks appear at distances smaller than the actual bond lengths due to the phase shift of the XAFS interference function.

[108]. I normalized $\mu(E)$ by dividing the data by the height of the edge-step, $\Delta\mu(E_0)$, calculated from the difference between the pre- and post-edge functions extrapolated to the absorption edge energy E_0 (Fig. 2.11(a)). This process induces an uncertainty as large as 10% on $\Delta\mu(E_0)$ [109]. Given that $\Delta\mu(E_0)$ determines the amplitude of the EXAFS oscillations and, therefore, correlates to S_0^2 and N of Eq. (2.11), the coordination number is determined with at most 10% accuracy.

Once $\chi(k)$ is obtained, it is possible to fit $\chi(k)$ either in k-space or in real space. Here, it was more advantageous to Fourier transform (FT) $\chi(k)$ in order to extract the structural parameters N_i, R_i and σ_i^2 from a fit to the data in R-space. Prior to the FT, it is customary to weight $\chi(k)$ by a k^n factor (where $n = 1$, 2 or 3) to amplify the oscillations of $\chi(k)$ at higher k. In addition to a k^2 weighting factor, I used a Gaussian window function to multiply all EXAFS functions analyzed here. A window parameter, set to 10%, controlled the width of the Gaussian function. The window function is useful to avoid ripples that normally occur when the FT is taken over a finite data range $\Delta(k)$. Although in a typical measurement the EXAFS data was collected from $k = 0$ to 15 Å^{-1}, the transformation covered a narrower range that depended on the quality of the data: k_{min} of $\Delta(k)$ was set to the first node above 2.0 Å^{-1} (above the edge), whereas k_{max} extended to the zero-crossing just before the point where the noise level became significantly high, usually around 10 Å^{-1}. Similarly, I fit the Fourier transformed data within a limited R-range, between 1.1 Å and at most 3.0 Å.

I determined the local coordination of Mn from a least-squares fit between a theoretical model and the experimental spectrum. To build the theoretical model, I input an "initial guess" structure, namely MnSi with a B20 crystal structure, into the software ATOMS [122] to generate the x, y, z coordinates of the atoms surrounding the Mn absorber in a cluster of radius $R = 6$ Å. The list of atoms positions was then transferred to FEFF8.2 which computed the theoretical EXAFS spectrum of

MnSi-B20 and generated a list of scattering paths with the corresponding effective amplitude $F_i(k)$, phase shift $\varphi_i(k)$ and mean free path $\lambda(k)$. The model and the calculated scattering paths were imported to WinXAS to fit the data with N_i, R_i and σ_i^2 as fitting parameters. The criteria for a best fit were a minimum in the goodness of fit parameter, χ^2, and the percent residual, $R(\%)$, defined in WinXAS as:

$$\chi^2 = \frac{1}{\sigma_{exp}^2} \sum_{i=1}^{N_d} [y_{exp}(i) - y_{th}(i)]^2, \tag{2.13}$$

$$R(\%) = 100 \times \frac{\sum_{i=1}^{N_d} |y_{exp}(i) - y_{th}(i)|}{\sum_{i=1}^{N_d} |y_{exp}(i)|}, \tag{2.14}$$

where σ_{exp} is the estimated experimental error, N_d is the number of data points and y_{exp} and y_{th} are the experimental and theoretical data points, respectively.

Note that the amount of information that can be extracted from the EXAFS data is constrained by the range Δk and the fit region ΔR according to the Nyquist theorem where the number of independent points N_{Ip} is [123]:

$$N_{Ip} = (\frac{2}{\pi} \Delta k \Delta R) + 2. \tag{2.15}$$

A "meaningful" fit in EXAFS analysis requires the number of variables for a given fit to be less than 2/3 the number N_{Ip}. Therefore, the fit region only included the first two scattering paths (6 variables), which corresponded to single scattering from the first and second nearest neighbors of Mn. Moreover, an energy shift parameter ΔE_0 was added to each scattering path in order to account for the threshold energy (E_0) misalignment of the experimental data relative to the theoretical calculation. I constrained ΔE_0 to be the same for both scattering paths, and also treated it as a constant parameter among the samples since E_0 was equally defined and had

virtually the same value for all measurements. Like S_0^2, the value of ΔE_0 was found from the fit of the MnSi reference sample and transferred as a fixed parameter to all data sets. For most results, a strong correlation existed between the second shell coordination number, N_2, and the mean square relative displacement σ_2^2 of the second shell. It was not possible to break the correlation with a simultaneous fit to a k^1- and k^2-weighted model, even though each parameter has a different k dependence. To extract a meaningful description of the second shell, I calculated the area under the profile function for the second shell which represents a combined contribution from N_2 and σ_2^2.

I determined the uncertainties from the "2 χ^2_{min}" method [108, 124, 125] as follows: For a given parameter, I found the increase in its value required to double χ^2_{min}. The increment for which the χ^2_{min} doubled its value was considered as the uncertainty of the specified parameter. I applied this method to all except the highly correlated parameters, N_2 and σ_2^2.

2.5 Measurement of Magnetic Properties

2.5.1 The SQUID Magnetometer

I characterized the magnetic properties of the Si:Mn samples by measuring the dependence of their magnetic moment, m, on the applied field, H, and the remanent moment as a function of temperature, $m_r(T)$. The magnetic measurements were performed with a Quantum Design magnetic property measurement system (MPMS XL-5) equipped with a 5 T magnet and a superconducting quantum interference device (SQUID) magnetometer with longitudinal pickup coil, all housed inside a liquid He dewar. The magnet consists of a superconducting solenoid connected to an external bipolar power supply providing a current that produces a uniform magnetic field along the axis of the pickup coil, with values between -5 T and 5 T. The pickup coil is

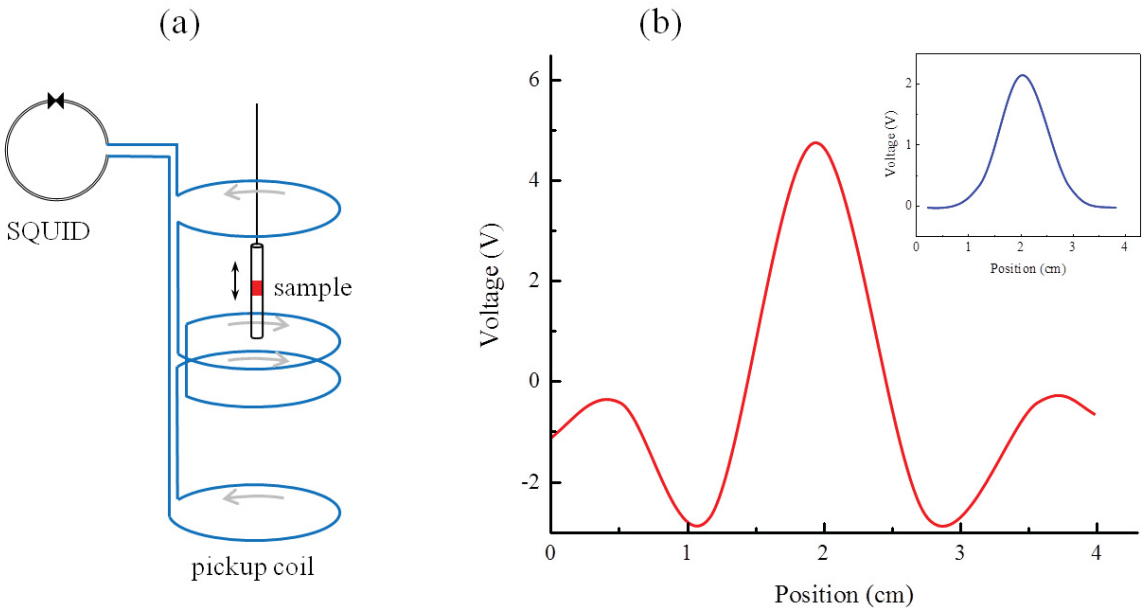

Figure 2.12: (a) The SQUID and second-order gradiometer pickup coil of the MPMS system form a closed superconducting loop. The sample is mounted inside a plastic straw attached to a transfer rod and moves through the central coils. (b) The output signal of the SQUID as the sample position changes with respect to the second-order gradiometer. The inset shows the output voltage expected from a first-order (2 turns) pickup coil.

placed at the center of the magnet and consists of a superconducting wire formed into a second-order gradiometer and connected to the SQUID by superconducting wires. The second-order gradiometer minimizes the noise caused by the environment and by fluctuations in the magnetic field: In the configuration shown in Fig. 2.12(a), the central turns of the gradiometer are wound opposite to the upper and lower turns so that when fluctuations in the magnetic field occur, the change in the flux detected by the central turns is cancelled by the change in the flux in the upper and lower turns [126]. During a measurement, the sample is driven through the central turns of the pickup coil at a constant rate. The electromotive force induced in the pickup coil is detected by the SQUID, which is formed with a ring of a superconducting material linked by a thin insulating layer forming a Josephson junction. The Josephson effect makes the SQUID a very sensitive device, capable of detecting magnetic fields as small as

10^{-15} T. In the MPMS system, the SQUID sensor is placed inside a superconducting shield to isolate it from the magnetic field of the superconducting magnet and from fluctuations in the ambient magnetic field. The data collected during a measurement is the SQUID output voltage as a function of the sample position with respect to the pickup coil. The detected signal is fit to the voltage of a point source magnetic dipole moving in a second-order gradiometer [126], as shown in Fig. 2.12(b).

For all measurements performed in this thesis, the reciprocating sample option (RSO) was used. In RSO, the sample holder is attached to a transport rod connected to a servo motor which oscillates the sample inside the pickup coil. This method results in a magnetic moment sensitivity of 5×10^{-12} A m^2. Moreover, in order to improve the signal-to-noise ratio, five consecutive measurements were collected and averaged for each data point.

2.5.2 Background Subtraction

The low Mn content in the samples made their magnetic signal prone to measurement artifacts and to be dominated by the diamagnetic moment of the Si substrate. The procedures to remove these contributions and analysis of the SQUID data are presented in what follows.

The samples were carefully handled with clean, non-magnetic tools and mounted inside a standard MPMS sample holder that consisted of a clear plastic straw. To maximize the magnetic signal, 4 to 6 pieces of each sample with a typical size of 4 mm $\times$ 5 mm were wedged into the straw. For $m_r(T)$ measurements, I applied a field $\mu_0 H = 5$ T at $T = 2$ K to saturate the magnetization of the samples before setting the field to zero. To ensure that the field was zero, I used the magnet reset option of the MPMS, which discharges any remaining magnetic flux trapped in the coils by heating the magnet above its superconducting transition temperature. The remanent moment was then measured on warming the sample up to the highest attainable temperature

of 400 K. Some sample holders were found to induce a weak signal in the SQUID due to nonuniformities or small indentations in the straw. The maximum value measured for the remanent moment in that case did not exceed 1 $\times 10^{-8}$ emu. Other contributions that dominated the $m - H$ signal of the samples were the diamagnetic and paramagnetic responses of the Si substrate and its boron dopants. To subtract the two contributions, I prepared and measured a control sample that consisted of a 100 nm Si layer grown on low-resistivity Si(001) substrate. The wafer cleaning and the growth conditions were the same as those of the Si:Mn samples. The average of the two branches of the $m-H$ curve of the control sample (Fig. 2.13) was then fit with:

$$m(H)_{Si(001)} = \chi_D H + m_{sat}\ B_j(x) \tag{2.16}$$

where the Si diamagnetic susceptibility $\chi_D = 1.22 \times 10^{-6}$ kA m^2/T kg was determined from a linear fit to the $m - H$ data above a field $\mu_0 H = 3$ T (blue line in inset of Fig. 2.13), m_{sat} is the saturation moment and $B_j(x)$ is the Brillouin function that describes the dependence of a paramagnetic moment on the applied field and on the total angular momentum quantum number j:

$$B_j(x) = \frac{2j+1}{2j}\coth(\frac{2j+1}{2j}x) - \frac{1}{2j}\coth(\frac{1}{2j}x) \tag{2.17}$$

$$x = \frac{g\mu_B j H}{k_B T} \tag{2.18}$$

with g, the Landé factor, k_B, the Boltzmann constant and T is the temperature of the measurement. The fit shown in Fig. 2.13 yielded a $m_{sat} = (3.9 \pm 0.1) \times 10^{-5}$ A m^2/kg that corresponds to a boron concentration of 6.3 $\times 10^{15}$ atoms/cm^3. This falls well

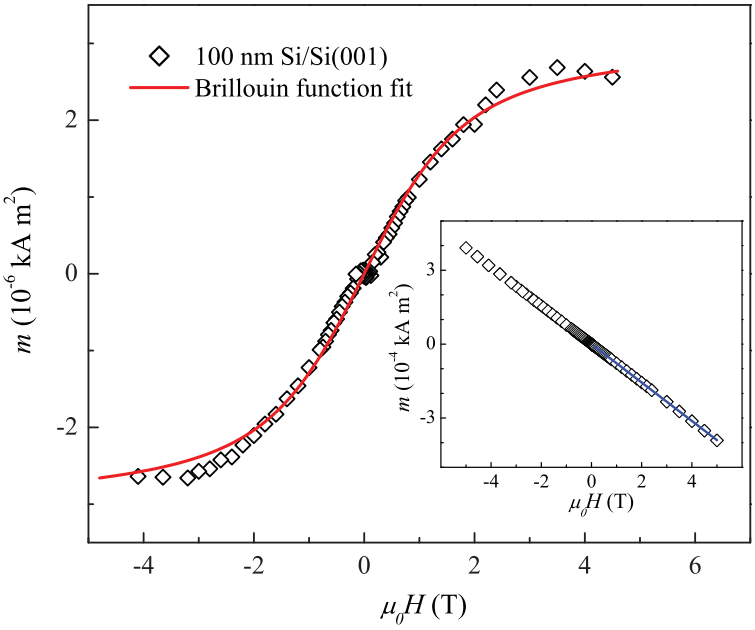

Figure 2.13: Hysteresis curve of a control sample after subtraction of the Si diamagnetic contribution from the measured data (inset). The average of the increasing and decreasing branches was fit with a Brillouin function to extract the paramagnetic contribution of the boron dopants in the substrate. The diamagnetic susceptibility χ_D is determined from the slope of a linear fit (blue line in inset) to the measured data above $\mu_0 H = 3$ T.

within the boron concentration range of $1.0 \times 10^{15} - 1.0 \times 10^{16}$ atoms/cm^3 extracted from the substrate resistivity. On the other hand, I could not detect a paramagnetic signal from a high-resistivity Si(001) substrate where the boron concentration was in the order of $10^{13} - 10^{14}$ atoms/cm^3, and therefore only the Si diamagnetic response was subtracted from the $m - H$ data of the samples grown on this type of substrates.

A good number of $m - H$ measurements showed sudden *jumps* in the moment mainly at fields above 2 T (Fig. 2.14(a)). This behavior resulted from an instrumental artifact related to small errors in the calibration of the gain of the SQUID amplifier, and was observed in samples where the signal of the magnetic thin film was much weaker than the diamagnetic contribution of the substrate [127, 128]. To remove this artifact (Fig. 2.14(b)), I determined a correction factor for each amplifier setting in order to remove the discontinuities in the raw $m - H$ data that occurred each time the sensitivity of the measurement was changed, as suggested by Ney et al. [127]. The corrections did not exceed 1% of the measured m.

After the background subtraction, I determined the Mn saturation moment, μ_{Mn}, at $T = 2$ K by extrapolating a linear fit to m in the range $\mu_0 H = 2 - 5$ T to $\mu_0 H = 0$ T (Fig. 2.14(b)). The average value calculated from the four linear fits of the two branches is reported for μ_{Mn}.

Remanent moment measurements were mainly used to determine the Curie temperature, T_C. I estimated T_C from the point where $m_r(T)$ drops to zero or to the upper limit of the background level, as discussed before.

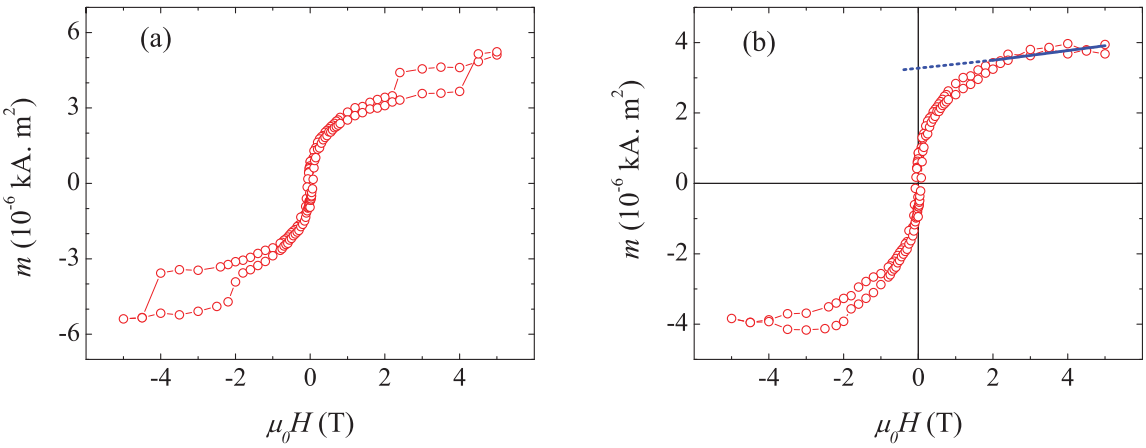

Figure 2.14: $m - H$ data of a Si:Mn sample after subtraction of the substrate background. (a) A discontinuity in the measured moment appeared at high fields. (b) The discontinuities were removed by slightly changing the calibrated values of the gain settings of the SQUID amplifier at the respective fields. The intercept at $\mu_0 H = 0$ T of the linear fit shown in solid blue line determines the Mn saturation moment.

Chapter 3

Structural and Magnetic Properties of Ultrathin Mn Films on Si(001)

In this Chapter, I explore the possibility of stabilizing ultrathin layers of MnSi with a B2 (CsCl) crystal structure. While such a structure is not generally thermodynamically stable, DFT predicted that the epitaxially induced strain of Si(100) can stabilize MnSi-B2 films. DFT showed that Mn atoms in a $1-3$ ML thick silicide film on Si(001) have sizable magnetic moments and a strong ferromagnetic coupling due to a B2-type coordination [32, 54, 55]. Using XAFS and SQUID magnetometry, I present a structural and magnetic characterization of Mn films with a thickness ranging from $0.35-4$ ML grown on Si(001) and capped with a Si layer. XAFS experiments reveal that the structure of the silicide layer that forms depends on the growth temperature of the capping layer. A capping layer grown at 200 °C on 0.35 ML Mn results in a metastable MnSi film with a B2-like phase, whereas a cap grown at room temperature on 0.5 ML Mn followed by annealing at 200 °C produces a MnSi layer with a B20-like structure. Increasing the Mn thickness from 0.5 to 4 ML does not induce a transformation in the structure but drives the Mn into a more ordered MnSi-B20 coordination. The sample with B2-like structure has the largest Mn magnetic moment of 0.33 μ_B at $T = 2$ K, and a T_C above 400 K. MnSi-B20 layers have lower moments and much lower T_C's, in agreement with the values reported for MnSi-B20 thin films.

3.1 Film Growth and Structural Characterization

All samples were grown on boron-doped (1 -20 Ω cm) Si(001) by following the substrate preparation and growth methods described in Chapter 2. After the growth of a 100 nm Si buffer layer, a Mn layer with a thicknesses varying from 0.35 to 4 ML was deposited at a substrate temperature of -15 °C then capped by a 10 to 20 nm Si layer. To be consistent with the studies of Refs. [32, 54, 55], it is convenient to define 1 ML Mn to correspond to the density of atoms in a MnSi-B2 structure, 1.36×10^{19} atoms/m^2. For the sample with 0.35 ML Mn, the Si-cap was deposited at 200 °C. Since initial XAFS results for this sample demonstrated the possibility of MnSi-B2, I tried to stabilize thicker films of this structure. However, to attempt to avoid the bimodal growth of Mn_5Si_3 and MnSi islands that are likely to appear at thicker Mn layers, as reported in Ref. [75] for a 0.5 ML Mn/Si(001) annealed up to 450 °C, I deposited the Si-cap of the $0.5 - 4$ ML samples at -15 °C. To examine the effect of postgrowth annealing on structural ordering and magnetic moment, I annealed the $0.5-4$ ML samples for 1 hour at 200 °C in Ar atmosphere. The annealing temperature was chosen based on XRR study of an amorphous-Si/0.5-ML Mn/Si(001) structure: by annealing up to 250 °C, no significant change in the Mn-Si interfacial roughness was observed. In what follows, I refer to the annealed samples as 0.5-ML-A, 2-ML-A, and 4-ML-A.

In order to rule out significant diffusion of Mn into the Si capping layer (such a behavior was observed in Mn/Ge(100) [129]), I measured the samples with XRR. The simulation of the XRR spectra provides information about the distribution of Mn in Si. The XRR data (Fig. 3.1) was fit using Parratt32 software [130] which is based on Parratt's recursion method [131]. A Gaussian scattering length density (SLD) profile of the Mn-containing regions of the samples was found to give the best fit. The profile was constructed in Parratt32 with a set of uniform layers, each with a thickness of

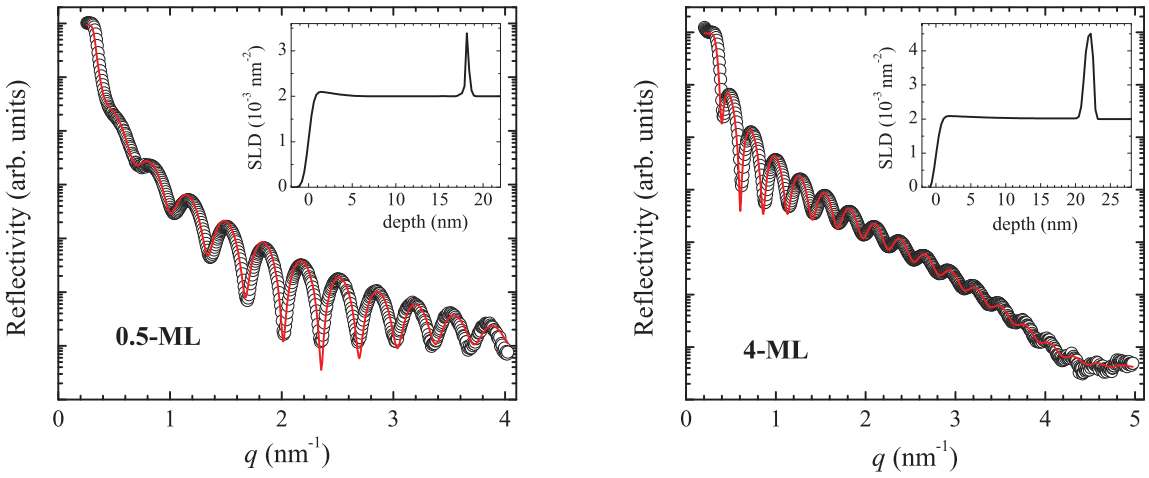

Figure 3.1: Simulations (solid red line) of the XRR data (open circles) of the 0.5-ML and 4-ML samples. The scattering length density (SLD) profile in the insets show that Mn remains at the interface. The data shown is representative of all other samples.

~ 0.15 Å. The insets of Fig. 3.1 show the SLD of the corresponding fits to the data, which demonstrate that the Mn remains localized at the substrate-cap interface. For the 0.5-ML sample, the full width at half maximum of the Mn distribution is about 2 Å, whereas the 4-ML sample has an estimated roughness of 4 Å. These values are comparable to the substrate roughness of 5 Å estimated from atomic force microscopy measurements, and demonstrate the smoothness of the films.

3.1.1 Local Environment of Mn

To investigate the local crystallographic order around Mn atoms, I performed polarization-dependent XAFS measurements in fluorescence mode. Between 20 to 30 x-ray absorption scans, $\mu(E)$, were collected at the Mn K-edge for each in-plane (ip) and out-of-plane (oop) orientation. The k^2-weighted XAFS functions and the corresponding Fourier transform magnitudes, $|FT[k^2\chi(k)]|$, are shown in Fig. 3.2. In addition to the ultrathin samples, I also measured a 5 nm-thick single-crystal MnSi film grown on Si(111) by solid phase epitaxy [119]. This served as a reference MnSi-B20 structure and for the determination of the two XAFS parameters: the amplitude reduction

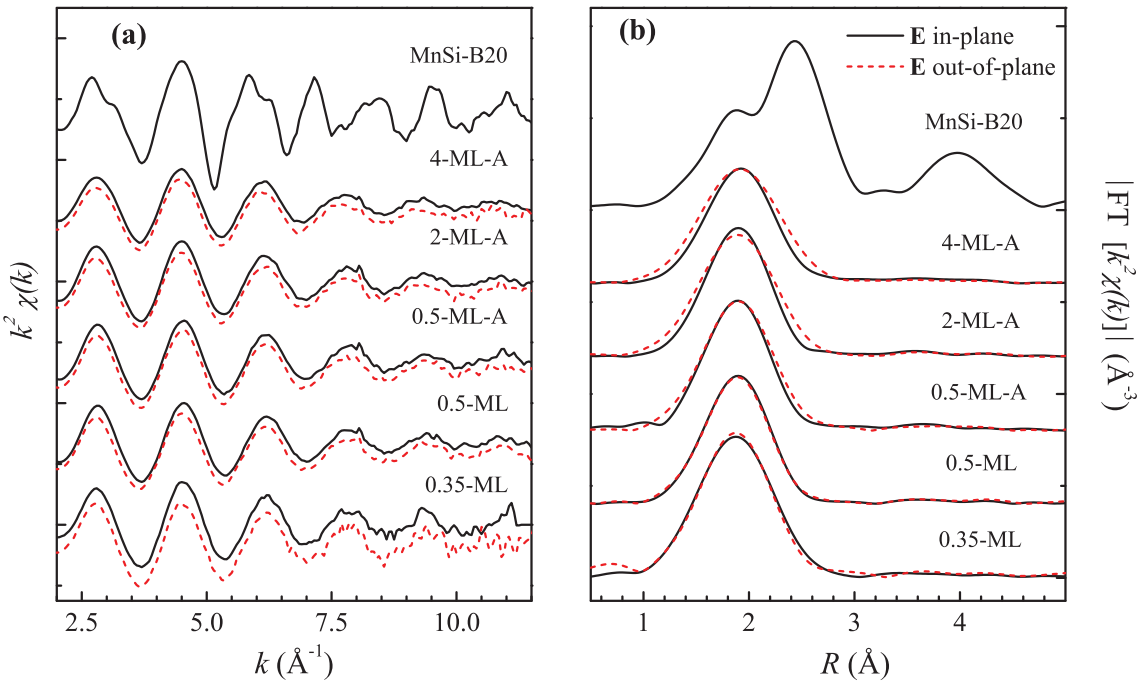

Figure 3.2: (a) k^2-weighted XAFS interference functions of all measured samples and the reference MnSi-B20 sample. (b) Magnitude of the Fourier transformed $k^2\chi(k)$. In-plane (solid black lines) and out-of-plane (dashed red lines) are shown.

factor S_0^2 and the energy shift ΔE_0. I fit the experimental data in R-space within the range $1.13 - 2.82$ Å ($1.10 - 3.00$ Å for the MnSi-B20 reference) to theoretical XAFS models calculated with FEFF8.2 [118]. The B20 model was the starting structure to fit the in-plane and out-of-plane data for each of the $0.35 - 4$ ML samples. Mn in a B20 structure has a first shell composed of seven Si neighbors: one at 2.305 Å, three at 2.536 Å and three at 2.402 Å, and a second shell with six Mn neighbors at 2.796 Å. Due to the relatively limited $\Delta(k)$ range, it was not possible to resolve the three separate bond lengths in the first Si shell. Therefore, I used the single scattering path with the largest scattering amplitude of the calculated B20 model to fit the seven Si neighbors of the first shell, which appears at $R \sim 1.9$ Å in Fig. 3.3. The second Mn-Mn shell was also included in the fit shown in Fig. 3.3.

Although the $|FT[k^2\chi(k)]|$ of the ultrathin films (Fig. 3.2(b)) show a single peak that is predominantly due to Mn-Si first shell, a second Mn-Mn scattering path was

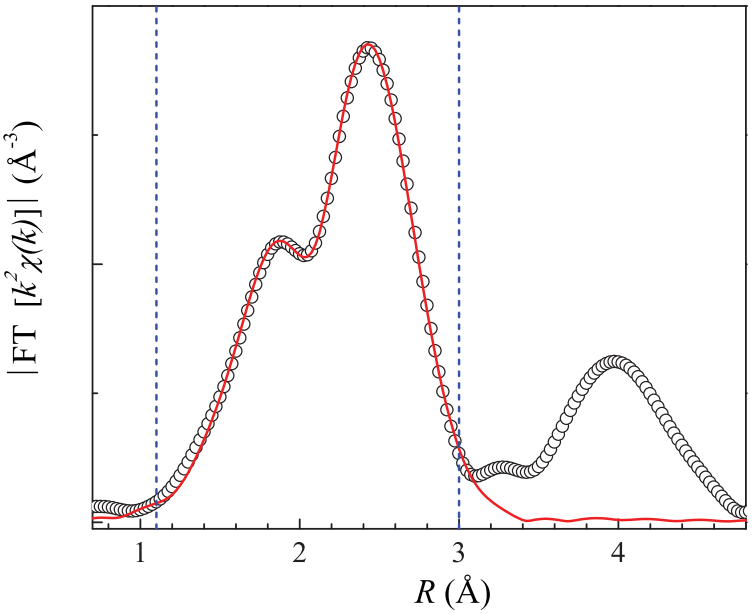

Figure 3.3: XAFS data of MnSi-B20 reference sample (open circles) and the corresponding fit (solid red line). The fitting range is within the dashed blue lines. The peak at $R \sim 1.9$ Å corresponds to the first Si shell containing all 7 Si neighbors and the second peak at $R \sim 2.4$ Å is for the second Mn shell. In the Fourier transform the peaks appear at shorter distances from the actual bond lengths due to the phase shift in $\chi(k)$.

needed in order to obtain a good fit to the experimental data. The contribution of the Mn second shell is evident from the overlays of Fig. 3.4, which show a broadening of the Mn-Si peak above $R \sim 2.2$ Å when the Mn thickness increases.

Figure 3.5 shows fits to the ultrathin samples with the coordination number N_i, path length R_i, and mean square relative displacement σ_i^2, treated as fitting parameters for the two scattering paths, Mn-Si ($i = 1$) and Mn-Mn ($i = 2$). The amplitude reduction factor $S_0^2 = 0.70 \pm 0.02$ and the energy shift $\Delta E_0 = 5.9 \pm 0.6$ eV were fixed to the values obtained from the MnSi-B20 reference sample. A simultaneous fit to a k^1- and k^2-weighted model reduced the correlation between N_2 and σ_2^2. The uncertainties of the fitting parameters shown in Table 3.1 were estimated by the double χ^2_{min} method, fixing one parameter and allowing the remaining parameters to float [124, 125]. Although, this method may be underestimating the errors in R_1.

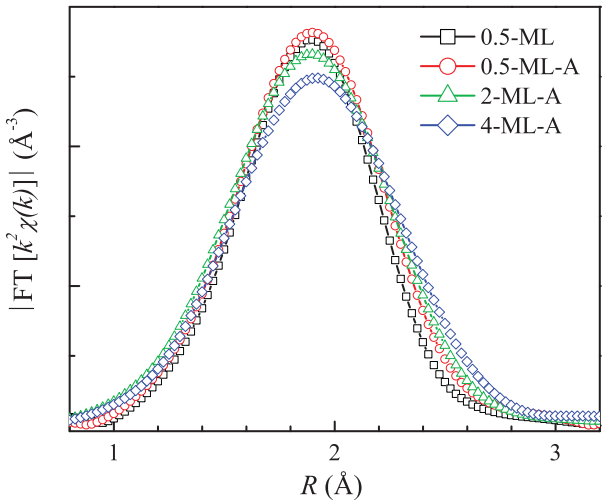

Figure 3.4: The overlays of the out-of-plane XAFS data show a broadening in the main peak above $R \sim 2.2$ Å as the Mn thickness is increased from 0.5 to 4 ML. The broadening is due to the contribution from Mn-Mn scattering path.

Sample	N_1 (Si)	R_1 (Å)	σ_1^2 (Å^2)	A_{Mn-Mn} (%)	R_2 (Å)	R (%)
MnSi-B20 ref.	6.5	2.39(1)	0.0104(4)	100	2.788(6)	1.88
0.35-ML_ip	7.7(4)	2.365(5)	0.0096(8)	9.2	2.79(1)	0.47
0.35-ML_oop	7.0(6)	2.367(4)	0.008(1)	13.2	2.82(2)	0.82
0.5-ML_ip	7.0(4)	2.363(2)	0.0097(7)	10.5	2.78(1)	0.84
0.5-ML_oop	7.1(5)	2.375(3)	0.0097(9)	9.4	2.81(1)	1.07
0.5-ML-A_ip	6.6(9)	2.363(6)	0.009(2)	14.2	2.79(3)	2.35
0.5-ML-A_oop	6.9(3)	2.372(2)	0.0094(6)	13.0	2.78(1)	0.48
2-ML-A_ip	6.9(4)	2.371(3)	0.0092(7)	14.8	2.81(1)	1.09
2-ML-A_oop	6.8(7)	2.381(4)	0.010(2)	14.1	2.80(2)	0.85
4-ML-A_ip	6.2(4)	2.384(3)	0.010(1)	18.5	2.78(1)	0.92
4-ML-A_oop	6.4(7)	2.391(5)	0.011(2)	17.3	2.77(3)	0.78

Table 3.1: Coordination numbers (N) and distances (R) obtained from the fit of the in-plane (ip) and out-of-plane (oop) XAFS data of the samples and the ip data of the MnSi-B20 reference. A_{Mn-Mn} is the area under the Mn-Mn profile function relative to that of Mn-Si. The percent residual (R%) and the uncertainty in the last digit of each fitting parameter (in parentheses) are also included.

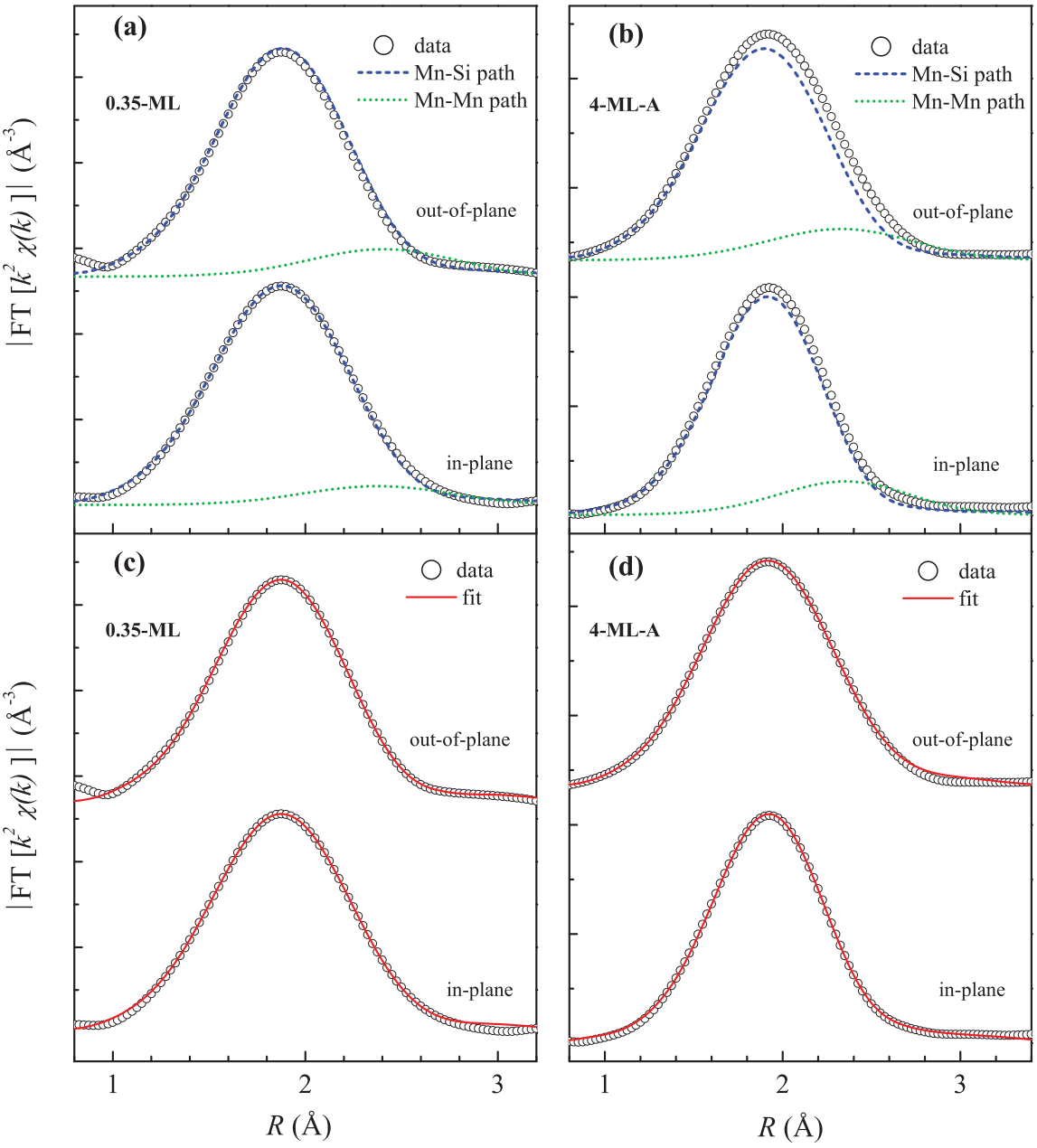

Figure 3.5: In-plane and out-of-plane XAFS data of the 0.35-ML and 4-ML-A samples. (a) and (b) show the profile functions of the Mn-Si and Mn-Mn scattering paths that were combined to obtain the final fits of the experimental data shown in (c) and (d).

The results of Table 3.1 reveal only a subtle difference between the XAFS parameters of the 0.35-ML sample and the $0.5 - 4$-ML samples. The difference between the samples is more clearly shown in Fig. 3.6, which shows a departure of the fit parameters for the 0.35-ML relative to the other samples. In particular, the coordination number $N_{1-ip} = 7.7 \pm 0.4$ of the 0.35-ML sample is more than a standard deviation higher than the other samples and there is no splitting in the in-plane $R_{1-ip} = 2.365$ Å and out-of-plane $R_{1-oop} = 2.367$ Å of the Mn-Si bond lengths. It is unclear why $N_{1-oop} = 7.0 \pm 0.6$ is less than N_{1-ip}, but an $N_{1-ip} = 7.7 \pm 0.4$ is within error of a coordination $N = 8$. The value obtained for N_{1-ip} and R_1 for the 0.35-ML are consistent with the first Si shell of a B2 structure that is pseudomorphic with the Si(001) substrate. The difference between the in-plane second shell radius, $R_{2-ip} = 2.79$ Å, and the out-of-plane Mn-Mn distance, $R_{2-oop} = 2.82$ Å, implies a 2% tetragonal distortion of the unit cell. However, R_{2-ip} is larger than half the Si lattice constant ($a_{Si}/2 = 2.716$ Å), the value expected for a B2 structure that is pseudomorphic with the Si substrate, which suggests that there is a distortion of the Mn sites relative to a tetragonal B2 structure.

The sensitivity of Mn to growth conditions is illustrated by the difference between the structures of the 0.35-ML sample and that of the samples grown with a cold capping layer. In contrast to the 0.35-ML sample, an inspection of the coordination numbers and bond lengths indicates that the 0.5-ML, 0.5-ML-A, 2-ML-A, and 4-ML-A samples evolve toward a B20-like structure as the Mn thickness is increased, as illustrated in Fig. 3.6. No significant structural transition is observed as the thickness is increased from 0.5 to 4 ML, nor between the annealed and unannealed 0.5-ML samples. The N_1 is approximately constant as a function of thickness and is within error of the effective coordination number $N_1 = 6.5$ of the MnSi-B20 reference sample. The Mn-Si bond length increases gradually with thickness and reaches a value equal to the average bond length $R_1 = 2.387$ Å for the 4-ML-A sample. Moreover, there

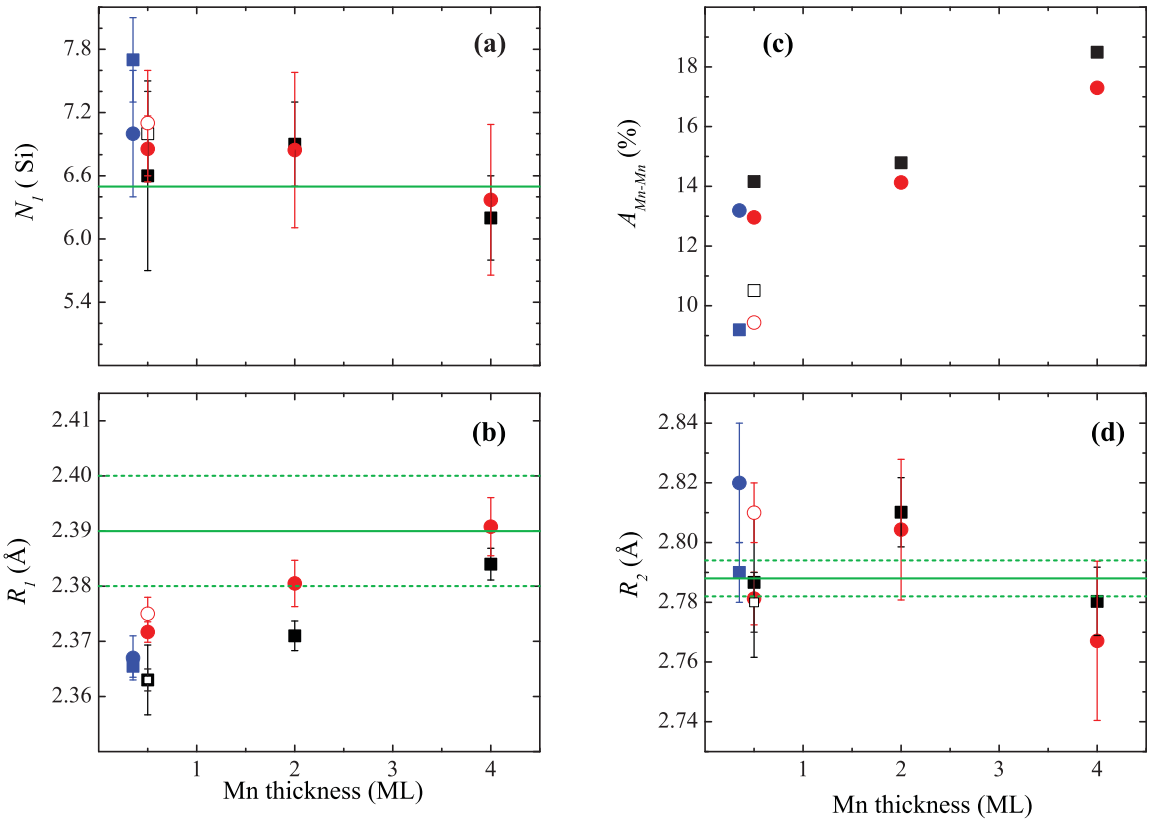

Figure 3.6: Variation of XAFS fitting parameters with Mn thickness. (a) and (b): parameters of the first Mn-Si shell. (c) and (d): parameters of the second Mn-Mn shell. Squares (circles) represent the in-plane (out-of-plane) data and open symbols correspond to the nonannealed 0.5-ML sample. Solid (green) horizontal line corresponds to the MnSi-B20 reference with the associated uncertainty indicated by the dashed lines.

is a clear splitting between R_{1-ip} and R_{1-oop}, indicative of a difference in structure between this set of samples and the 0.35-ML sample. The Mn-Mn bond is also within error of the B20 reference sample. Given the weak second shell of Mn and the strong correlation between N_2 and σ_2^2, I could not determine a value for N_2. Instead, I use the area under the Mn-Mn profile function, A_{MnMn}, as a measure of the relative combined change in N_2 and σ_2^2. The XAFS measurements of the as-grown and postgrowth annealed 0.5-ML sample show that the annealing mostly affects the Mn-Mn shell, without a noticeable change to the Mn-Si shell. The increase in A_{MnMn} is due to an increase in the Mn coordination number and/or a decrease in the structural disorder, although the correlation between N_2 and σ_2^2 prevents a separation of these two contributions. However, one can interpret the increase in A_{MnMn} with annealing and also with increasing thickness as an indication that the system is being driven towards a more ordered B20 structure, although the weak presence of the Mn shell and an absence of a peak in the magnitude of the Fourier transform corresponding to the third nearest neighbor shell indicate a significant disorder in the layers.

Given the 400 °C temperature used to create MnSi layers on Si(111) by solid phase epitaxy, it is not surprising that the MnSi layers are disordered. The poor lattice mismatch between MnSi(001)-B20 and Si(001) is likely another contributing factor. A similar observation was reported for Mn^+ implanted Si(001) in Ref. [68], where MnSi precipitates with a disordered B20 coordination were achieved after annealing at 337 °C.

The XAFS results show that the growth mode of the Si cap affects the incorporation of Mn into the layer and leads to distinct MnSi structures. While DFT calculations [54] and scanning tunneling microscopy (STM) experiments [63] show that the subsurface interstitial sites are more favorable for Mn on Si(001), STM measurements on Mn deposited at room temperature show that Mn adatoms are energetically inhibited from populating these sites at room temperature and instead form chains

on the surface [72, 73]. By annealing the sample prior to the deposition of the Si cap, Mn atoms are driven into the preferred subsurface interstitial sites where the surrounding Si atoms and interstitial Si atoms provided by the subsequent addition of the Si cap lead to the formation of the B2-like phase. However, by depositing the capping layer prior to annealing, STM measurements suggest that Mn is prevented from accessing the silicon interstitial sites, which enables it to form MnSi-B20 with the Si in the capping layer.

3.2 Magnetic Properties of the Ultrathin Mn/Si(001) Films

The magnetic properties of the as-grown and annealed samples were measured using a SQUID magnetometer. I measured the remanent moment as a function of temperature, $m_r(T)$, after saturating the sample in a 5 T applied field at $T = 2$ K, and measured the $m - H$ loops in a field applied parallel to the [110] direction of the thin films. The diamagnetic and paramagnetic contributions of the boron-doped Si substrate were subtracted from each $m - H$ curve according to the method described in Chapter 2, and the Mn magnetic moment was extracted from a fit to the linear region of $m - H$ above $\mu_0 H = 1$ T. All reported values of Mn saturation moment μ_{Mn} are from measurements performed at $T = 2$ K.

There is a clear difference between the magnetic response of the B2-like sample compared to that of the B20-like samples. In Fig. 3.7, I show the $m - H$ loops of the 0.35-ML and 4-ML-A samples measured at T = 2 K. The shape of the $m - H$ curve of the 4-ML-A sample is representative of all as grown and annealed $0.5 - 4$-ML samples. The insets of Fig. 3.7 show a remanent moment indicative of long-range magnetic order. The 0.35-ML sample with the B2-like structure, has a saturation field $\mu_0 H_{sat} = 0.12$ T and a coercive field of approximately 10 mT (inset of Fig. 3.7(a)). The calculated Mn magnetic moment is 0.33 μ_B for the B2-like sample. In contrast, the $m - H$ loops of the B20-like structures are more rounded with a much higher

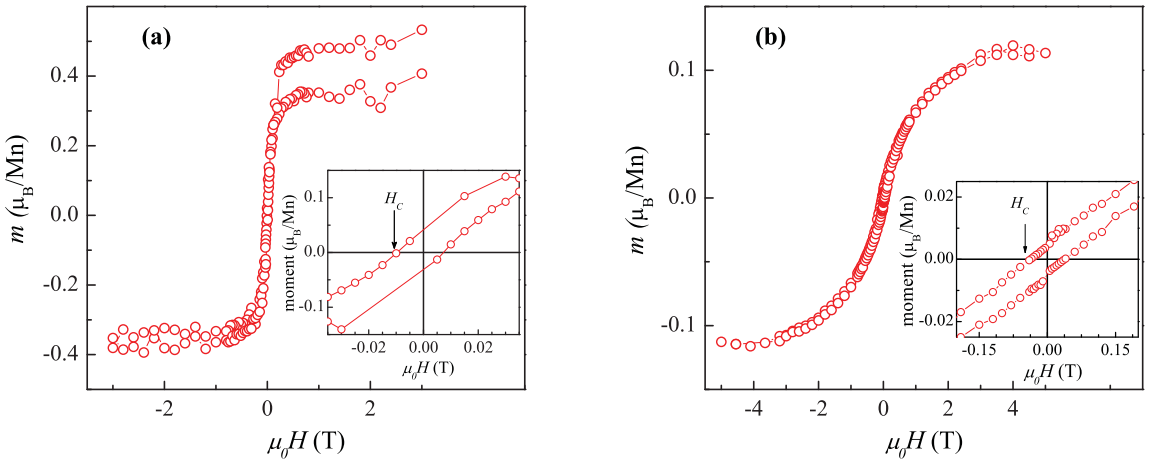

Figure 3.7: Hysteresis loops of the (a) 0.35-ML and (b) 4-ML-A samples measured at $T = 2$ K. The substrate background has been subtracted. Insets show the remanent moment and the coercive field for each sample. The "jump" in the moment seen in the top branch in (a) is an instrumental artifact caused by a change in the emu-range during the measurement as discussed in Chapter 2 and Ref. [127]

$\mu_0 H_{sat} = 1.8$ T and a larger coercive field, which is $\mu_0 H_c = 35$ mT in the case of the 4-ML-A sample. The fact that $\mu_0 H_c$ is much larger than the 5 mT coercive field of B20-MnSi/Si(111) [119] is consistent with the large disorder inferred from the XAFS fits.

There is a dramatic difference between the Curie temperatures of the B2- and B20-like structures. Due to the large susceptibility of the substrate, the clearest estimates of the T_C come from measurements of the remanent moment, $m_r(T)$, where there is no substrate contribution. I estimated T_C from the point where $m_r(T)$ goes to zero or to the background level of each sample (Fig. 3.8). For the B20-like structures, the estimated T_C drops with increasing thickness: $T_C = 18$ K for the 0.5-ML-A sample, $T_C = 13$ K for the 2-ML-A and $T_C = 4$ K for the 4-ML-A sample. These low values for T_C are expected from a B20 structure, where the bulk T_C is only 29.5 K. A combination of finite-sized effects [132] and the influence of defects [119] accounts for the difference between the ultrathin film measurements and bulk. However, the origin of the drop in T_C with thickness is not clear. These low Curie temperatures are in

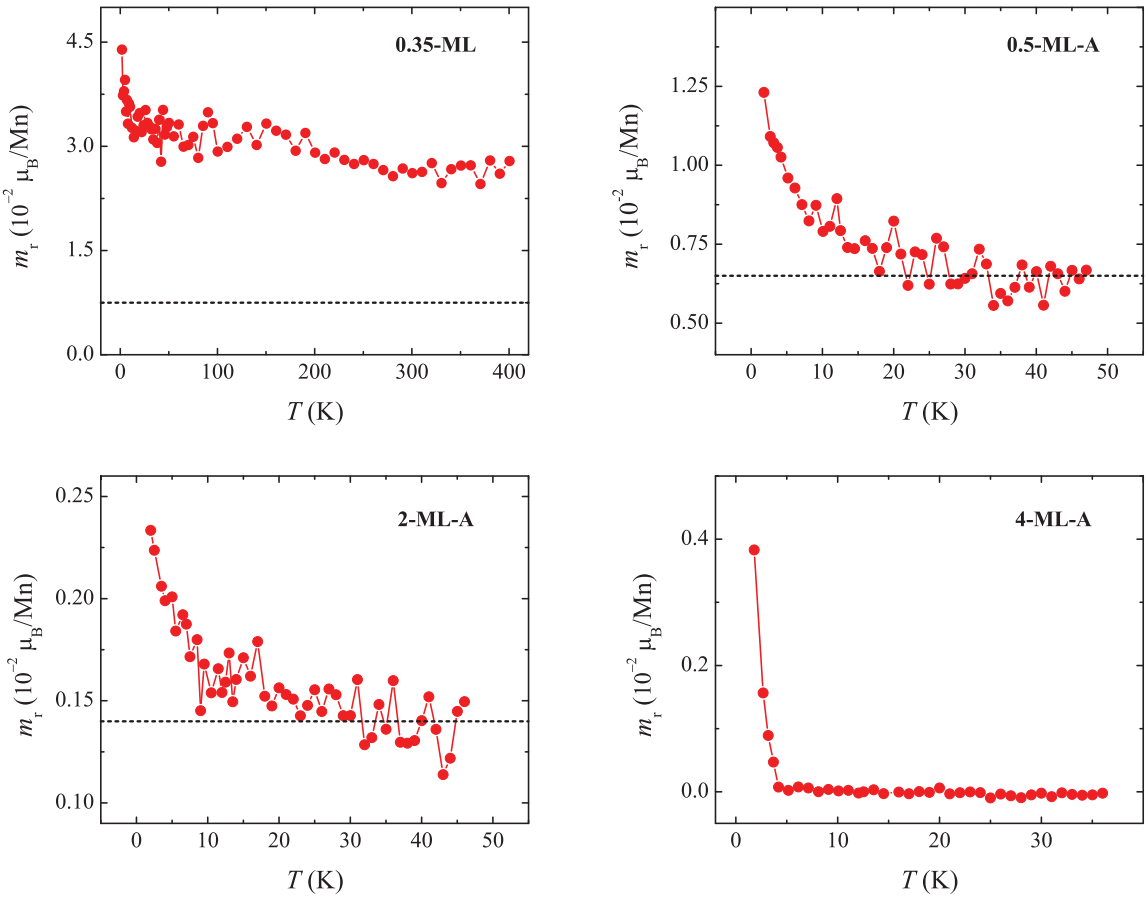

Figure 3.8: Remanent moment m_r as a function of temperature for the samples with indicated Mn thickness. For the samples with Mn $\geq$ 0.5 ML, the measurements were interrupted when the value of the magnetic moment reached zero or the background level which is indicated by the dashed lines. The 0.35-ML sample with a MnSi-B2-like structure has a $T_C > 400$K.

stark contrast to the B2-like sample, which shows a slower decay of $m_r(T)$ with a T_C that is above the maximum measurable temperature of 400 K. This high T_C is in reasonably good agreement with the predictions of Ref. [55].

The growth temperature of the Si capping layer influences the local chemical environment of the Mn atoms. I find that the magnetic properties are most strongly correlated with the A_{Mn-Mn} parameter of the XAFS fit, which points to the Mn-Mn shell as most important for determining the magnetic interactions. An increase in A_{Mn-Mn} due to annealing is correlated with the increase in Mn magnetic moment,

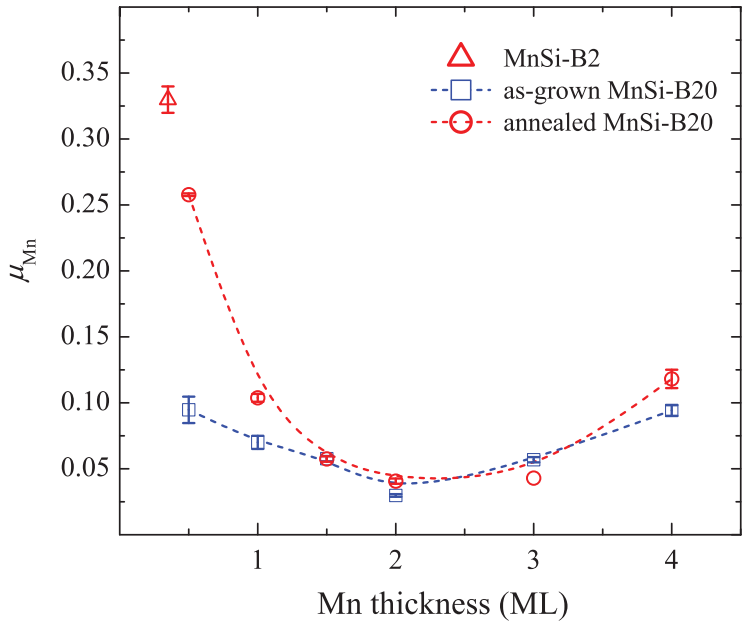

Figure 3.9: Variation of Mn magnetic moment with thickness. The largest moment is measured for the sample with MnSi-B2-like structure. Postgrowth annealing at 200 °C generally increases the moment of the samples with B20-like structure. The same trend is observed for as-grown and annealed samples when the Mn thickness increases from 0.5 to 4 ML.

as shown in Fig. 3.9. The largest increase is observed for the thinnest MnSi-B20 sample, presumably because the redistribution of its low Mn content during the annealing experiences a larger influence from the single crystal substrate, as compared to the thicker samples whose Mn may be more strongly affected by the disordered amorphous cap. For the 0.5-ML sample, an increase in A_{Mn-Mn} from 10% to 13.5% after annealing coincides with an increase in the moment from 0.09 to 0.26 μ_B. Some insight into the magnetic structure of the B20-like films can be obtained from the thickness dependence of the saturated moment shown in Fig. 3.9. The moment drops from 0.26 μ_B, to approximately 0.05 μ_B between 2 and 3 ML before it increases again at 4 ML. A similar nonmonotonic thickness dependence is observed for MnSi/Si(111) films [119] and is explained in part by the results of DFT calculations that predict an enhanced interfacial moment [133]. The drop seen in the 2 and 3 ML films is then attributed in part to the formation of bulk moments. A second possible contribution

to the drop in the moment is due to the presence of defects. A third possibility is the formation of an antiferromagnetic state. For MnSi/Si(111), a magnetic configuration with large uncompensated interfacial moments that are antiparallel to smaller central moments is found to be nearly degenerate with the ferromagnetic state [119]. The drop in magnetic moment could possibly be due to the formation of antiparallel spins in the interior of the film. The more ordered 4-ML film has a higher moment presumably due to fewer defects and a more highly coordinated Mn shell.

More insight about the correlation between the structure and magnetism of the ultrathin Mn layers can be inferred from a comparison with the DFT calculations. The finding that a Si capping layer influences the structure and magnetism is similar to the DFT predictions of Refs. [32, 54, 55], which demonstrate that a Si capping layer is essential to stabilize a B2 structure and plays an important role in switching the Mn/Si(001) system from antiferromagnetic in the absence of a Si cap, to ferromagnetic when the Mn layer is capped with Si. The capping layer in the DFT model is provided by Si of the topmost surface layer, given that Mn diffuses to its preferred second-layer subsurface interstitial sites. DFT demonstrates that the Mn-Si coordination leading to an itinerant $sp-d$ exchange is at the origin of the ferromagnetic ordering. The hybridization due to the covalent Mn-Si bonding broadens the Mn $3d$ bands and couples neighboring Mn and Si antiferromagnetically, which in turn leads to a ferromagnetic alignment of the next-nearest neighbor Mn spins. The exchange coupling between Mn is therefore dependent on their distance and the number of neighboring Si atoms. It is shown that the $sp-d$ interaction competes with a direct $d-d$ exchange interaction between Mn as the number of Si neighbors decreases. In the limiting case where, instead of a silicide layer, a thin Mn layer forms on Si(001), the $d-d$ exchange interaction is more effective and antiferromagnetic coupling becomes energetically more favorable. This DFT study possibly explains the trend observed in Fig. 3.9. The XAFS results in Fig. 3.6 show that the Mn-Si coordination decreases

with increasing thickness, whereas the Mn-Mn shell either increases in coordination or becomes more ordered. According to DFT, these trends would decrease the $sp-d$ hybridization, and increase the $d-d$ interaction that would drive the structure from a ferromagnetic phase to an antiferromagnetic phase with increasing thickness.

Given that the samples discussed in this study contain precipitates, it is also interesting to comment on the structural stability of the thin Mn layers determined by DFT. The study of Ref. [54] shows that for a Mn coverage less than or equal to 2 ML, the decomposition of the films into 3D islands with variable thicknesses is more favorable than the formation of homogeneous layers. It is interesting that the structural transition at 2 ML predicted by DFT is approximately the thickness above which the XAFS results show the MnSi films to have a more B20-like character. Furthermore, the SQUID results show that μ_{Mn} increases with thickness after reaching its lowest value at 2 ML. Although the Mn magnetic moment in a tetragonally distorted MnSi-B2 is estimated to be at least 0.8 μ_B [55], the low value of 0.33 μ_B for the MnSi-B2 structure of the 0.35 ML sample could be due to the disorder in the structure or to antiferromagnetic regions if the films form 3D islands that are a few ML thick.

Overall, the growth of a high-T_C ferromagnetic structure by "dusting" Mn at the Si interface is an interesting finding. However, as this study showed, it is important to grow the Si capping layer at high temperature to maintain its crystalline structure and reduce defects that affect the magnetism of the thin Mn films.

Chapter 4

Surfactant Mediated Growth of Mn δ-doped Si

In this chapter, I investigate the influence of a Pb surfactant on the local structure and magnetism of Mn δ-doped layers in Si(001). XAFS, RBS, TEM and SQUID magnetometry were employed in this study. The complementary data obtained from these techniques show that Pb has a significant effect on the structural and magnetic properties of the submonolayer of Mn when the Si capping layer growth temperature, T_{Si}, and the Mn coverage, θ_{Mn}, are varied. The results presented in this chapter identify three regions in the growth-phase-diagram characterized by distinct magnetic behaviors and crystal structures. In one region, XAFS and TEM experiments indicate that MnSi nanocrystallites form with a B2-like crystal structure. At the optimal growth conditions, $T_{\mathrm{Si}} = 200$ °C and $\theta_{\mathrm{Mn}} = 0.26$ monolayer (ML), a ferromagnetic phase develops with a Curie temperature $T_C > 400$ K and a Mn saturation moment $\mu_{Mn}= 1.56\ \mu_B$, whereas T_C drops to zero for a control sample prepared without Pb. For $T_{\mathrm{Si}} > 200$ °C, large nano-disks with a MnSi-B20 type structure form with a $T_C \simeq 170$ K. RBS shows that the increase in the remanent magnetization in these two phases is possibly correlated with an increase in the Mn substitutional fraction, which suggests that a $\mathrm{Si}_{1-x}\mathrm{Mn}_x$ dilute magnetic semiconductor may be forming in the matrix between the precipitates.

Density functional theory (DFT) calculations are performed to give insight into the role of the surfactant. The calculations show that Pb changes the pathway by which the Mn atoms access the Si substitutional sites, $\mathrm{Mn_{Si}}$. While the Pb increases the formation energy of $\mathrm{Mn_{Si}}$ at the Si surface, it enables substitutional incorporation

by lowering the formation energy of Si vacancies by 0.92 eV.

The RBS measurements and data analysis discussed in this chapter were conducted by Prof. Sjoerd Roorda at Université de Montréal, whereas the TEM measurements were performed by Prof. Michael Robertson at Acadia University. Dr. Junyi Zhu at the National Renewable Energy Laboratory performed the DFT calculations.

4.1 MBE Growth and Structural Characterization of Mn δ-doped Si Layers

The magnetic properties and structural evolution of the δ-doped layers were investigated for a range of Mn coverage 0.26 ML $\leq \theta_{\mathrm{Mn}} \leq$ 0.86 ML and Si cap growth temperature 150 °C $\leq T_{\mathrm{Si}} \leq$ 300 °C. Here, I define 1 ML to correspond to the density of atoms in the Si(001) plane (6.78×10^{19} atoms/m^2). The Mn δ-doped films were grown on low resistivity (1-20 Ω cm) and high resistivity (600-1200 Ω cm) boron-doped Si(001) substrates. Prior to thin film growth, a 20 nm Si buffer layer was deposited at 600 °C onto a (2×1) Si(001) surface, followed by the deposition of 2 ML of Pb at room temperature. I measured the Pb coverage by reflection high-energy electron diffraction (RHEED) intensity oscillations. By the completion of the second Pb layer, a (2×1) reconstruction of the surface was recovered, as expected for 2 ML Pb/Si(001) [102, 103]. Before the deposition of the submonolayer of Mn, I lowered the substrate temperature to $T < 0$ °C and monitored the Mn flux rate with the ionization gauge, as discussed in Chapter 2. The amount of deposited Mn was subsequently measured with RBS. A 12.4 nm-thick Si layer grown at the substrate temperature T_{Si} capped the Mn layer. *Ex-situ* x-ray photoelectron spectroscopy and RBS measurements confirmed that Pb segregated to the surface during the growth

of the Si capping layer, and RHEED diffraction patterns showed that the cap remained crystalline throughout the growth. I also prepared control samples without a Pb layer in order to determine how the Pb affects the Mn incorporation and the magnetic properties. A description of the samples prepared for this study is shown in Table 4.1.

Table 4.1: Samples and their corresponding Mn coverage θ_{Mn}, Si cap growth temperature T_{Si} and region in the growth-phase-diagram (see Fig. 4.3). I refer to the samples as listed in the first column.

Sample	$\theta_{\mathbf{Mn}}$ (ML)	$T_{\mathbf{Si}}$ (°C)	**region**
a_1	0.26	200	A
a_2	0.32	200	A **(No Pb)**
b_1	0.59	200	B
b_2	0.68	200	B
b_3	0.7	200	B **(No Pb)**
c_1	0.26	250	C
c_2	0.41	250	C
c_3	0.49	250	C **(No Pb)**
c_4	0.86	250	C
c_5	0.33	300	C

The Mn dopant concentration and the fraction of Mn atoms that occupy Si substitutional sites (x_{sub}) were determined from RBS spectra measured in random and channeling orientations, as described in Chapter 2. The 2 MeV He ion beam was directed along the [100] direction of the sample and two detectors were used during the measurement: a wide angle detector (WAD) measured the ion yield backscattered through an angle close to 170°, and a glancing angle detector (GAD) collected ions with grazing incidence. Since the WAD measurements are less prone to small changes in geometry, fits to the WAD data were used to calculate the amount of Mn and x_{sub}, whereas the values obtained from GAD were employed to determine the depth of the Mn layer. The Mn concentrations calculated from random orientation spectra

(Mn_{random}) are usually more reliable than the Mn amounts determined from channeling orientation ($Mn_{channel}$) because they are compared to the Si random height, whereas the channeled spectra depend on the less reliable charge normalization to extract the Mn concentration. Therefore, the values of x_{sub} were verified by using the signal from Pb as a reference, assuming that the Pb peak does not allow channeling:

$$x_{sub} = 1 - \frac{Pb_{random}}{Pb_{channel}}(\frac{Mn_{channel}}{Mn_{random}}), \tag{4.1}$$

where Pb_{random} and $Pb_{channel}$ are the Pb concentrations determined from the random and channeled orientations spectra, respectively. As a further check on the reliability of charge integration, and specifically for control samples without Pb, the minimum ion yield measured from the spectrum height from ions scattered deep in the Si was also calculated and found to lie within the expected range of 4-5% for a well channeled spectrum. Note that in a channeling experiment the incident ions tend to travel in the center of the channel, which enhances the probability of backscattering from interstitial Mn. This is referred to as *flux peaking*. Due to flux peaking, the channeled signal overestimates the amount of interstitial Mn and, consequently, the calculated substitutional Mn fractions should be interpreted as lower threshold values [134].

The local coordination of Mn was determined from XAFS measurements carried out in fluorescence mode. The polarization-dependent XAFS spectra were collected in-plane (ip) and out-of-plane (oop) at the Mn K-edge and the experiments and data analysis were conducted as outlined in Chapter 2. To extract the coordination parameters, I fit the magnitude of the Fourier transform (FT) of the k^2-weighted XAFS interference function $\chi(k)$, $|FT[k^2\ \chi(k)]|$, in R-space (Fig. 4.1). Due to the increase in the noise level of $k^2\ \chi(k)$ for $k > 10.0$ Å^{-1} (see insets of Fig. 4.1), the

FT was limited to within the closest zero-crossing of the k-range $= 2.3 - 10.0$ Å^{-1}. To obtain a good fit to the data, I included two scattering paths that corresponded to the first Mn-Si shell and the second Mn-Mn shell, with the exception of sample b_1-ip, which could only be fit with two separate Mn-Si shells. In order to confirm the composition of the two shells, the equations derived from XAFS *beats theory* in Refs. [135, 108] were applied to calculate the difference in radii between the first two shells, $\Delta R = R_2 - R_1$. The values found were consistent with the ΔR obtained from the best fit values of R_1 and R_2.

I report the XAFS parameters of the δ-doped samples in Table 4.2. For comparison, I also include the parameters of the 5 nm MnSi/Si(111) reference sample with a B20 crystal structure, analyzed in Chapter 3, as well as the parameters expected for Mn in a Si substitutional site (Mn_{Si}) and for Mn in a tetragonally distorted MnSi-B2 structure. For Mn_{Si}, I consider one substitutional Mn atom in the Si lattice since $\theta_{Mn} < 1$ ML. In this case, the second shell corresponds to Mn-Si with $R_2 = 3.84$ Å, which is outside the fitting range and therefore is not included in the table. The amplitude reduction factor $S_0^2 = 0.70 \pm 0.02$ and the energy shift $\Delta E_0 = 5.9 \pm 0.6$ eV were fixed to the values obtained from the reference MnSi-B20 sample. Due to the weak contribution from the second Mn-Mn shell and the strong correlation between the coordination number N_2 and the mean square relative displacement σ_2^2 of the measured samples, it was not possible to determine a value of N_2. As described in Chapter 3, I refer to the area under the Mn-Mn profile function, $A_{\text{Mn-Mn}}$, to represent the relative combined change in N_2 and σ_2^2. A comparison between the measured XAFS spectra and the $|FT[k^2\ \chi(k)]|$ functions calculated for MnSi-B2, MnSi-B20 and Mn_4Si_7 structures is shown in Fig. 4.2.

The structure of the samples was further characterized with plan view and cross-sectional TEM. The samples were prepared by low-angle mechanical polishing and subsequently cleaned with Ar-ion milling [136] before being imaged with 300 kV

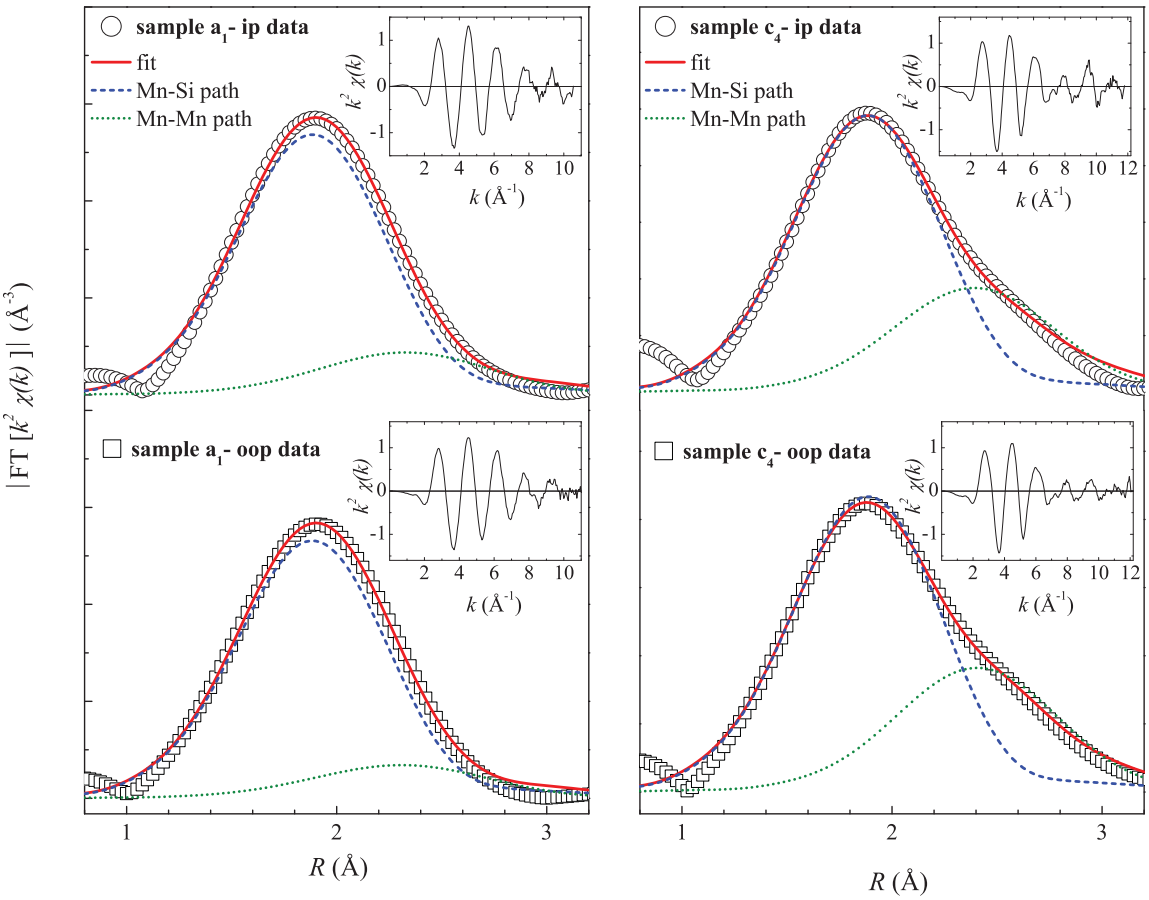

Figure 4.1: In-plane (ip) and out-of-plane (oop) XAFS data and corresponding fit in R-space for samples a_1 (left) and c_4 (right). Profile functions of Mn-Si and Mn-Mn scattering paths are shown for each sample and the fitting range is within $R = 1.40 - 2.82$ Å. Insets show the k^2-weighted XAFS interference function in k-space. The curves are representative of other XAFS measurements discussed in the text.

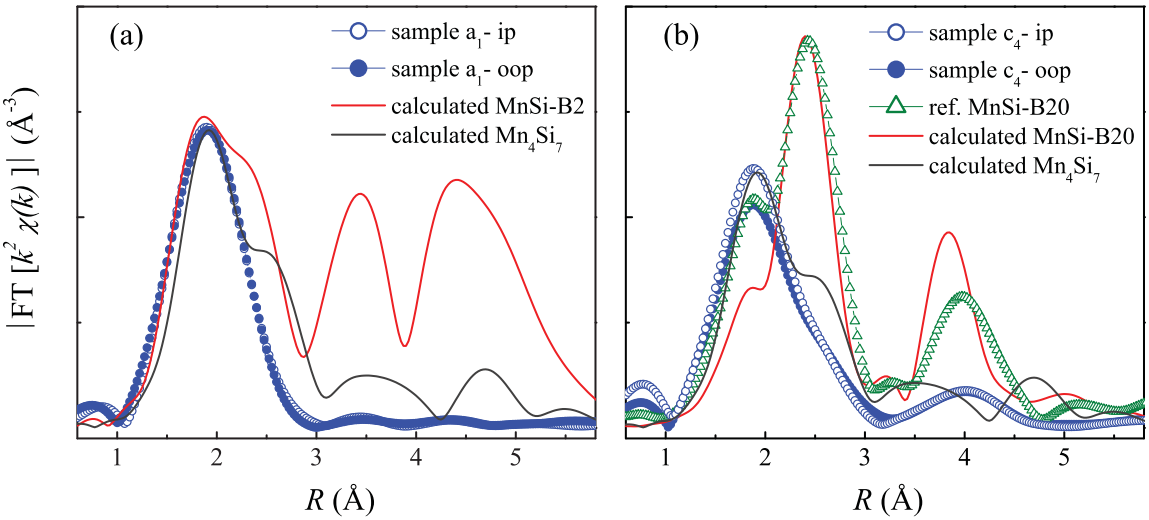

Figure 4.2: Qualitative comparison of the $|FT[k^2\ \chi(k)]|$ of samples (a) a_1 and (b) c_4 with the calculated $|FT[k^2\ \chi(k)]|$ of MnSi-B2, MnSi-B20 and Mn_4Si_7 structures. The same window function and similar k-range were used to Fourier transform the calculated structures, and their $|FT[k^2\ \chi(k)]|$ were scaled to match either the Si (MnSi-B2 and Mn_4Si_7) or the Mn (MnSi-B20) peak of the measured spectra.

Samples	N_1 (Si)	R_1 (Å)	σ_1^2 (Å^2)	N_2 (Mn)	R_2 (Å)	σ_2^2 (Å^2)	$A_{\text{Mn-Mn}}$ (%)	R (%)
a_1**-ip**	6.7(7)	2.37(1)	0.009(2)	-	2.76(2)	-	18.8	1.04
a_1**-oop**	7(1)	2.378(5)	0.010(2)	-	2.75(3)	-	15.0	1.14
b_1**-ip**	2(1)	2.22(3)	0.006	7(1)**(Si)**	2.42(2)**(Si)**	σ_1^2	-	2.61
b_1**-oop**	6.1(8)	2.38(1)	0.008(2)	-	2.80(1)	-	21.4	0.91
b_3**-ip (No Pb)**	7.7(4)	2.365(5)	0.0096(8)	-	2.79(1)	-	9.2	0.47
b_3**-oop (No Pb)**	7.0(6)	2.367(4)	0.008(1)	-	2.82(2)	-	13.2	0.82
c_4**-ip**	6.3(6)	2.38(1)	0.010(2)	-	2.817(5)	-	41.0	1.11
c_4**-oop**	6.3(6)	2.38(1)	0.012(1)	-	2.829(4)	-	44.9	0.62
MnSi-B20	6.5	2.39(1)	0.010(4)	5.9	2.788(6)	0.005	-	1.88
***t*-MnSi-B2**	8	2.370		6	2.790			
$\mathbf{Mn}_{Si}$	4	2.351						

Table 4.2: Coordination numbers N_i and distances R_i of the first ($i = 1$) and second ($i = 2$) shells obtained from the fit of the in-plane (ip) and out-of-plane (oop) XAFS data of the samples and the ip data of the 5 nm MnSi-B20 film. Estimated parameters of a tetragonally distorted MnSi-B2 structure (t-MnSi-B2) and of Mn in Si substitutional site (Mn_{Si}) are also included. $A_{\text{Mn-Mn}}$ is the area under the Mn-Mn profile function relative to that of Mn-Si. The percent residual (R %) and uncertainty of each fitting parameter (in parentheses) are also included.

Philips CM30 TEM. Energy dispersive x-ray spectroscopy (EDX) was also used to probe the chemical composition of the precipitates that formed in certain samples.

To analyze the magnetic properties of the samples, I measured their moment as a function of field ($m-H$) and remanent moment as a function of temperature ($m_r(T)$) with SQUID magnetometry. For all magnetic measurements 3-5 samples, each nominally 4 mm $\times$ 5 mm, were stacked and placed inside the sample holder. I did not find a difference in the hysteresis loops when measured with the field applied along the [100] or [110] directions, which is likely a result of the disorder in the Mn layer. The paramagnetic and diamagnetic responses of the low-resistivity Si(001), where the boron concentration is of the order of $10^{15} - 10^{16}$ atoms/cm^3, were subtracted from each $m - H$ curve as described in Chapter 2. Samples grown on the high-resistivity substrates did not show a paramagnetic contribution and only the diamagnetic response of the Si was subtracted. I calculated the Mn saturation moment μ_{Mn} from the $m - H$ loops measured at $T = 2$ K and estimated the T_C from the point where $m_r(T)$ drops to zero.

To further confirm that the magnetic signal of the δ-doped films arises from Mn, and to rule out contamination from the Pb source, I measured the magnetic response of a sample prepared without Mn and consisting of 2 ML Pb grown at $T = 25$ °C and capped by a 12.4 nm Si grown at 200 °C. The saturation and remanent moments of this Mn-free control sample were close to zero (within the detection limits of the SQUID magnetometer).

4.2 Structural and Magnetic Phase Diagram of Mn δ-doped Si Films

For the ranges of θ_{Mn} and T_{Si} considered, structural analysis and SQUID results demonstrate that the Mn δ-doped samples occupy three regions in the growth-phase-diagram, characterized by distinct magnetic ordering and local crystallographic structure. The three regions are labeled A-C and presented in Fig. 4.3.

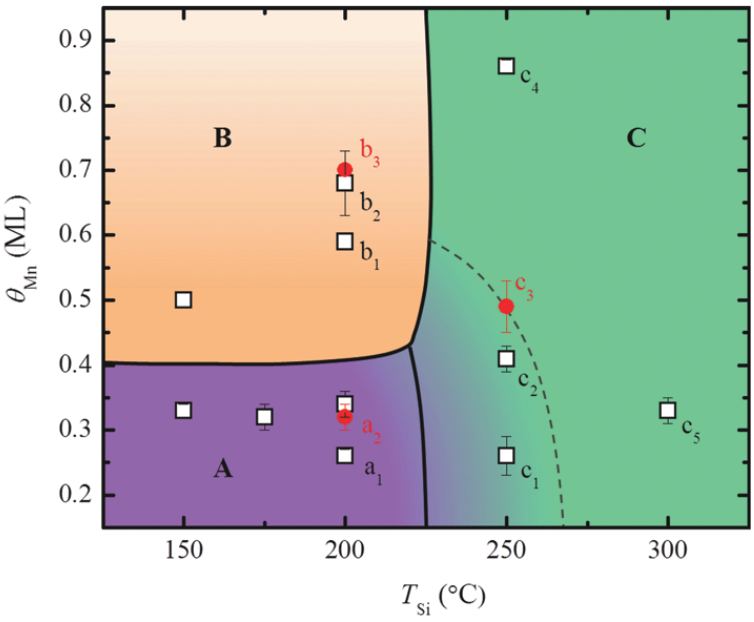

Figure 4.3: Three regions A-C are identified in the growth-phase-diagram based on the magnetic and structural properties of the samples. The samples are indicated according to the first column of Table 4.1 and the three control samples grown without Pb are shown in red circles. The dashed line bounds a mixed-phase in region-C.

Region-A has a T_C well above room temperature, as indicated by the non-zero remanent moment measured up to $T = 400$ K (Fig. 4.4(a)). The existence of magnetic order is confirmed by the presence of hysteresis as shown in Fig. 4.5 (a). Sample a_1 was found to have the optimal growth conditions that produced the largest m_r (Fig. 4.4 (a) and (d)) and the largest saturation moment, $\mu_{Mn} = 1.56\ \mu_B$ measured at $T = 2$ K (Fig. 4.5(d)). This sample has the lowest Mn concentration, $\theta_{\mathrm{Mn}} = 0.26$ ML, and a growth temperature that is closest to the phase boundary between regions A and C. The m_r decreases as T_{Si} drops from this optimal $T_{\mathrm{Si}} = 200$ °C (Fig. 4.4(d)), while the μ_{Mn} measured at $T = 2$ K drops quickly with increasing θ_{Mn} (Fig. 4.5(d)).

Fits to the XAFS spectra resolve the first two shells surrounding the Mn atoms that correspond to the Si nearest neighbors and Mn next-nearest neighbors. The Mn-Si bond length, $R_1 = 2.374$ Å and the coordination number $N_1 = 6.7 \pm 0.7$ are larger than expected for substitutional Mn (see Table 4.2). The large coordination indicates

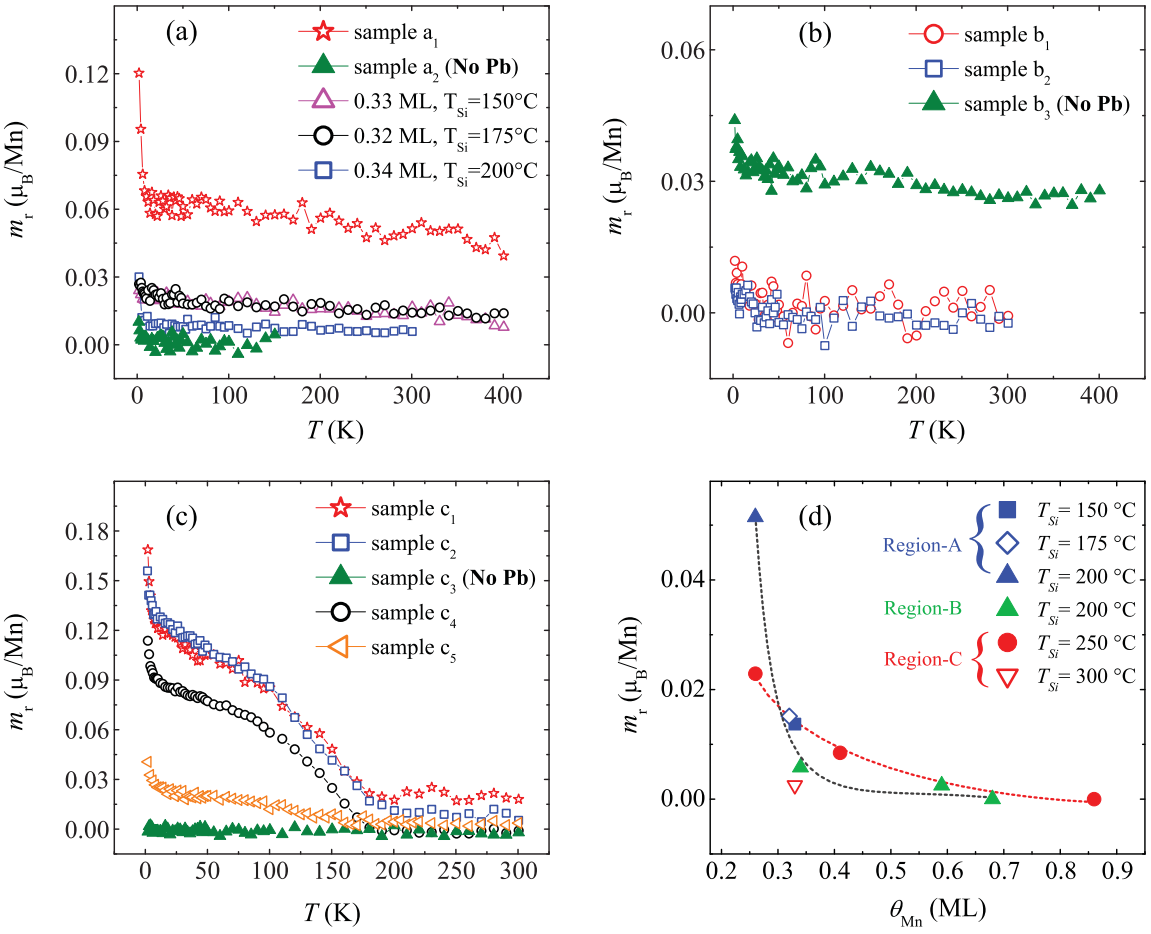

Figure 4.4: (a) Non-zero $m_r(T)$ indicate a ferromagnetic phase with $T_C > 400$ K for samples in region-A. The control sample of this region (filled triangles) has zero remanent moment. (b) $m_r(T)$ show no ferromagnetic ordering for samples grown with Pb in region B but a $T_C > 400$ K for the control sample. (c) A magnetic phase transition is observed in region-C with $T_C \simeq 170$ K for all samples with Pb. There is no remanent moment for the control sample of this region. (d) Remanent moment measured at $T = 250$ K as a function of θ_{Mn} for all T_{Si}. Dashed lines connect the samples grown with the same T_{Si}.

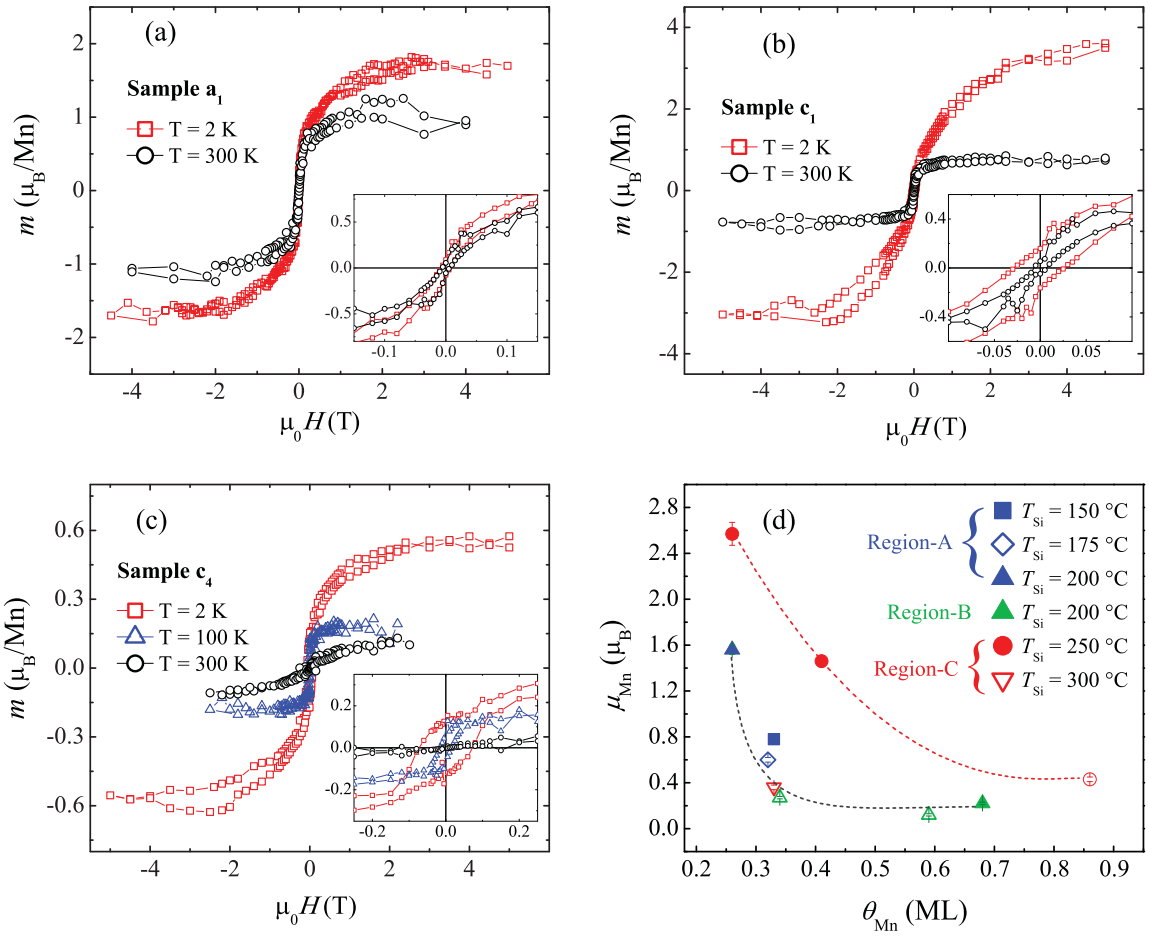

Figure 4.5: $m - H$ loops measured at low and high temperatures as indicated. The insets show that there is a hysteresis at $T = 300$ K for samples (a) a_1 and (b) c_1 but it vanishes for sample c_4 (c). (d) Variation of Mn saturation moment μ_{Mn} calculated at $T = 2$ K as a function of θ_{Mn}. Open symbols refer to samples grown on low resistivity Si(001) where the boron paramagnetic contribution has been subtracted and the dashed lines connect the samples with the same T_{Si}.

the formation of precipitates, although these phases could not be detected in the TEM experiments. A qualitative comparison between XAFS measurements of sample a_1 and calculated spectra shows that the local Mn environment does not correspond to either MnSi-B20, $MnSi_{1.7}$ or Mn_5Si_3 crystal structures that are commonly formed during the deposition of Mn on Si(001) [137, 75]. Furthermore, the Mn-Mn bond length $R_2 = 2.75$ Å is significantly contracted relative to that measured for $MnSi_{1.7}$ precipitates in Ref. [51].

According to DFT predictions, tetragonally distorted MnSi-B2 is the most energetically favorable structure that forms on Si(001), since MnSi-B2 phase has a reasonably good lattice match to Si(001) [55]. A MnSi-B2-like phase was observed in one of the samples studied in Chapter 3. A comparison between the fitting parameters in Table 4.2 with those expected for a B2 shows that this structure is the closest match to sample a_1 (see Fig. 4.2 (a)). The expected 8-fold coordinated crystal structure can be constructed from a Si lattice by placing Si and Mn into interstitial sites. Missing interstitials would account for some of the discrepancy between the measured and the expected coordination number for a B2 structure. RBS, however, shows that only 65% of the Mn in sample a_1 is in interstitial sites (Fig. 4.6), which indicates that Mn in this sample has at least two distinct environments. Although the XAFS is not inconsistent with the co-existence of both a B2 phase and Mn_{Si}, such a fit would introduce too many fitting parameters to permit a quantitative analysis.

The SQUID data is also suggestive of two components: Fig.4.5(a) reveals a wasp-waisted hysteresis loop that can be constructed from the superposition of a ferromagnetic and a superparamagnetic hysteresis loop, as shown in the case of $MnSi_{1.7}$ nanoparticles in Si [138]. The ferromagnetic hysteresis loop seen at low magnetic field in the inset of Fig. 4.5(a) has a weaker temperature dependence than the S-shaped portion of the $m-H$ curve visible at high fields, which suggests that these components have different magnetic behaviors.

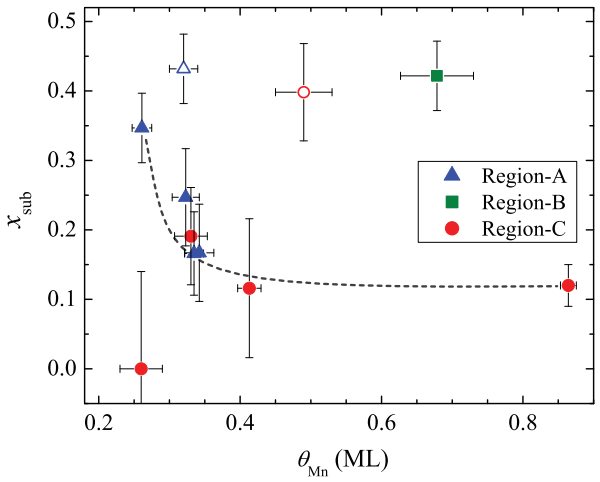

Figure 4.6: Variation of x_{sub} with Mn coverage θ_{Mn} for samples in all three regions of the growth diagram. Open triangle (circle) refers to control sample of region-A (region-C) grown without Pb and the dashed line is a guide to the eye.

The samples in Region B of the growth-phase-diagram have T_C's near zero (Fig. 4.4 (b)) and the μ_{Mn} values are small (Fig. 4.5 (d)). However, there is a noticeable change in the Mn environment when θ_{Mn} increases to 0.59 ML at $T_{\text{Si}} = 200$ °C. In particular, sample b_1 has a distinctive in-plane structure with two Mn-Si shells as opposed to Mn-Si and Mn-Mn shells for all other samples. Sample b_1 has a reduced coordination number $N_1 = 2 \pm 1$ and a short Mn-Si distance $R_1 = 2.22$ Å that form only in-plane. This result is similar to the split shell and reduced coordination observed in (Ga,Mn)As at the boundary between the DMS phase and the precipitate region of the growth-phase-diagram [139]. The TEM images of Fig. 4.7(a) show that sample b_2 contains precipitates with an estimated lateral size of up to 15 nm. Curiously, samples from this region still show a considerably large x_{sub} (Fig. 4.6). The small μ_{Mn} and low T_C indicate that these sites are not magnetically active.

In region-C of Fig. 4.3, the m_r has a concave shape typical of ferromagnetism that drops either to zero or to a small constant value at a temperature of 170 K. This transition temperature is unaffected by a variation in θ_{Mn} or an increase in T_{Si} to 300 °C (Fig. 4.4(c)), which reflects a higher stability relative to the phase in

region-A. It is likely that this magnetic behavior arises from the large precipitates that form in this region and can be seen in the cross-section TEM image of sample c_4 (Fig. 4.7(c)), given that the onset of this new low temperature feature coincides with their appearance. The nano-disk shaped precipitates (Fig. 4.7(d)) distribute themselves at the interface with a range of sizes that vary between 10-200 nm in diameter. It is important to note that, unlike a similar structure of Mn doped Ge where the Mn acts as a surfactant and floats to subsurface sites in the Ge cap [129], the measurements show that Mn in the δ-doped Si layers remains localized at the interface. For instance, it was not possible to detect Mn-rich inclusions in the Si cap from the cross-sectional TEM image of Fig. 4.7(c), but only the MnSi nano-disks were observed at the interface. Also, the depth of the backscattering Mn atoms measured by the RBS GAD detector was consistent with the thickness of the Si capping layer ($\sim$ 12.4 nm), which indicates that Mn is buried at the interface.

Energy-dispersive x-ray spectroscopy (EDX) showed that the precipitates contain Mn, but it was not possible to determine their phase from the weak reflections in the selected area diffraction pattern (SADP) measurements. While a fit to the XAFS data beyond $R = 3$ Å is not possible, a comparison between the XAFS function of sample c_4 and that of the MnSi-B20 phase shows similar features up to $R = 5$ Å(Fig. 4.2(b)), which suggests that the structure of the sample is more B20-like than the other possible phases. In particular, the $|FT[k^2\ \chi(k)]|$ show a common peak at $R \sim 4$ Å which is consistent with a single scattering from the second-nearest-neighbor Mn located at $R = 4.138$ Å, according to the calculated MnSi-B20 model. However, although the first Mn-Si shell coordination number and radius are within the error limits of those of MnSi-B20, the second shell shows deviations from this structure. The ip and oop bond lengths of the second shell appear to be expanded relative to the R_2 of a B20 structure (see Table 4.2). Furthermore, the magnetic transition at $T = 170$ K is not consistent with the $T_C \leq 44$ K of ordered MnSi-B20

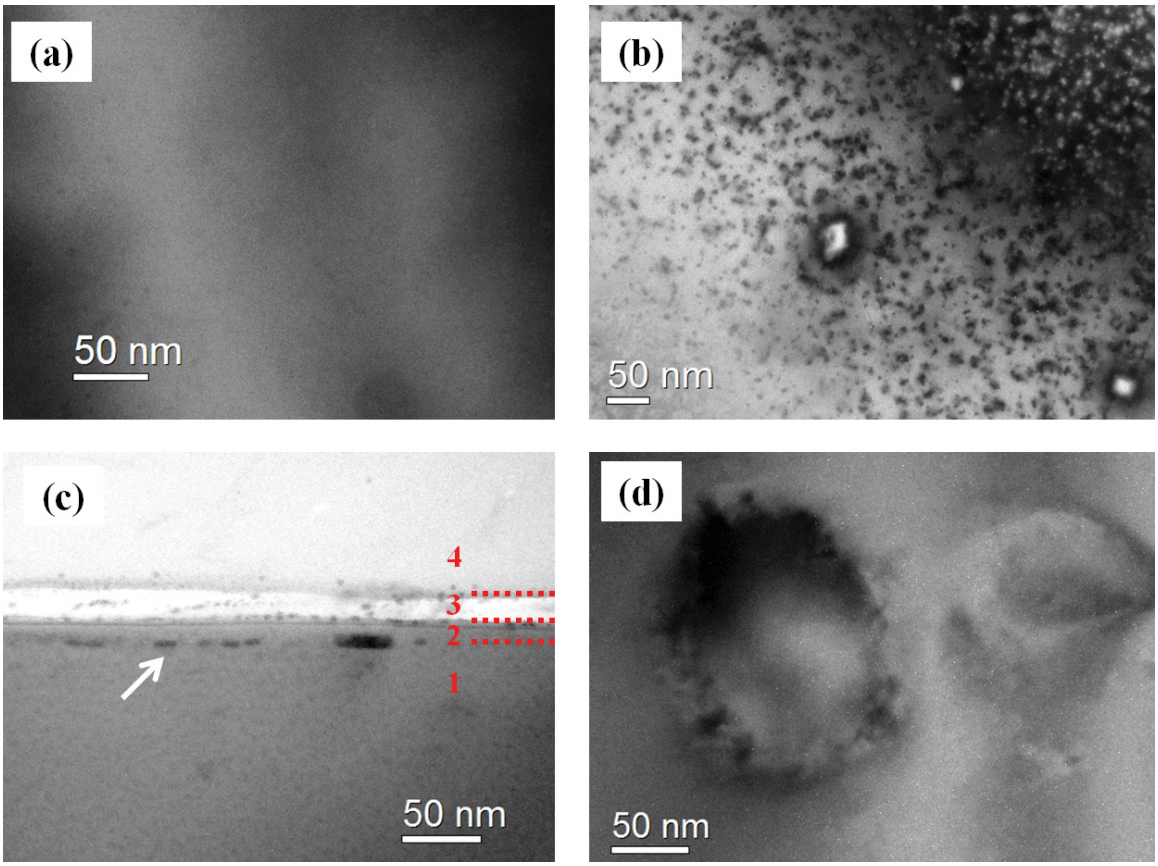

Figure 4.7: (a) The bright field plan-view TEM image of sample a_1 hardly shows any precipitates whereas (b) Mn-rich precipitates are clearly observed in sample b_2. (c) Cross-section TEM image of sample c_4 shows Mn-rich precipitates (dark features indicated by arrow) distributed at the interface between the substrate (1) and the Si-cap (2). The epoxy layer (3) that glues the samples to a second Si wafer (4) is also visible in the image. (d) Plan view TEM image of sample c_4 shows nano-disk shaped precipitates.

thin films [119]. I therefore speculate that the low θ_{Mn} and low T_{Si} create a defected MnSi-B20 structure. Such a structure has been observed in Chapter 3 and in Mn^{+} implanted Si(001) [68].

The presence of a second phase is evidenced by the non-zero m_r above 170 K in the lower θ_{Mn} samples in region-C. The m_r of sample c_1 above 170 K matches the temperature dependence of the remanent moment of region-A samples. Furthermore, the values of the high-temperature m_r for the region-C samples are comparable to those of region-A (see Fig. 4.4(d)) with the exception of the optimal sample a_1. This suggests that while the higher T_{Si} drives the Mn into larger precipitates with $T_C \simeq 170$ K, some of the Mn forms the same structure found in region-A. Like the phase in region-A, this second phase is sensitive to θ_{Mn}. Figure 4.4(c) shows that the high temperature m_r is zero for sample c_4 ($\theta_{\mathrm{Mn}} = 0.86$ ML), which suggests that the second phase is absent in this sample. It is also sensitive to growth temperature: $m_r(T) = 0$ above $T = 170$ K for the $T_{\mathrm{Si}} = 300$ °C sample in Fig. 4.4(c).

4.3 The Influence of the Pb Surfactant

The control samples grown without Pb demonstrate the dramatic influence of the Pb surfactant on the magnetic properties of the Mn δ-doped layers. Without Pb, the samples in regions-A and C have no long-range magnetic order, as shown by the zero remanent magnetization of these samples in Figs. 4.4(a) and (c), although the saturation magnetization for the control sample in region-A (sample a_2) is 0.78 μ_B. Surprisingly, the situation is reversed in region B. The sample without Pb has a local coordination that is within error of MnSi-B2 structure (sample b_3 in Table 4.2) and a large remanent moment (Fig. 4.4 (b)) with a $T_C > 400$ K. The formation of a MnSi-B2 structure explains this magnetic behavior, as discussed in Chapter 3. It is, however, worth pointing out that this B2 phase grown without Pb only forms at the higher coverages corresponding to region-B, and RBS indicates that the x_{sub} is close

to zero for this sample. Like the other samples, the x_{sub} measured by RBS is not a good indicator of the magnetic behavior of the control samples. The substitutional fraction of the control samples in regions-A and C shown in Fig. 4.6 is larger than the samples with a Pb surfactant. It is likely that x_{sub} originates from substitutional-like sites within the precipitates.

To understand how Pb can influence the formation of $\mathrm{Mn_{Si}}$, DFT calculations were performed. It is found that Pb increases the formation energy of $\mathrm{Mn_{Si}}$ by direct substitution into a surface Si site. However, the Pb surfactant tends to weaken the top layer bonding of Si and DFT calculations show that this enhances vacancy formation in the top Si layers, and thereby creates a channel for the Mn to incorporate substitutionally.

DFT calculations were carried out using the VASP code within the generalized gradient approximation [140, 141] and with the Projected Augmented Wave PBE potential as the pseudo potential [142, 143]. Various theoretical and experimental studies show that different amounts of Pb on Si can form different surface reconstructions [144, 145, 146]. For one full monolayer coverage of Pb, a 2×1 surface reconstruction was chosen as both confirmed by the *in situ* RHEED observations and by scanning tunneling microscopy measurements and calculations [144, 145, 146]. The simulation cell consisted of a 144 Si atoms slab with 32 H atoms passivating the dangling bonds of the bottom surface, as shown in Fig. 4.8(a). One full layer of Pb atoms was introduced into the calculation as the surfactant and the thickness of the vacuum layer was about 18 Å. The plane wave cutoff energy was 245 eV and a $2 \times 2 \times 1$ k-point mesh was used for Brillouin zone sampling. A total energy minimization was performed by relaxing atomic positions until the forces converged to less than 0.01 eV/Å. The calculated Si lattice constant was 5.469 Å, which is in good agreement with the experimental value of 5.43 Å.

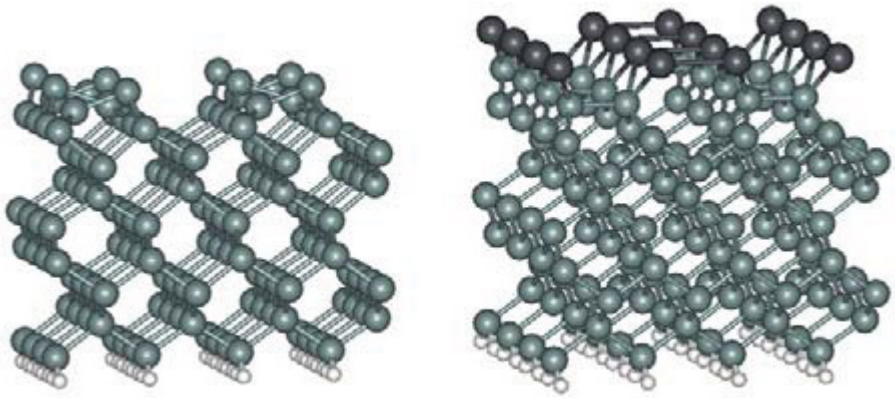

Figure 4.8: (a) Schematic illustration of the DFT simulation supercell. Grey spheres are Si atoms and small white spheres at the bottom represent H atoms. (b) Schematic illustration of the surface reconstruction of one monolayer of Pb (black spheres at the top) on Si thin film.

The formation energy of a vacancy is defined as:

$$E(formation) = E(vac) - E(reference) + \mu(Si) \tag{4.2}$$

where *E(reference)* is the total energy of the Si slab, *E(vac)* is the total energy of the same cell with one Si atom removed and $\mu(Si)$ is the chemical potential of the Si, which is the energy per atom of a bulk calculation of a system with 512 Si atoms. The chemical potential of the Si was calculated to be -5.43 eV. The formation energy of an atom vacancy on the surface layer in a pure Si thin film was calculated by removing a Si atom from the top dimer layer of the 2×1 reconstructed surface. An $E(formation) = 1.18$ eV was found in this case. When a Pb surfactant layer was added to the surface (Fig. 4.8 (b)), the formation energy corresponding to the removal of one Si atom dropped to 0.26 eV, which is about 0.92 eV lower than the vacancy formation energy for a pure Si surface at the same site. The Pb atoms largely disturb the top Si surface layer and lower the Si vacancy formation energy. On the other hand, the interstitial diffusion is unlikely to change much due to the surfactant.

4.4 Discussion

The contrasting magnetic behavior of the samples in the three regions of the growth-phase-diagram raises the question of the mechanism behind the magnetic order. For regions-A and C, the m_r and the μ_{Mn} are found to decrease with increasing θ_{Mn}, as shown in Figs. 4.4 (d) and 4.5 (d). This is likely a consequence of the fact that as the concentration of Mn increases, so does the probability of the formation of precipitates. It is interesting that x_{sub} also drops with increasing θ_{Mn} in regions-A and C (Fig. 4.6), possibly for the same reason. It is important to understand the role that the Si matrix must play in mediating the ferromagnetic order. One possible mechanism is the formation of a $\mathrm{Si}_{1-x}\mathrm{Mn}_x$ dilute magnetic semiconductor (DMS) in the regions between the precipitates. RBS measurements show that the remanent magnetization is possibly correlated with the fraction of substitutional Mn, x_{sub}. In Fig. 4.9, the m_r increases approximately linearly with x_{sub} for samples in regions-A and C. The sample that lies off this trend is sample c_1 for which $x_{\mathrm{sub}} = 0$, although this value is only 1.5 standard deviations from the line of best fit. Furthermore, flux peaking may result in an underestimation of this value. Since MnSi-B2 samples are known to be ferromagnetic with a high T_C [55, 147], a $\mathrm{Si}_{1-x}\mathrm{Mn}_x$ DMS provides a plausible explanation for how the precipitates in region-A are correlated in order to yield a high T_C. A similar mechanism of DMS mediated interaction explains the coupling between the $\mathrm{Mn}_x\mathrm{Ge}_{1-x}$ nanocolumns in Ref. [148], and was shown to compete with an antiferromagnetic dipolar coupling between the nanocolumns.

A difficulty with the interpretation of the RBS data is that one cannot distinguish the substitutional-like Mn in the precipitates from the $\mathrm{Mn}_{\mathrm{Si}}$. While Fig. 4.9 shows a possible correlation between m_r and x_{sub}, there is no correlation between μ_{Mn} and x_{sub} that would allow the extraction of the magnetic moments of the individual magnetic phases in the composite samples. However, an assumption can be made for

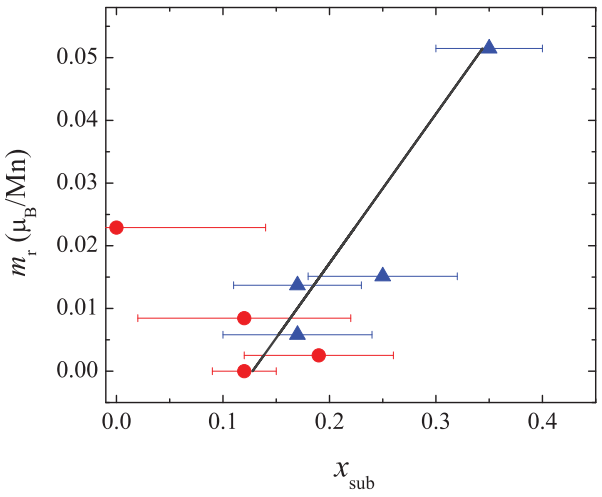

Figure 4.9: Variation of the remanent moment measured at $T = 250$ K with the fraction of substitutional Mn, x_{sub}. A possible correlation exists for samples of region-A (blue triangles) and region-C (red circles), as shown by the line of best fit.

sample a_1, which shows strong evidence of two magnetic phases, as noted above. For this sample, if all Mn are magnetically active, the saturation moment at $T = 2$ K, $\mu_{Mn} = 1.56\ \mu_B$, can be decomposed into two components using the values of x_{sub}: $\mu_{Mn} = 0.35(\pm 0.05)\ \mu_{sub} + 0.65(\pm 0.05)\ \mu_{B2}$, where μ_{sub} is the magnetic moment of the substitutional phase and μ_{B2} is that of the MnSi-B2-like precipitates. From the DFT predicted value $\mu_{sub} = 3\ \mu_B$ [44], one finds $\mu_{B2} = 0.8(\pm 0.2)\ \mu_B$. This value of μ_{B2} is in good agreement with that estimated for a tetragonally distorted MnSi-B2 with a lattice constant between $2.74 - 2.79$ Å (see Fig. 4 in Ref. [55]). The lattice constant of sample a_1 is ~ 2.76 Å(Table 4.2). Note that Ref. [55] shows that the value of μ_{B2} depends on the volume of the unit cell.

Surprisingly, the region-B samples were found to have the highest x_{sub} (Fig. 4.6(b)). The absence of ferromagnetism in the region-B samples could be due to a number of possibilities. One possibility is the presence of an antiferromagnetic component. DFT calculations of Mn interstitial-substitutional complexes, however, predict ferromagnetic behavior [149]. More recent calculations of δ-doped layers of mixed substitutional and interstitial Mn finds a complex non-collinear magnetic order [53]. A

second possibility is that the measured $x_{\rm sub}$ of the samples of region-B arises mostly from the precipitates and a lack of $\rm Mn_{Si}$ prevents magnetic order other than at very low temperature.

In region-C, however, the MnSi-B20 type precipitates were not expected to have a T_C as large as 170 K due to the small $T_C \leq 44$ K found in MnSi thin films [150]. It is possible that the model put forward in Ref. [38] to explain the high T_C in nanocrystalline $\rm MnSi_{1.7}$ precipitates in Si also explains the behavior of the region-C samples. Like $\rm MnSi_{1.7}$, MnSi-B20 is a weak itinerant magnet where the $3d$ states are delocalized due to the strong $sp-d$ hybridization between Mn and Si. However, the structural disorder suggested by the XAFS data may lead to the localization of the wave function of the $3d$ carriers about the Mn defects within the precipitates. The localization length depends on the nature of localization and the impurity concentration within the precipitates. In the case of $\rm MnSi_{1.7}$, it is estimated that a Mn impurity concentration of 8% in the precipitates is enough to increase their moment from 0.01 μ_B to 0.2 μ_B [38]. Given the Mn concentration of the δ-doped layers of region-C samples, $\sim 10^{22}$ $\rm cm^{-3}$, and the metallic character of the bulk MnSi-B20 phase, it is expected that the precipitates are also metallic. The large magnetic moment measured for these samples may therefore be explained by the Anderson mechanism of local moment formation of a magnetic impurity in a metallic host [151]. According to the Anderson model, the formation of a local magnetic moment is dependent on the Coulomb interaction U between the $3d$ electrons of the impurity ion, the level of mixing between the d and s orbitals and the energy difference between the d levels and the Fermi level of the system. The impurity ion will be magnetic when $U\eta_d(\epsilon_F) > 1$, where $\eta_d(\epsilon_F)$ is the density of d-states at the Fermi level. For Mn in disordered MnSi-B20, it is not exactly clear whether a high $\eta_d(\epsilon_F)$ or a high U is responsible for the large moment formation. The first principles calculations of Ref. [152] demonstrate that U plays a major role in moment formation in $\rm Fe_xSi_{1-x}$: a $U = 3.0$ eV causes the magnetic

moment of Fe in $Fe_{0.0625}Si_{0.9375}$ to increase from 0 to 3.02 μ_B.

Men'shov et al. [38] proposed that the large localized magnetic moments are coupled by spin-fluctuations in the itinerant $MnSi_{1.7}$. If such a mechanism exists in the MnSi-B20 nano-disks, this may explain the large T_C of these precipitates. However, given the size of the nano-disks, superparamagnetic behavior would be expected. In this case, a relationship between the blocking temperature T_B and the magnetic anisotropy energy density K_a of the MnSi-B20 nanoclusters can be established from the Néel-Brown theory of superparamagnetism [153]:

$$T_B = \frac{K_a V}{k_B \ln(\frac{\tau_m}{\tau_0})} \ , \tag{4.3}$$

where V is the volume of the nanoclusters and τ_m and τ_0 are the measurement and attempt times, respectively. By considering the typical values of SQUID measurement time (10^2 second) and τ_0 (10^{-10} second), and an average nano-disks volume of 4×10^3 nm^3 estimated from the TEM measurements, one finds that $K_a \sim 95\ T_B$ (J/K m^3). If T_B is considered to be the same as the transition temperature $T = 170$ K measured for region-C samples, a value of $K_a \sim 16$ kJ/m^3 is obtained. This value falls within the range of the uniaxial magnetocrystalline anisotropy calculated for various thicknesses of MnSi-B20 films on Si(111) [150].

Moreover, a DMS may be the second phase that is mediating a ferromagnetic interaction between these large moment precipitates, although this coupling is minimal since the second phase disappears in the 0.86 ML sample whereas the $T_C = 170$ K remains the same. The large T_C of the precipitates could also be related to the interfacial Mn, which is shown theoretically and experimentally to have an enhanced magnetic moment [55, 119].

In summary, similar to the findings of Chapter 3, the study of this chapter also

showed that the growth conditions of the Si capping layer are a key factor in determining the structure and magnetism of the δ-doped films. As with the previous chapter, a disordered MnSi-B2-like structure forms at lower Mn concentrations. RBS shows that these precipitates coexist with a large fraction of Mn_{Si} that forms due to Pb promoted vacancy formation in the capping layer. It is speculated that a $Si_{1-x}Mn_x$ DMS that forms in the Si matrix mediates a long-range exchange coupling between the precipitates. However, the nature of the ferromagnetic coupling in the δ-doped samples is blurred by the inhomogeneities of the structures. In region-C, the B20-like precipitates that form are likely metallic and their large magnetic moments may be explained by the Anderson model, which are then coupled by spin fluctuations.

Chapter 5

Influence of Pb Surfactant on the Magnetism of Dilute $Si_{1-x}Mn_x$ Films

The sensitivity of dilute magnetic semiconductors to growth conditions and to modulation in the concentration of transition metals often leads to the development of secondary phases. The growth of DMS commonly produces transition metal-rich nanocrystallites with various shapes and alloy compositions [37, 35, 154, 148, 155]. However, there are relatively few studies on the growth and magnetic properties of these precipitates. These nanocrystallites created under the appropriate growth conditions provide new opportunities for creating semiconductor compatible magnetic materials [156, 157].

It is generally understood that the precipitates result from a spinodal decomposition of the DMS at intermediate growth temperatures [156, 69, 35, 158]. Monte Carlo simulations show that the morphology of the precipitates is influenced by the growth mode, where a 2D growth mode leads to the formation of nanocolumns [159] while a 3D mode leads to more isotropic shapes. The charge state of the transition metal also plays an important role. For instance, by changing the carrier densities and the charge state of the Cr impurities by co-doping with either n-type or p-type dopants, the degree of Cr clustering in $Zn_{1-x}Cr_xTe$ can be tuned [11].

Nanocolumns were reported in several systems including (Al,Cr)N [160], (Zn,Cr)Te [161], (Ge,Mn) [35] and during the MBE growth of $Si_{1-x}Mn_x$ thin films [69]. In the case of (Ge,Mn), the nanocolumns that form with a composition close to the uncommon Ge_2Mn phase display a giant magnetoresistance of up to 7000% at 30 K and

a $T_C > 400$ K [35]. The origin of the magnetic order in the nanocolumns has been suggested to be due to the confinement of the carriers inside the Ge matrix [162]. Above room temperature ferromagnetism is also found in incoherent nanocrystals, such as MnAs in GaAs [155] and $MnSi_{1.7}$ in Si [36, 33, 37].

The interesting results reported for (Ge,Mn) nanocolumns and the lack of a magnetic characterization of their (Si,Mn) counterparts, motivated the study presented in this chapter. Given the success of the Pb surfactant in previous studies, it was important to know whether Pb could also stabilize a high T_C phase in $Si_{1-x}Mn_x$ alloys. Furthermore, since Pb is known to increase the diffusion length of Si during homoepitaxy, it is interesting to investigate its influence on the growth of nanocolumns.

In contrast to the (Ge,Mn) case, I show that the nanocolumns that form in the Pb-free (Si,Mn) samples are paramagnetic with a small saturation moment that drops with increasing Mn concentration. On the other hand, I find that Pb does not support a spinodal decomposition of the $Si_{1-x}Mn_x$ into nanocolumns. The samples grown with 2 monolayers of Pb contain $MnSi_{1.7}$ nanorods that lie in the plane of the films. Although the saturation moment of these samples also drops rapidly with increasing Mn concentration, it is as high as 0.65 μ_B. At the lowest Mn concentration $x = 0.5\%$, the samples grown with a Pb surfactant exhibit two ferromagnetic transitions at the Curie temperatures $T_{C1} \approx 40$ K and $T_{C2} > 400$ K. While the transition at T_{C1} is consistent with the Curie temperature of bulk $MnSi_{1.7}$ crystals, T_{C2} is possibly due to a second phase resulting from Mn in the Si matrix.

5.1 MBE Growth of $Si_{1-x}Mn_x$ Films

For this study, I prepared two sets of samples. In the first set, denoted (Si,Mn), 50 nm thick $Si_{1-x}Mn_x$ layers were grown by co-depositing Mn and Si directly after the growth of a 100 nm Si buffer onto the Si(001) surface, while for the second set, Pb-(Si,Mn), 2 ML of Pb were deposited onto the Si buffer at $T = 25$ °C prior to

the co-deposition. For each set of samples, I investigated three Mn atomic fractions, $x = 0.005$, 0.015 and 0.030, and three growth temperatures $T_g = 150$ °C, 200 °C and 250 °C. During the growth, I rotated the sample to ensure uniform coverage and continually monitored the evolution of the surface structure by RHEED. The films were capped by a 10 nm Si layer, grown at the same conditions as the alloy layer. The Si evaporation rate was nominally set to 0.6 nm/min, whereas the Mn flux rate varied between 0.002 to 0.02 nm/min, depending on the Mn concentration.

The structure of the thin films was characterized with plan-view and cross-sectional TEM, whereas a SQUID magnetometer measured their magnetic properties. Samples preparation and procedures for TEM and SQUID measurements were similar to those described in Chapters 3 and 4.

5.2 Structure and Magnetism of the $Si_{1-x}Mn_x$ Thin Films

The RHEED patterns collected at the end of the growth did not show significant differences between the samples grown with and without Pb. For $x = 0.005$, the RHEED images of the $T_g = 150$ °C and 200 °C samples showed an array of diffuse diffraction spots (Fig. 5.1(b) and (c)), characteristic of a rough surface. However, an increase in temperature to $T_g = 250$ °C resulted in a significant improvement in the surface roughness of both the Pb-(Si,Mn) and (Si,Mn) samples: the RHEED diffraction spots were arranged on a Laue circle and the (2×1) reconstruction was still visible after the deposition of the 50 nm-thick $Si_{1-x}Mn_x$ film (Fig. 5.1(d)). For $x \geq 0.015$, all RHEED patterns showed a rough surface (similar to the patterns of Fig. 5.1 (b) and (c)).

Despite the similarities between the RHEED patterns for the Pb and Pb-free samples, TEM shows significant differences in their microstructure. All (Si,Mn) samples yield nanocolumns oriented along the growth direction, as expected from Ref. [69],

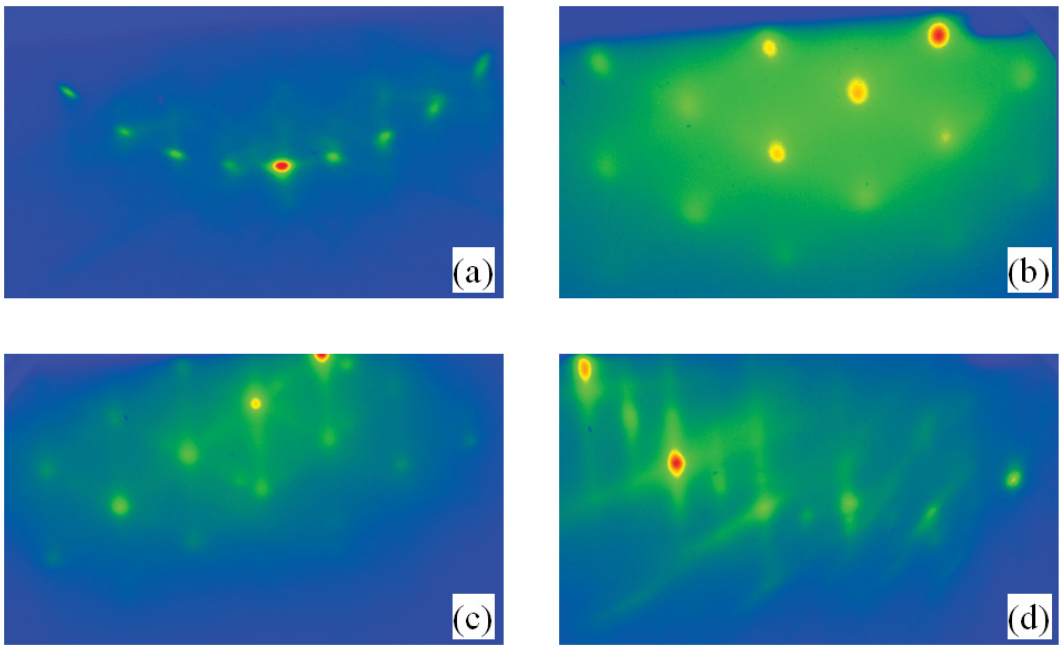

Figure 5.1: RHEED patterns of the Pb-(Si,Mn) samples with Mn concentration $x = 0.005$. (a) (2×1) surface reconstruction of the Pb covered Si(001) surface prior to the co-deposition of $Si_{1-x}Mn_x$ thin films. RHEED patterns at (b) $T_g = 150$ °C, (c) $T_g = 200$ °C and (d) $T_g = 250$ °C. Similar patterns were observed for the (Si,Mn) samples.

whereas the Pb-(Si,Mn) samples display nanocrystalline precipitates. The TEM images of the $T_g = 250$ °C samples in Figs. 5.2 and 5.3 illustrate these differences. The two representative [001] zone axis bright-field plan-view images of the (Si,Mn) samples in Figs. 5.2 (a) and (c) show a monodisperse distribution of circular dark spots. By tilting the sample away from the [001] zone axis, these spots elongate into lines (inset of Fig. 5.2 (c)), indicative of the nanocolumns, which are clearly shown in the cross-sectional TEM image of Fig. 5.4(b).

Other features are also visible in the TEM images of the (Si,Mn) samples. Stacking fault defects are observed at the two lowest growth temperatures, consistent with Ref. [69]. These stacking faults largely disappear by $T_g = 250$ °C. As the Mn concentration increases to 3%, irregularly shaped precipitates form together with the nanocolumns. Evidence of these precipitates appears in the selected area diffraction

patterns (SADP) as well. Although only very weak $MnSi_{1.7}$ diffraction spots appear at the [001] zone axis orientation, the SADP tilted about 17° off this axis (inset of Fig.5.2(b)) shows a hexagonal array of diffraction spots between the Si spots that correspond to (113), (220) and (104) reflections of Mn_4Si_7. No other (Si,Mn) sample displayed secondary crystalline phases in the SADP tilt-studies. The 0.5% sample grown at $T_g = 250$ °C only shows the diffraction spots from the Si lattice (Fig. 5.2 (d))

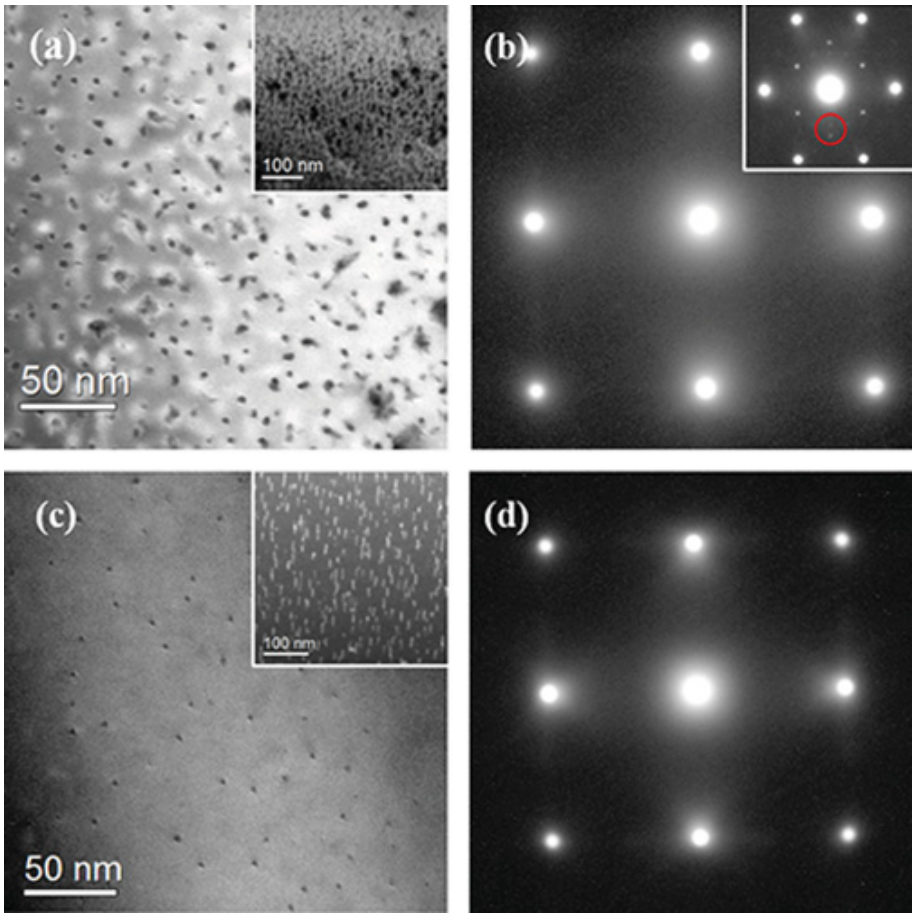

Figure 5.2: Plan-view TEM images of the (Si,Mn) samples grown at $T_g = 250$ °C with $x = 0.03$ ((a) and (b)), and $x = 0.005$ ((c) and (d)). The plan-view images in (a) and (c) show dark circular spots. By rotation away from the [001] zone axis, the plan-view images show that these are nanocolumns (insets (a) and (c)). The SADP taken at the [001] zone axis in (b) and (d) show only Si diffraction spots. Extra diffraction spots were only observed when the $x = 0.03$ sample was tilted off the [001] zone axis. The inner array of spots in the inset of (b) correspond to the (113), (220) and (104) (red circle) reflections of Mn_4Si_7 phase, and the outer spots are reflections from Si.

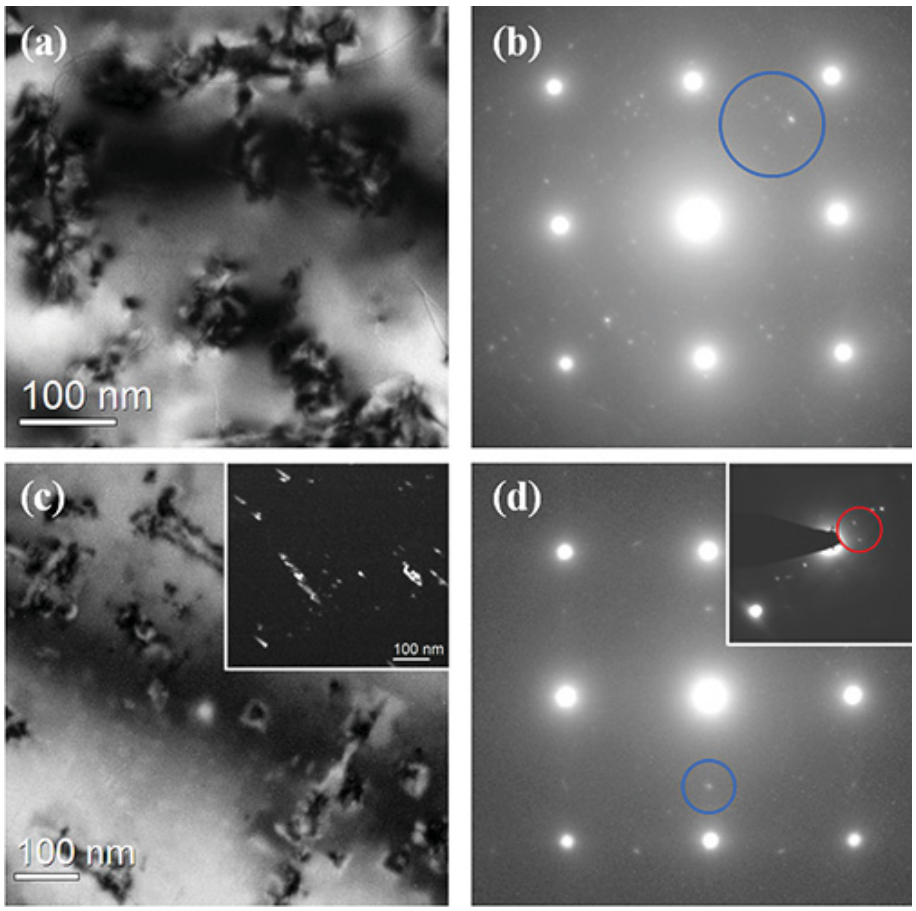

Figure 5.3: Plan-view TEM images of the Pb-(Si,Mn) samples grown at T_g = 250 °C with $x = 0.03$ ((a) and (b)), and $x = 0.005$ ((c) and (d)). Irregularly shaped precipitates form in (a) and are attributed to the $MnSi_{1.7}$ phase as confirmed from the extra diffraction spots shown inside the (blue) circle in (b) and corresponding to the (220), (214), (200) and (110) reflections of Mn_4Si_7. The elongated features in the image in (c) correspond to nanorods that form in-plane with a length that varies between $25 - 200$ nm and a diameter range of $10 - 30$ nm. The bright square features in (c) and the extra spot (blue circle) that appears in the SADP in (d) are due to stacking faults. The inset of (c) is a dark-field image of the $MnSi_{1.7}$ obtained from the diffraction spots shown inside the (red) circle in the inset of (d).

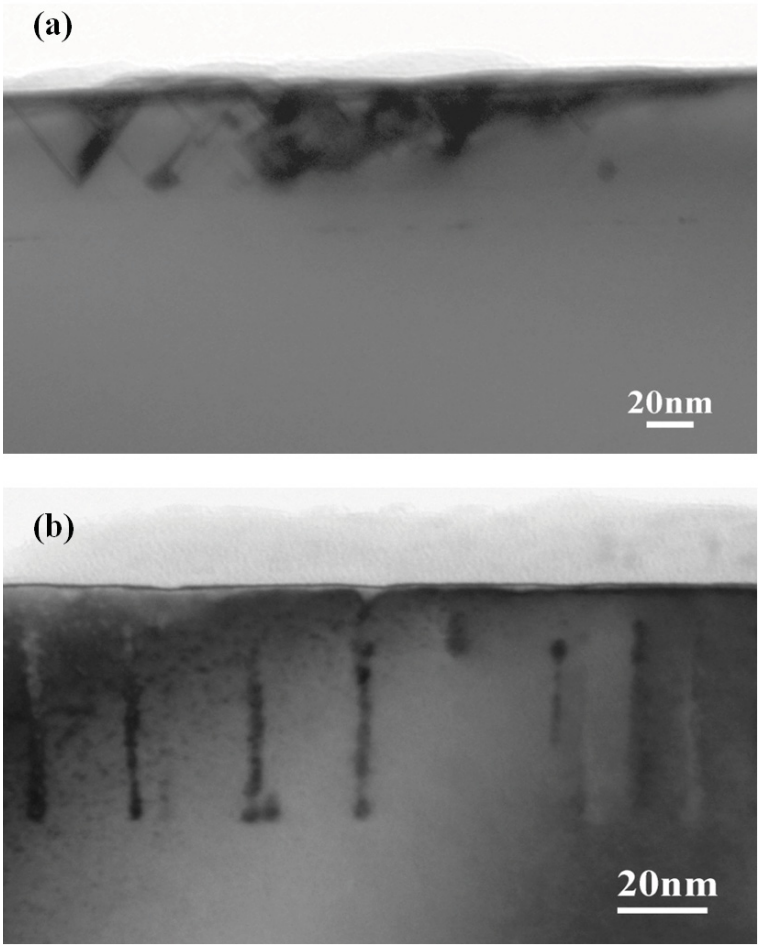

Figure 5.4: Cross-sectional TEM images of samples grown at T_g = 250 °C with $x = 0.005$. (a) Stacking faults are observed as inverted pyramids in the Pb-(Si,Mn) sample while in the (Si,Mn) sample (b) nanocolumns are formed and appear to extend from the interface up to the Si capping layer with an average length of 50 nm. The diameters of the nanocolumns vary between $2 - 5$ nm.

and increased thermal diffuse scattering that could be due to Mn in the nanocolumns. The T_g = 150 °C series of samples also display a faint ring in their SADP, although this is likely due to the formation of Si nanocrystallites in the film.

In contrast to the (Si,Mn) samples, the Pb-(Si,Mn) samples show a collection of crystalline precipitates. The elongated features in the bright-field plan-view image in Fig. 5.3 (c) correspond to nanorod-shaped precipitates that run along the ⟨110⟩ directions. Dark-field plan-view images taken at the $MnSi_{1.7}$ diffraction spots circled in

the SADP in the inset of Fig. 5.3 (d) show that the nanorods correspond to crystalline $MnSi_{1.7}$. The rods oriented in the orthogonal direction are absent from the dark-field image since their crystallographic orientations are orthogonal to the ones selected by the aperture. These are found along the same directions as the wires that form in submonolayer coverages of Mn on Si(001) [71, 72, 73], and nucleate at vacancies on the Si(001) surface [74]. These results are interesting in light of the DFT calculations of Chapter 4, which showed that a Pb surfactant lowers the vacancy formation energy. These vacancies may nucleate the nanorods and are possibly the origin of the different morphologies between the Pb-(Si,Mn) and (Si,Mn) samples. In addition to the nanorods, triangular precipitates are also found (not shown). The $MnSi_{1.7}$ precipitates are also present in the higher concentration samples, but with a higher degree of polycrystallinity as shown in Fig. 5.3(b), where the diffraction spots inside the blue circle correspond to (220), (214), (200) and (110) reflections of Mn_4Si_7.

The square features in the bright field image in 5.3(c) correspond to stacking faults, which are more clearly seen in the cross-sectional bright field image in Fig. 5.4(a). The plan-view and cross-sectional images show that these stacking faults form inverted pyramids, which are referred to as funnel defects in Ref. [69]. At $T_g = 150$ °C, the stacking fault density is high enough that additional spots appear in the [001] zone axis SADP between the Si(400) and the Si(000) spots. The spots can be properly identified in the SADP by rotation away from the [001] zone axis, which causes each spot to split into four due to the four [111] stacking planes.

Despite the similarity between the (Si,Mn) nanocolumns and those observed in other systems [35, 160, 161], the nanocolumns are found to be paramagnetic down to a temperature of at least 2 K. As in the previous studies, I measured the remanent moment, m_r, after saturating the samples in a 5 T magnetic field at a temperature $T = 2$ K then measured $m_r(T)$ on warming the sample up to 400 K. The open symbols in Fig. 5.5 show that the remanent moment is zero for all (Si,Mn) samples, with the

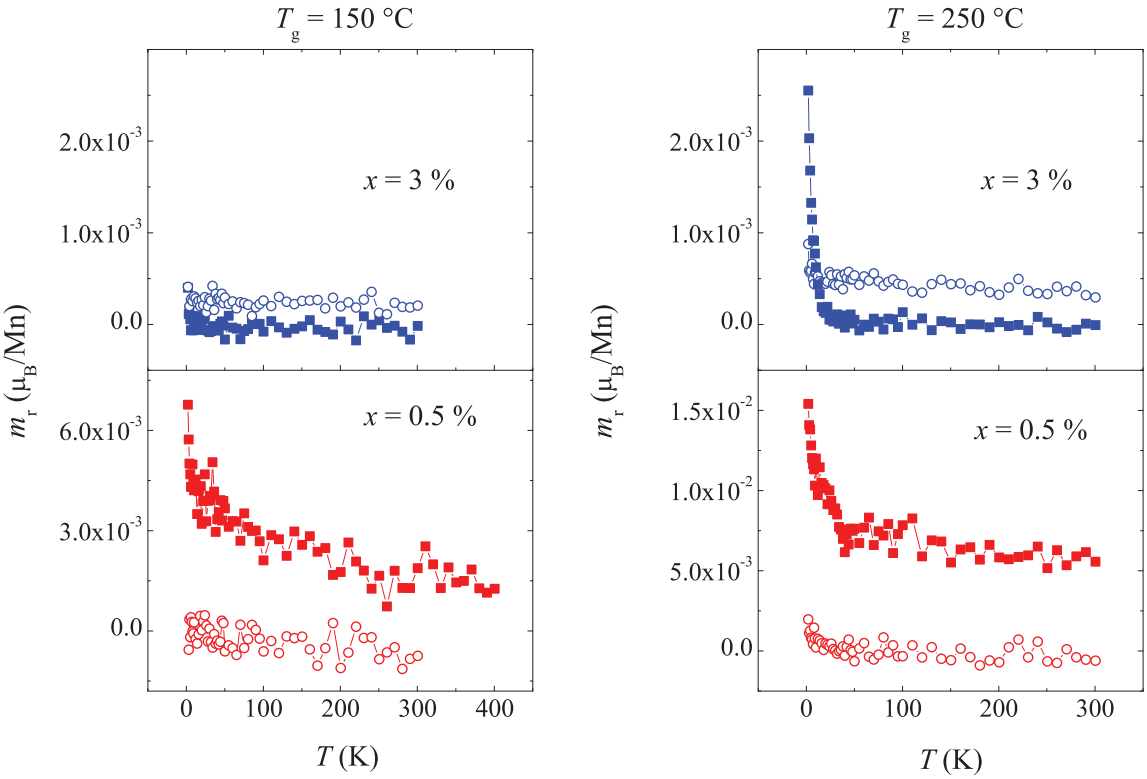

Figure 5.5: Variation of the remanent moment with temperature for Pb-(Si,Mn) samples (filled squares) and (Si,Mn) samples (open circles) grown at $T_g = 150$ °C (left) and $T_g = 250$ °C (right).

exception of the $x = 3\%$ sample grown at $T = 250$ °C. While the m_r of the $x = 3\%$ sample is small, it is important to note that the average of m_r above $T = 100$ K in this sample corresponds to $(2.7 \pm 0.4) \times 10^{-8}$ emu, which is more than six times the background level measured from the control samples (same as the control samples measured in Chapter 4), shown in Fig. 5.6. Furthermore, this is the only (Si,Mn) sample that contains $MnSi_{1.7}$ precipitates, and therefore this small magnetic signal is likely related to their presence, as discussed below.

The saturation moment, m_{sat}, obtained for (Si,Mn) is no larger than 0.28 μ_B/Mn at $x = 0.5\%$, and drops with increasing Mn concentration (Fig. 5.7). This is similar to what was found in amorphous a-(Si,Mn) alloys [163], where the loss of magnetic

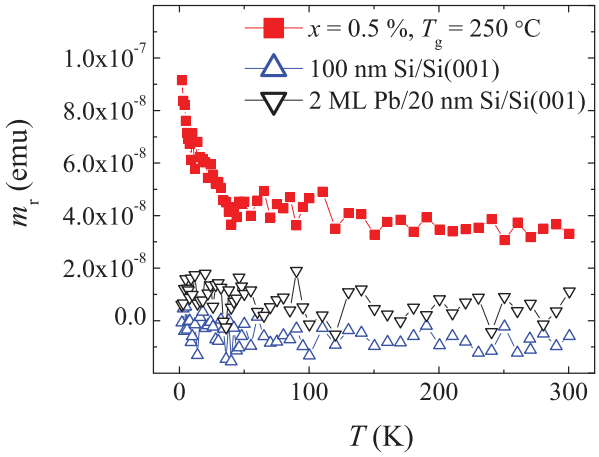

Figure 5.6: Total remanent magnetic moment as a function of temperature of the two Mn-free control samples and the $x = 0.5\%, T_g = 250$ °C Pb-(Si,Mn) sample. The average value of the moment above $T = 100$ K of the control sample with Pb ($(4 \pm 5) \times 10^{-9}$ emu) determines the background level of all $m_r(T)$ measurements.

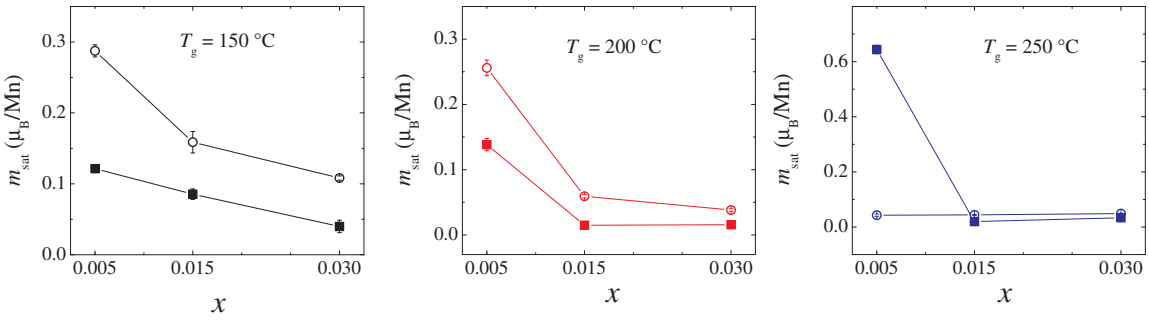

Figure 5.7: Variation of the saturation moment with Mn atomic fraction, x, measured at $T = 2$ K. Filled squares correspond to Pb-(Si,Mn) samples and open circles correspond to (Si,Mn) samples.

moment was attributed to the formation of an itinerant state produced by an Anderson localized impurity band. Given that the SADP from the (Si,Mn) nanocolumns do not display a secondary crystalline phase, it is likely that the nanocolumns are amorphous. In (Ge,Mn), the amorphous cores of the nanocolumns were speculated to be magnetically inactive [164]. It was recently shown that m_{sat} of both a-(Si,Mn) and a-(Ge,Mn) films drop with increasing Mn coordination number. However, Mn in a-(Ge,Mn) tends to form much lower coordinated structures than in a-(Si,Mn), and therefore develops a much larger moment in a Ge environment [165]. This result therefore explains the difference between the magnetic properties of the (Si,Mn) and (Ge,Mn) nanorods.

In contrast to (Si,Mn), the Pb-(Si,Mn) samples display ferromagnetic order. The $m_r(T)$ of Pb-(Si,Mn) samples with $x = 0.5\%$ in Fig. 5.5 (filled-squares) indicate two magnetic transitions. The $T_g = 250$ °C samples show a sudden upturn in $m_r(T)$ as the temperature drops below $T_{C1} \approx 40$ K that is suggestive of a phase transition. A similar feature is shown in the $T_g = 150$ °C samples, although the transition is more gradual. The transition at T_{C1} is possibly a consequence of the $MnSi_{1.7}$ precipitates and it is consistent with the values reported elsewhere [34, 39]. The persistence of a remanent magnetization in the $x = 0.5\%$ samples indicates a second magnetic transition $T_{C2} > 400$ K. Figure 5.5 shows that as the concentration increases, this high temperature phase disappears. However, the transition temperature attributed to the $MnSi_{1.7}$ phase is still observed in the $m_r(T)$ data of the $x = 3\%$, $T_g = 250$ °C Pb-(Si,Mn) sample, although T_{C1} drops to ≈ 25 K, possibly due to an absence of coupling between the precipitates without the presence of a second phase.

This second phase is possibly a DMS due to Mn dissolved in the Si matrix. The DFT calculations reported in Chapter 4 show that Pb makes the substitutional Si site accessible to Mn by increasing the density of Si vacancies in the film. The

largest m_{sat} values shown in Fig. 5.7 are significantly larger than what has been reported for bulk $MnSi_{1.7}$ crystals ($m_{sat} \approx 0.012\ \mu_B$/Mn) [39], or ion-implanted samples ($m_{sat} \approx 0.21\ \mu_B$/Mn) [37], which suggests that the second phase has a much larger moment. Substitutional Mn in Si is predicted to have a moment of nearly 3 μ_B [44]. A comparison of these moments with the measured $m_{sat} = 0.65\ \mu_B$ for the $x = 0.5\%$, $T_g = 250$ °C sample indicates that approximately $16 - 20\%$ of the Mn would be in substitutional Si sites. Such a low concentration of Mn would not be expected to give ferromagnetic order in the group III-V DMS. However, a $T_C > 400$ K was obtained in (Ge,Mn) with a concentration of only 0.25% substitutional Mn [129], and a similar analysis performed on Mn-implanted Si samples gives a similar small concentration [34]. The origin of the ferromagnetic order at these low concentrations remains an outstanding issue in these group-IV magnetic semiconductors.

An increase in the Mn concentration to $x \geq 1.5\%$ is sufficient to destroy the second phase. At these concentrations, $m_r(T)$ show a disappearance of the T_{C2} phase and the $m-H$ data indicate a change in the shape of the hysteresis (Fig. 5.8) and a large drop in m_{sat} (Fig. 5.7). Fig. 5.3(a) shows that the morphology of the precipitates changes at $x = 3\%$. The precipitates form larger and more irregularly-shaped clusters. It is possible that by increasing the deposited Mn concentration, a larger fraction of Mn incorporates into the precipitates. Given the low m_{sat} value of the 3% sample that is dominated by $MnSi_{1.7}$ precipitates (Fig. 5.3(b)), it is likely that the $MnSi_{1.7}$ present in the $x = 0.5\%$ samples does not contribute to the high T_C phase, which lends support to the existence of a second DMS phase in the Si matrix.

In conclusion, there are some similarities between the magnetism of the samples discussed here and those discussed in the previous chapter. The disappearance of the high-T_C phase when the Mn concentration exceeds 0.5% at $T_g = 250$ °C is similar to the behavior of region-C samples of Chapter 4, where the high-T_C phase disappears for a Mn coverage above 0.4 ML. This is attributed to the suppression of the DMS

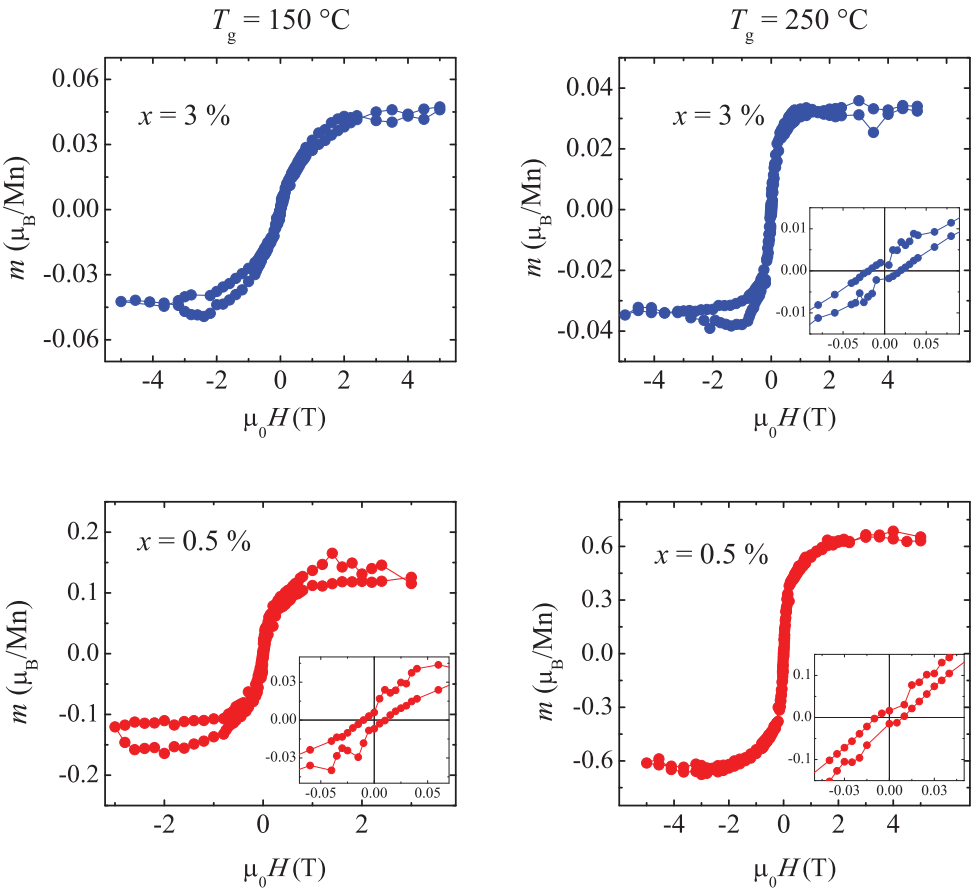

Figure 5.8: Hysteresis loops of Pb-(Si,Mn) samples with Mn concentrations $x = 3\%$ (blue) and 0.5% (red), and growth temperatures $T_g = 150$ °C (left) and $T_g = 250$ °C (right). Measurements were performed at $T = 2$ K.

phase in the Si host. On the other hand, it is believed that the absence of magnetic order in the nanocolumns is related to localized states in an itinerant magnet that form due to disorder.

Chapter 6

Summary and Conclusion

In this thesis, I investigated the influence of growth conditions on the crystal structure and magnetism of Si:Mn thin films prepared by molecular beam epitaxy. In the first study, I examined the growth of $0.35 - 4$ ML of Mn onto Si(001) and uncovered a novel phase with a metastable MnSi-B2-like structure. X-ray absorption fine structure (XAFS) results revealed that the structure of the MnSi film depends on whether the Mn layer was annealed prior to the deposition of the Si cap. When the 0.35 ML film was capped by a Si layer grown at 200 °C, a MnSi with a B2-like crystal structure formed. The MnSi-B2 structure was predicted by DFT calculations to be energetically favorable when Mn is deposited on Si(001) [32, 54, 55], and the work in this thesis represents the first demonstration of this phase, albeit a disordered one. In contrast, samples where the Si cap was grown at -15 °C then annealed to 200 °C had a MnSi-B20-type structure. The magnetic properties of the samples studied in Chapter 3 are shown to be highly sensitive to the Mn coordination, with a possibly stronger influence from the Mn-Mn shell. The B2-like structure has a magnetic moment of 0.33 μ_B and exhibits a ferromagnetic ordering with a T_C above 400 K that is substantially larger than the largest estimated $T_C = 18$ K for the samples with a MnSi-B20-like structure.

In a second study, I introduced a Pb surfactant as a means to control the incorporation of Mn in Si during the growth of Mn δ-doped Si layers. I found that Pb strongly influences the structure and magnetism of the δ-doped films, which were also shown to be sensitive to the Mn coverage, θ_{Mn}, and the growth temperature of the Si capping layer, T_{Si}. Structural and magnetic characterizations identified three distinct

regions in the growth-phase-diagram, where two of the regions created ferromagnetic structures. Samples with 150 °C $\leq T_{Si} \leq$ 200 °C and $\theta_{Mn} \leq 0.4$ ML, have a $T_C > 400$ K and contain nanocrystalline MnSi precipitates with a B2-like crystal structure that coexist with a relatively large fraction of Mn in Si substitutional sites. This high temperature ferromagnetism extends into the third region of the phase-diagram (250 °C $\leq T_{Si} \leq$ 300 °C) where a second magnetic transition at $T_C = 170$ K also exists due to MnSi nano-disks with a MnSi-B20-like crystal structure. Although such a high T_C is not expected from the MnSi-B20 structure and cannot be associated with any known MnSi phase, this result complements previous work on $MnSi_{1.7}$ precipitates [33, 36, 37, 51, 34], and provides an example of different nanocrystalline precipitates in Si with a high T_C. The Anderson model provides a plausible explanation for the formation of the large local moment. In this model, it is assumed that Mn impurities exist within a metallic MnSi-B20 host.

The Pb assisted growth of δ-doped layers showed a mechanism for an intriguing surfactant-enhanced substitutional doping phenomenon. DFT calculations show that a Pb layer on Si reduces the vacancy formation energy by 0.92 eV, which opens the pathway for substitutional doping of Mn into Si. Experimental evidence for this mechanism is found from RBS. In the two ferromagnetic phases, RBS results show that an increase in the remanent moment is possibly correlated with an increase in substitutional-like Mn. This increase is interpreted as an increase in the concentration of substitutional Mn in the Si matrix, which may be mediating the long-range ferromagnetic interaction leading to the observed high T_C.

The presence of a Pb surfactant also significantly impacts the growth kinetics of co-deposited $Si_{1-x}Mn_x$ alloys. Without Pb, a 2D spinodal decomposition produces nanocolumns along the growth direction that extend from the interface up to the capping layer, as also observed in Ref. [69]. These nanocolumns are most likely

amorphous, given the lack of additional diffraction spots in the SADP data. A measurement of the remanent moment down to $T = 2$ K shows that the nanocolumns are paramagnetic with a small Mn magnetic moment. In contrast, the co-deposition of $Si_{1-x}Mn_x$ on a 2 ML Pb-covered Si(001) surface creates a collection of nanocrystalline precipitates, including $MnSi_{1.7}$ nanorods that run along the $\langle 110 \rangle$ directions of the substrate. The SQUID measurements showed that the surfactant dramatically improves the magnetic properties of the dilute alloy at the lowest concentrations. For a concentration $x = 0.5\%$, the Pb-(Si,Mn) samples have a T_C above 400 K. However, this high temperature phase is likely not due to the precipitates, but rather to Mn incorporated coherently into the Si matrix. The fact that Pb decreases the formation energy of vacancies in the Si offers an explanation for the formation of both phases.

This thesis adds an important contribution to the few studies available on the MBE growth of Mn-doped Si. The experiments conducted in this work demonstrate that a careful manipulation of the growth conditions gives rise to intriguing magnetic properties in the Si:Mn system. Interestingly, the results of both Chapters 3 and 4 demonstrate that dusting Mn at the Si interface with a coverage as low as a 1/4 of a ML is enough to turn Si into a high-T_C ferromagnet. While nanoscale inhomogeneities could not be avoided, I showed that it is indeed possible to influence their phase and morphology by optimizing the growth conditions and by introducing a Pb surfactant. Since substitutional incorporation of Mn is a crucial issue in DMS research, the effect of Pb discovered in this work is promising and provides a new opportunity for controlled doping in other DMS systems. Given that there are no known phases of Mn-Si alloys with an above room temperature T_C, the ability to achieve two such phases in this work is also interesting and demonstrates the potential of these materials for spintronic applications. However, the low coercivity of the precipitates and their lack of anisotropy create technological challenges that would have to be overcome.

In both the δ-doped and the dilute alloys investigated in this thesis, there is

evidence of multiple phases. While the existence of precipitates is clear, the evidence for substitutional Mn is more indirect. Although RBS provides the most direct probe of this state, the interpretation is obscured by contributions from the precipitates. However, the MnSi-B2 precipitates have a crystal structure that lies in registry with the lattice where each Mn site corresponds to an interstitial Si site. RBS data for this system therefore gives the strongest support for the existence of substitutional Mn in Si.

The findings of this study open the opportunity for further experimental and theoretical investigations. This thesis demonstrates three different Mn-Si precipitates that can exist in a Si matrix. The origin of the high T_C ferromagnetism remains uncertain, although it is likely that large moments that result from Anderson localization are responsible for the enhanced T_C of the MnSi-B20-rich samples. To further confirm this idea, it would be interesting to probe the density of states near the Fermi level to search for evidence for localized states in the valence band, such as with ultraviolet photoemission spectroscopy (UPS). A measurement of the band structure of Mn-doped Si may also be possible with the newly developed technique of hard (or soft) x-ray angle-resolved photoemission spectroscopy (HARPES), which was recently applied to identify the $3d$ impurity band and its location with respect to the valence band in the (Ga,Mn)As DMS [166, 167].

The nature of the interaction between the metallic nanoclusters and the semiconducting matrix remains an open and interesting question, both in the context of the high T_C, and in terms of what magneto transport properties might be expected. Unlike other DMS systems, magneto transport measurements of Mn doped Si are rarely investigated and the two studies of Refs. [168, 169] report on the measurements performed on amorphous Mn films grown on hydrogenated Si. Transport measurements would confirm whether the samples containing MnSi-B2, MnSi-B20 and $MnSi_{1.7}$ precipitates are metallic. If a gated structure could be constructed, such as that proposed

by Park et al. [26] for Mn_xGe_{1-x}, it may be possible to detect whether a carrier mediated ferromagnetism exists in the samples where a DMS phase is expected to coexist with the precipitates.

The existence of a dilute $Si_{1-x}Mn_x$ phase and its role in ferromagnetism could be further corroborated by theoretical models and by experimental techniques capable of detecting dilute amounts of Mn in the matrix, such as cross-sectional STM (XSTM). Although the dopant identification can be very challenging in XSTM, experimental studies combined with numerical simulations successfully identified the Mn atoms and their localization in GaAs [170, 171]. On the other hand, it would be interesting to use scanning tunneling microscopy and numerical calculations in order to confirm how Pb influences the growth kinetics at the atomic scale.

It would be interesting to investigate whether annealing changes the magnetic properties of the samples containing Mn_xSi_{1-x} nanocolumns, as it did with the Mn_xGe_{1-x} nanocolumns [148]. As for increasing the amount of substitutional Mn, it would be interesting to combine a Pb surfactant with the growth on n-type Si(001) substrates, in light of the DFT prediction that a n-type impurity enhances substitutional Mn [65]. Similarly, Pb can also be combined with Mn doping of $Si_{1-x}Ge_x$, given that substitutional incorporation is predicted to be enhanced in this alloy [62].

Finally, it may be worth exploring if Si wafer bonding can be used instead of growing a Si capping layer. Wafer bonding can be relatively easy to achieve in MBE by bringing two smooth, clean surfaces into contact with each other [172], for example, a Mn covered Si(001) and a clean Si(001) wafers together. The advantage of this technique is that it eliminates the need of increasing the temperature to grow a crystalline Si cap once the Mn have been deposited at low temperature. By avoiding this high temperature step, it is possible to reduce the mobility of Mn atoms and keep them trapped in the sites they occupied during the growth.

Bibliography

[1] M. N. Baibich, J. M. Broto, A. Fert, F. Nguyen Van Dau, F. Petroff, P. Etienne, G. Creuzet, A. Friederich, and J. Chazelas. Giant magnetoresistance of (001)Fe/(001)Cr magnetic superlattices. *Phys. Rev. Lett.*, 61:2472–2475, Nov 1988.

[2] G. Binasch, P. Grünberg, F. Saurenbach, and W. Zinn. Enhanced magnetoresistance in layered magnetic structures with antiferromagnetic interlayer exchange. *Phys. Rev. B*, 39:4828–4830, Mar 1989.

[3] IBM Research, http://www.research.ibm.com/research/gmr.html.

[4] S. Datta and B. Das. Electronic analog of the electro-optic modulator. *Applied Physics Letters*, 56(7):665–667, 1990.

[5] R. Fiederling, M. Keim, G. Reuscher, W. Ossau, G. Schmidt, A. Waag, and L. W. Molenkamp. Injection and detection of a spin-polarized current in a light-emitting diode. *Nature*, 402:787–790, January 1999.

[6] G. Prinz and K. Hathaway. Special issue: Magnetoelectronics. *Physics Today*, 48(4):24–25, 1995.

[7] Y. Ohno, D. K. Young, B. Beschoten, F. Matsukura, H. Ohno, and D. D. Awschalom. Electrical spin injection in a ferromagnetic semiconductor heterostructure. *Nature*, 402:790–792, January 1999.

[8] M. Özer, C. Zeng, and H. Weitering. Magnetic doping of group IV semiconductors. In W.M. Chen and I.A. Buyanova, editors, *Handbook of Spintornic Semiconductors*, chapter 7, pages 193 – 223. Pan Stanford, 2010.

[9] A. Bonanni and T. Dietl. A story of high-temperature ferromagnetism in semiconductors. *Chem. Soc. Rev.*, 39:528–539, 2010.

[10] H. Akinaga, S. Miyanishi, K. Tanaka, W. Van Roy, and K. Onodera. Magneto-optical properties and the potential application of GaAs with magnetic MnAs nanoclusters. *Appl. Phys. Lett.*, 76(1):97–99, 2000.

[11] S. Kuroda, N. Nishizawa, K. Takita, M. Mitome, Y. Bando, K. Osuch, and T. Dietl. Origin and control of high-temperature ferromagnetism in semiconductors. *Nat. Mater.*, 6(6):440–446, 06 2007.

[12] T. Dietl, D.D. Awschalom, M. Kaminska, and H. Ohno. *Spintronics*. Semiconductors and semimetals. Elsevier Science, 2009.

[13] S. A. Crooker, D. D. Awschalom, J. J. Baumberg, F. Flack, and N. Samarth. Optical spin resonance and transverse spin relaxation in magnetic semiconductor quantum wells. *Phys. Rev. B*, 56:7574–7588, Sep 1997.

[14] M. Goryca, T. Kazimierczuk, M. Nawrocki, A. Golnik, J. A. Gaj, P. Kossacki, P. Wojnar, and G. Karczewski. Optical manipulation of a single Mn spin in a CdTe-based quantum dot. *Phys. Rev. Lett.*, 103:087401, Aug 2009.

[15] C. Le Gall, L. Besombes, H. Boukari, R. Kolodka, J. Cibert, and H. Mariette. Optical spin orientation of a single manganese atom in a semiconductor quantum dot using quasiresonant photoexcitation. *Phys. Rev. Lett.*, 102:127402, Mar 2009.

[16] T. Jungwirth, Jairo Sinova, J. Mašek, J. Kučera, and A. H. MacDonald. Theory of ferromagnetic (III,Mn)V semiconductors. *Rev. Mod. Phys.*, 78:809–864, Aug 2006.

[17] T. Jungwirth, K. Y. Wang, J. Mašek, K. W. Edmonds, Jürgen König, Jairo Sinova, M. Polini, N. A. Goncharuk, A. H. MacDonald, M. Sawicki, A. W. Rushforth, R. P. Campion, L. X. Zhao, C. T. Foxon, and B. L. Gallagher. Prospects for high temperature ferromagnetism in (Ga,Mn)As semiconductors. *Phys. Rev. B*, 72:165204, Oct 2005.

[18] X. Luo, S. B. Zhang, and S.-H. Wei. Theory of Mn supersaturation in Si and Ge. *Phys. Rev. B*, 70:033308, Jul 2004.

[19] H. Munekata, H. Ohno, S. von Molnar, Armin Segmüller, L. L. Chang, and L. Esaki. Diluted magnetic III-V semiconductors. *Phys. Rev. Lett.*, 63:1849–1852, Oct 1989.

[20] H. Ohno, H. Munekata, T. Penney, S. von Molnár, and L. L. Chang. Magnetotransport properties of p -type (In,Mn)As diluted magnetic III-V semiconductors. *Phys. Rev. Lett.*, 68:2664–2667, Apr 1992.

[21] H. Ohno, A. Shen, F. Matsukura, A. Oiwa, A. Endo, S. Katsumoto, and Y. Iye. (Ga,Mn)As: A new diluted magnetic semiconductor based on GaAs. *Applied Physics Letters*, 69(3):363–365, 1996.

[22] F. Xiu. Magnetic Mn-doped Ge nanostructures. *ISRN Condensed Matter Physics*, 2012:1–25, 2012.

[23] Ferromagnetic Semiconductor Spintronic Web Project, http://unix12.fzu.cz/ms/navigate.php?cont=public_in.

[24] M. Wang, R. P. Campion, A. W. Rushforth, K. W. Edmonds, C. T. Foxon, and B. L. Gallagher. Achieving high Curie temperature in (Ga,Mn)As. *Applied Physics Letters*, 93(13):132103, 2008.

[25] T. Dietl, H. Ohno, F. Matsukura, J. Cibert, and D. Ferrand. Zener model description of ferromagnetism in zinc-blende magnetic semiconductors. *Science*, 287(5455):1019–1022, 2000.

[26] Y. D. Park, A. T. Hanbicki, S. C. Erwin, C. S. Hellberg, J. M. Sullivan, J. E. Mattson, T. F. Ambrose, A. Wilson, G. Spanos, and B. T. Jonker. A group-IV ferromagnetic semiconductor: Mn_xGe_{1x}. *Science*, 295(5555):651–654, 2002.

[27] A. P. Li, J. Shen, J. R. Thompson, and H. H. Weitering. Ferromagnetic percolation in Mn_xGe_{1-x} dilute magnetic semiconductor. *Applied Physics Letters*, 86(15):152507–, 2005.

[28] A. M. Tyryshkin, S. A. Lyon, A. V. Astashkin, and A. M. Raitsimring. Electron spin relaxation times of phosphorus donors in silicon. *Phys. Rev. B*, 68:193207, Nov 2003.

[29] E. Weber. Transition metals in silicon. *Applied Physics A*, 30:1–22, 1983.

[30] A.B. Gokhale and R. Abbaschian. The Mn-Si (manganese-silicon) system. *Bulletin of Alloy Phase Diagrams*, 11:468–480, 1990.

[31] A.B. Gokhale and R. Abbaschian. The Ge-Mn (germanium-manganese) system. *Bulletin of Alloy Phase Diagrams*, 11:460–468, 1990.

[32] H. Wu, M. Hortamani, P. Kratzer, and M. Scheffler. First-principles study of ferromagnetism in epitaxial Si-Mn thin films on Si(001). *Phys Rev Lett*, 92(23):237202, 2004.

[33] M. Bolduc, C. Awo-Affouda, A. Stollenwerk, M. B. Huang, F. G. Ramos, G. Agnello, and V. P. LaBella. Above room temperature ferromagnetism in Mn-ion implanted Si. *Phys. Rev. B*, 71:033302–, 2005.

[34] V. Ko, K. L. Teo, T. Liew, T. C. Chong, M. MacKenzie, I. MacLaren, and J. N. Chapman. Origins of ferromagnetism in transition-metal doped Si. *J. Appl. Phys.*, 104:033912, 2008.

[35] M. Jamet, A. Barski, T. Devillers, V. Poydenot, R. Dujardin, P. Bayle-Guillemaud, J. Rothman, E. Bellet-Amalric, A. Marty, J. Cibert, R. Mattana, and S. Tatarenko. High-Curie-temperature ferromagnetism in self-organized $Ge_{1-x}Mn_x$ nanocolumns. *Nat. Mater.*, 5(8):653–659, 2006.

[36] C. Awo-Affouda, M. Bolduc, M. B. Huang, F. Ramos, K. A. Dunn, B. Thiel, G. Agnello, and V. P. LaBella. Observation of crystallite formation in ferromagnetic Mn-implanted Si. *Journal of Vacuum Science and Technology A*, 24(4):1644–1647, 2006.

[37] S. Zhou, K. Potzger, G. Zhang, A. Mücklich, F. Eichhorn, N. Schell, R. Grötzschel, B. Schmidt, W. Skorupa, M. Helm, J. Fassbender, and D Geiger. Structural and magnetic properties of Mn implanted Si. *Phys. Rev. B*, 75:085203–, 2007.

[38] V. N. Men'shov, V. V. Tugushev, S. Caprara, and E. V. Chulkov. High-temperature ferromagnetism in Si:Mn alloys. *Phys. Rev. B*, 83(3):035201, Jan 2011.

[39] U. Gottlieb, A. Sulpice, B. Lambert-Andron, and O. Laborde. Magnetic properties of single crystalline Mn_4Si_7. *J. Alloys Compd.*, 361(1-2):13 – 18, 2003.

[40] C. Zener. Interaction between the *d* shells in the transition metals. *Phys. Rev.*, 81:440–444, Feb 1951.

[41] T. Dietl. A ten-year perspective on dilute magnetic semiconductors and oxides. *Nat. Mater.*, 9:965 – 974, 2010.

[42] A. Kaminski and S. Das Sarma. Polaron percolation in diluted magnetic semiconductors. *Phys. Rev. Lett.*, 88:247202, May 2002.

[43] S. Das Sarma, E. H. Hwang, and A. Kaminski. Temperature-dependent magnetization in diluted magnetic semiconductors. *Phys. Rev. B*, 67:155201, Apr 2003.

[44] A. Stroppa, S. Picozzi, A. Continenza, and A. J. Freeman. Electronic structure and ferromagnetism of Mn-doped group-IV semiconductors. *Phys. Rev. B*, 68(15):155203, Oct 2003.

[45] Q. Liu, W. Yan, H. Wei, Z. Sun, Z. Pan, A. V. Soldatov, C. Mai, C. Pei, X. Zhang, Y. Jiang, and S. Wei. Energetic stability, electronic structure, and magnetism in Mn-doped silicon dilute magnetic semiconductors. *Phys. Rev. B*, 77:245211, Jun 2008.

[46] F. M. Zhang, X. C. Liu, J. Gao, X. S. Wu, Y. W. Du, H. Zhu, J. Q. Xiao, and P. Chen. Investigation on the magnetic and electrical properties of crystalline $Mn_{0.05}Si_{0.95}$ films. *Appl. Phys. Lett.*, 85(5):786–788, 2004.

[47] Shoichi T. and Hiroshi W. Helical spin structure of Mn_3Si. *Journal of the Physical Society of Japan*, 39(2):295–302, 1975.

[48] A. Z. Menshikov, A. P. Vokhmyanin, and Yu A. Dorofeev. Magnetic structure and phase transformations in Mn_5Si_3. *physica status solidi (b)*, 158(1):319–328, 1990.

[49] Y. Ishikawa, K. Tajima, D. Bloch, and M. Roth. Helical spin structure in manganese silicide MnSi. *Solid State Communications*, 19(6):525, 1976.

[50] T. Nakajima and J. Schelten. Peculiarities of the band magnetism in the higher manganese silicide. *Journal of Magnetism and Magnetic Materials*, 21(2):157, 1980.

[51] A. Orlov, A. Granovsky, L. Balagurov, I. Kulemanov, Yu. Parkhomenko, N. Perov, E. Gan'shina, V. Bublik, K. Shcherbachev, A. Kartavykh, V. Vdovin, A. Sapelkin, V. Saraikin, Yu. Agafonov, V. Zinenko, A. Rogalev, and A. Smekhova. Structure, electrical and magnetic properties, and the origin of the room temperature ferromagnetism in Mn-implanted Si. *J. Exp. Theor. Phys.*, 109:602–608, 2009. 10.1134/S1063776109100069.

[52] S. Yabuuchi, H. Kageshima, Y. Ono, M. Nagase, A. Fujiwara, and E. Ohta. Origin of ferromagnetism of $MnSi_{1.7}$ nanoparticles in Si: First-principles calculations. *Phys. Rev. B*, 78(4):045307, Jul 2008.

[53] M. M. Otrokov, A. Ernst, V. V. Tugushev, S. Ostanin, P. Buczek, L. M. Sandratskii, G. Fischer, W. Hergert, I. Mertig, V. M. Kuznetsov, and E. V. Chulkov. *Ab initio* study of the magnetic ordering in Si/Mn digital alloys. *Phys. Rev. B*, 84:144431, Oct 2011.

[54] M. Hortamani, H. Wu, P. Kratzer, and M. Scheffler. Epitaxy of Mn on Si(001): Adsorption, surface diffusion, and magnetic properties studied by density-functional theory. *Phys. Rev. B*, 74:205305, Nov 2006.

[55] M. Hortamani, L. Sandratskii, P. Kratzer, I. Mertig, and M. Scheffler. Exchange interactions and critical temperature of bulk and thin films of MnSi: A density functional theory study. *Phys. Rev. B*, 78(10):104402–, 2008.

[56] S. Walter, F. Blobner, M. Krause, S. Müller, K. Heinz, and U. Starke. Interface structure and stabilization of metastable B2-FeSi/Si(111) studied with low-energy electron diffraction and density functional theory. *Journal of Physics: Condensed Matter*, 15(30):5207, 2003.

[57] H. von Känel, C. Schwarz, S. Goncalves-Conto, E. Müller, L. Miglio, F. Tavazza, and G. Malegori. New epitaxially stabilized CoSi phase with the CsCl structure. *Phys. Rev. Lett.*, 74(7):1163–1166, Feb 1995.

[58] J. E. Jørgensen and S. E. Rasmussen. Refinement of the structure of MnSi by powder diffraction. *Powder Diffraction*, 6:194–195, 11 1991.

[59] G. M. Dalpian, Antônio J. R. da Silva, and A. Fazzio. Theoretical investigation of a possible Mn_xSi_{1-x} ferromagnetic semiconductor. *Phys. Rev. B*, 68:113310, Sep 2003.

[60] G.M. Dalpian, Antnio J.R. da Silva, and A. Fazzio. Adsorption of Mn atoms on the Si(100) surface. *Surface Science*, 566-568, Part 2(0):688 – 692, 2004. Proceedings of the 22nd European Conference on Surface Science.

[61] Z. Z. Zhang, B. Partoens, Kai Chang, and F. M. Peeters. First-principles study of transition metal impurities in Si. *Phys. Rev. B*, 77:155201, Apr 2008.

[62] Antônio J. R. da Silva, A. Fazzio, and Alex Antonelli. Stabilization of substitutional Mn in silicon-based semiconductors. *Phys. Rev. B*, 70:193205, Nov 2004.

[63] M. R. Krause, A. J. Stollenwerk, J. Reed, V. P. LaBella, M. Hortamani, P. Kratzer, and M. Scheffler. Electronic structure changes of Si (001) (2×1) from subsurface Mn observed by STM. *Phys. Rev. B*, 75(20):205326, May 2007.

[64] S. Yabuuchi, E. Ohta, H. Kageshima, and A. Taguchi. First-principles study of strain effects on Mn in Si. *Physica B*, 376-377:672, 2006.

[65] W. Zhu, Z. Zhang, and E. Kaxiras. Dopant-assisted concentration enhancement of substitutional Mn in Si and Ge. *Physical Review Letters*, 100(2):027205, January 2008.

[66] H. Wu, P. Kratzer, and M. Scheffler. Density-functional theory study of half-metallic heterostructures: Interstitial Mn in Si. *Phys. Rev. Lett.*, 98(11):117202, Mar 2007.

[67] J. Ye, Y. Jiang, Q. Liu, T. Yao, Z. Pan, H. Oyanagi, Z. Sun, W. Yan, and S. Wei. Cosputtered Mn-doped Si thin films studied by x-ray spectroscopy. *Journal of Applied Physics*, 106(10):103517, 2009.

[68] A. Wolska, K. Lawniczak-Jablonska, M. Klepka, M. S. Walczak, and A. Misiuk. Local structure around Mn atoms in Si crystals implanted with Mn^+ studied using x-ray absorption spectroscopy techniques. *Phys. Rev. B*, 75(11):113201, Mar 2007.

[69] Y. T. Zhang, Q. Jiang, D. J. Smith, and J. Drucker. Growth and characterization of $Si_{1-x}Mn_x$ alloys on Si(100). *J. Appl. Phys.*, 98(3):033512, August 2005.

[70] M. Bolduc, C. Awo-Affouda, A. Stollenwerk, M.B. Huang, F. Ramos, and V.P. LaBella. Investigation of the structural properties of ferromagnetic Mn-implanted Si. *Nuclear Instruments and Methods in Physics Research B*, 242(12):367 – 370, 2006.

[71] H. Liu and P. Reinke. Formation of manganese nanostructures on the Si(100) (2 ×1) surface. *Surf. Sci.*, 602(4):986 – 992, 2008.

[72] C. A. Nolph, H. Liu, and P. Reinke. Bonding geometry of Mn-wires on the Si(100) (2 × 1) surface. *Surf. Sci.*, 605(13-14):L29 – L32, 2011.

[73] J.-T. Wang, C. Chen, E. Wang, and Y. Kawazoe. Magic monatomic linear chains for Mn nanowire self-assembly on Si(001). *Phys. Rev. Lett.*, 105:116102, Sep 2010.

[74] K. R. Simov, C. A. Nolph, and P. Reinke. Guided self-assembly of Mn wires on the Si(100) (2×1) surface. *The Journal of Physical Chemistry C*, 116(2):1670–1678, 2012.

[75] H. Lippitz, J. J. Paggel, and P. Fumagalli. Bimodal growth of manganese silicide on Si(100). *Surface Science*, 575(3):307–312, 2/1 2005.

[76] E. F. Schubert and K. Ploog. The δ-doped field-effect transistor. *Japanese Journal of Applied Physics*, 24(Part 2, No. 8):L608–L610, 1985.

[77] E. F. Schubert, J. E. Cunningham, W. T. Tsang, and G. L. Timp. Selectively delta-doped $Al_xGa_{1-x}As$/GaAs heterostructures with high two-dimensional electron-gas concentrations $n_{2DEG} \geq 1.5 \times 10^{12}$ cm^{-2} for field-effect transistors. *Applied Physics Letters*, 51(15):1170–1172, 1987.

[78] E. F. Schubert, B. Ullrich, T. D. Harris, and J. E. Cunningham. Quantum-confined interband absorption in GaAs sawtooth-doping superlattices. *Phys. Rev. B*, 38:8305–8308, Oct 1988.

[79] R. K. Kawakami, E. Johnston-Halperin, L. F. Chen, M. Hanson, N. Guébels, J. S. Speck, A. C. Gossard, and D. D. Awschalom. (Ga,Mn)As as a digital ferromagnetic heterostructure. *Applied Physics Letters*, 77(15):2379–2381, 2000.

[80] X. Chen, M. Na, M. Cheon, S. Wang, H. Luo, B. D. McCombe, X. Liu, Y. Sasaki, T. Wojtowicz, J. K. Furdyna, S. J. Potashnik, and P. Schiffer. Above-room-temperature ferromagnetism in GaSb/Mn digital alloys. *Applied Physics Letters*, 81(3):511–513, 2002.

[81] A. M. Nazmul, S. Sugahara, and M. Tanaka. Ferromagnetism and high Curie temperature in semiconductor heterostructures with Mn δ-doped GaAs and p-type selective doping. *Phys. Rev. B*, 67:241308, Jun 2003.

[82] A. M. Nazmul, T. Amemiya, Y. Shuto, S. Sugahara, and M. Tanaka. High temperature ferromagnetism in GaAs-based heterostructures with Mn δ doping. *Phys. Rev. Lett.*, 95:017201, Jun 2005.

[83] S. H. Chiu, H. S. Hsu, and J. C. A. Huang. The molecular beam epitaxy growth, structure, and magnetism of $Si_{1-x}Mn_x$ films. *Journal of Applied Physics*, 103(7):07D110, 2008.

[84] M. C. Qian, C. Y. Fong, Kai Liu, W. E. Pickett, J. E. Pask, and L. H. Yang. Half-metallic digital ferromagnetic heterostructure composed of a δ-doped layer of Mn in Si. *Phys. Rev. Lett.*, 96:027211, Jan 2006.

[85] T. J. Burke. Continued quest for understanding the impact of annealing upon delta-doped Mn on Si(100). Dalhousie University, 2007.

[86] D. J. Eaglesham, H.-J. Gossmann, and M. Cerullo. Limiting thickness h_{epi} for epitaxial growth and room-temperature Si growth on Si(100). *Phys. Rev. Lett.*, 65:1227–1230, Sep 1990.

[87] B. Voigtländer, A. Zinner, T. Weber, and H. P. Bonzel. Modification of growth-kinetics in surfactant-mediated epitaxy. *Phys. Rev. B*, 51(12):7583–7591, March 1995.

[88] D. Kandel and E. Kaxiras. The surfactant effect in semiconductor thin-film growth. *Solid State Physics: Advances In Research and Applications, Vol. 54*, 54:219–262, 2000.

[89] C. Y. Fong, M. D. Watson, L. H. Yang, and S. Ciraci. Surfactant-mediated growth of semiconductor materials. *Modelling and Simulation in Materials Science and Engineering*, 10(5):R61, 2002.

[90] J. Y. Zhu, F. Liu, and G. B. Stringfellow. Dual-surfactant effect to enhance p-type doping in III-V semiconductor thin films. *Phys. Rev. Lett.*, 101:196103, Nov 2008.

[91] J. Zhu, F. Liu, and G.B. Stringfellow. Enhanced cation-substituted p-type doping in GaP from dual surfactant effects. *J. Cryst. Growth*, 312(2):174 – 179, 2010.

[92] L. Zhang, Y. Yan, and S.-H. Wei. Enhancing dopant solubility via epitaxial surfactant growth. *Phys. Rev. B*, 80:073305, Aug 2009.

[93] P. G. Evans, O. D. Dubon, J. F. Chervinsky, F. Spaepen, and J. A. Golovchenko. Low-temperature homoepitaxial growth on Si(111) through a Pb monolayer. *Applied Physics Letters*, 73:3120, 1998.

[94] Q. F. Xiao, S. Kahwaji, T. L. Monchesky, R. A. Gordon, and E. D. Crozier. Local environment of Mn in Mn delta-doped Si layers. *J. Phys.: Conf. Ser.*, 190:012101, 2009.

[95] M. R. Krause, A. Stollenwerk, M. Licurse, and V. P. LaBella. Ostwald ripening of manganese silicide islands on Si(001). *Journal of Vacuum Science and Technology A*, 24(4):1480–1483, 2006.

[96] W. Kern and D.A. Puotien. Cleaning solutions based on hydrogen peroxide for use in silicon semiconductor technology. *RCA Rev.*, 31:187–206, 1970.

[97] W. Kern. The evolution of silicon wafer cleaning technology. *Journal of The Electrochemical Society*, 137(6):1887–1892, 1990.

[98] M. Sakurai, J. Ryuta, E. Morita, K. Tanaka, T. Yoshimi, and Y. Shimanuki. *Extended Abstracts of The Elctrochemical Society*, volume 90-1. The Elctrochemical Society, Pennington, NJ, 1990.

[99] S. R. Johnson. *Optical bandgap thermometry in molecular beam epitaxy*. PhD thesis, The University of British Columbia, 1995.

[100] W. Braun. *Applied RHEED: Reflection High-Energy Electron Diffraction During Crystal Growth*. Number 154 in Tracts in Modern Physics Series. Springer-Verlag, 1999.

[101] J. E. Mahan, K. M. Geib, G. Y. Robinson, and R. G. Long. A review of the geometrical fundamentals of reflection high-energy electron diffraction with application to silicon surfaces. *Journal of Vacuum Science & Technology A: Vacuum, Surfaces, and Films*, 8(5):3692–3700, 1990.

[102] R.G. Zhao, J.F. Jia, and W.S. Yang. Surface superstructures of the Pb/Si(001) system. *Surface Science*, 274(2):L519 – L523, 1992.

[103] L. Li, C. Koziol, K. Wurm, Y. Hong, E. Bauer, and I. S. T. Tsong. Surface morphology of Pb overlayers grown on Si(100) (2×1). *Phys. Rev. B*, 50:10834–10842, Oct 1994.

[104] T.L. Alford, L.C. Feldman, and J.W. Mayer. *Fundamentals of Nanoscale Film Analysis*. Springer, 2007.

[105] H.R. Verma. *Atomic and Nuclear Analytical Methods: XRF, Mössbauer, XPS, NAA and Ion-beam Spectroscopic Techniques*. Springer, 2007.

[106] Stopping power of light ions, http://www.exphys.uni-linz.ac.at/stopping/.

[107] D.C. Koningsberger and R. Prins. *X-Ray Absorption: Principles, Applications, Techniques of EXAFS, SEXAFS and XANES*. Chemical Analysis. Wiley, 1988.

[108] G. Bunker. *Introduction to XAFS: a practical guide to x-ray absorption fine structure spectroscopy*. Cambridge University Press, Cambridge, UK, 2010.

[109] S. D. Kelly, D. Hesterberg, and B. Ravel. Analysis of soils and minerals using x-ray absorption spectroscopy. In *Methods of Soil Analysis: Mineralogical methods*, volume 5 of *Soil Science Society of America Book Series*, chapter 14, pages 387 – 464. Soil Science Society of America, 2008.

[110] S. H. Baker, M. Roy, S. J. Gurman, and C. Binns. Extended x-ray absorption fine structure studies of the atomic structure of nanoparticles in different metallic matrices. *Journal of Physics: Condensed Matter*, 21(18):183002, 2009.

[111] D. E. Sayers, E. A. Stern, and F. W. Lytle. New technique for investigating noncrystalline structures: Fourier analysis of the extended x-ray absorption fine structure. *Phys. Rev. Lett.*, 27:1204–1207, Nov 1971.

[112] E. A. Stern. Theory of the extended x-ray-absorption fine structure. *Phys. Rev. B*, 10:3027–3037, Oct 1974.

[113] P. A. Lee and J. B. Pendry. Theory of the extended x-ray absorption fine structure. *Phys. Rev. B*, 11:2795–2811, Apr 1975.

[114] S. J. Gurman, N. Binsted, and I. Ross. A rapid, exact curved-wave theory for EXAFS calculations. *Journal of Physics C: Solid State Physics*, 17(1):143, 1984.

[115] E. A. Stern. Structural determination by x-ray absorption. *Contemp. Phys*, 19:239–310, 1978.

[116] E. A. Stern and Helad S. M. Basic principles and applications of EXAFS. In E. E. Koch, editor, *Handbook of Synchrotron Radiation*, volume 10, chapter 10, pages 995 – 1014. North-Holland, Amsterdam, 1983.

[117] J. J. Rehr and R. C. Albers. Scattering-matrix formulation of curved-wave multiple-scattering theory: Application to x-ray-absorption fine structure. *Phys. Rev. B*, 41:8139–8149, Apr 1990.

[118] A. L. Ankudinov, B. Ravel, J. J. Rehr, and S. D. Conradson. Real-space multiple-scattering calculation and interpretation of x-ray-absorption near-edge structure. *Phys.Rev.B*, 58(12):7565–7576, Sep 1998.

[119] E. Karhu, S. Kahwaji, T. L. Monchesky, C. Parsons, M. D. Robertson, and C. Maunders. Structure and magnetic properties of MnSi epitaxial thin films. *Phys. Rev. B*, 82(18):184417, November 2010.

[120] S. M. Heald, D. L. Brewe, E. A. Stern, K. H. Kim, F. C. Brown, D. T. Jiang, E. D. Crozier, and R. A. Gordon. XAFS and micro-XAFS at the PNC-CAT beamlines. *J. Synchrotron Rad*, 6:347, 1999.

[121] T. Ressler. WinXAS : A new software package not only for the analysis of energy-dispersive XAS data. *J. Phys. IV France*, 7(C2):C2–269–C2–270, 1997.

[122] B. Ravel and M. Newville. ATHENA, ARTEMIS, HEPHAESTUS: data analysis for x-ray absorption spectroscopy using IFEFFIT. *J. Synchrotron Rad*, 12:537–541, 2005.

[123] E. A. Stern. Number of relevant independent points in x-ray-absorption fine-structure spectra. *Phys. Rev. B*, 48:9825–9827, Oct 1993.

[124] F. W. Lytle, D. E. Sayers, and E. A. Stern. Report of the international workshop on standards and criteria in x-ray absorption spectroscopy. *Physica B: Condensed Matter*, 158(1-3):701 – 722, 1989.

[125] D. T. Jiang, E. D. Crozier, and B. Heinrich. Structure determination of metastable epitaxial Cu layers on Ag(001) by glancing-incidence x-ray-absorption fine structure. *Phys. Rev. B*, 44:6401–6409, Sep 1991.

[126] M. McElfresh. Fundamentals of Magnetism and Magnetic Measurements: Featuring Quantum Design's Magnetic Property Measurement System. Quantum Design, www.qdusa.com, 1994.

[127] A. Ney, T. Kammermeier, V. Ney, K. Ollefs, and S. Ye. Limitations of measuring small magnetic signals of samples deposited on a diamagnetic substrate. *Journal of Magnetism and Magnetic Materials*, 320(23):3341 – 3346, 2008.

[128] A. Ney, R. Rajaram, S. S. P. Parkin, T. Kammermeier, and S. Dhar. Experimental investigation of the metastable magnetic properties of Cr-doped InN. *Phys. Rev. B*, 76:035205, Jul 2007.

[129] C. Zeng, Z. Zhang, K. van Benthem, M. F. Chisholm, and H. H. Weitering. Optimal doping control of magnetic semiconductors via subsurfactant epitaxy. *Phys. Rev. Lett.*, 100:066101, Feb 2008.

[130] C. Braun. Parratt32 program, version 1.6.0. (Berlin: Berlin-Neutron Scattering Center [BENSCI] Hanh-Meiner Institut), 2002.

[131] L. G. Parratt. Surface studies of solids by total reflection of x-rays. *Phys. Rev.*, 95:359–369, Jul 1954.

[132] M. E. Fisher and M. N. Barber. Scaling theory for finite-size effects in the critical region. *Phys.Rev.Lett.*, 28(23):1516–1519, Jun 1972.

[133] M. Hortamani, P. Kratzer, and M. Scheffler. Density-functional study of Mn monosilicide on the Si(111) surface: Film formation versus island nucleation. *Phys.Rev.B*, 76(23):235426, Dec 2007.

[134] J. U. Andersen, O. Andreasen, J. A. Davies, and E. Uggerhj. The use of channeling-effect techniques to locate interstitial foreign atoms in silicon. *Radiation Effects*, 7(1-2):25–34, 1971.

[135] K. R. Bauchspiess. *A Study of the Pressure-induced Mixed-valence Transition in SmSe and SmS by X-ray Absorption Spectroscopy.* PhD thesis, Simon Fraser University, 1991.

[136] M. D. Robertson, T. Burns, and T. Morrison. The preparation of semiconductor TEM specimens by low-angle polishing. *Microscopy Society of Canada Bulletin*, 34:19, 2006.

[137] Y. C. Lian and L. J. Chen. Localized epitaxial growth of $MnSi_{1.7}$ on silicon. *Applied Physics Letters*, 48:359–, 1986.

[138] S. Zhou, A. Shalimov, K. Potzger, M. Helm, J. Fassbender, and H. Schmidt. $MnSi_{1.7}$ nanoparticles embedded in Si: Superparamagnetism with collective behavior. *Phys. Rev. B*, 80(17):174423, 2009.

[139] F. d'Acapito, G. Smolentsev, F. Boscherini, M. Piccin, G. Bais, S. Rubini, F. Martelli, and A. Franciosi. Site of Mn in Mn δ-doped GaAs: X-ray absorption spectroscopy. *Phys. Rev. B*, 73:035314, 2006.

[140] G. Kresse and J. Hafner. *Ab initio* molecular-dynamics simulation of the liquid-metal amorphous-semiconductor transition in germanium. *Phys. Rev. B*, 49:14251–14269, May 1994.

[141] G. Kresse and J. Furthmüller. Efficiency of ab-initio total energy calculations for metals and semiconductors using a plane-wave basis set. *Comput. Matter. Sci.*, 6(1):15 – 50, 1996.

[142] P. E. Blöchl. Projector augmented-wave method. *Phys. Rev. B*, 50:17953–17979, Dec 1994.

[143] G. Kresse and D. Joubert. From ultrasoft pseudopotentials to the projector augmented-wave method. *Phys. Rev. B*, 59:1758–1775, Jan 1999.

[144] S. Froyen, D. M. Wood, and A. Zunger. Electronic structure of [110] Si-Ge thin-layer superlattices. *Appl. Phys. Lett.*, 54(24):2435–2437, 1989.

[145] M. E. González-Méndez and N. Takeuchi. First-principles calculations of the initial growth of Pb on Si(100). *Phys. Rev. B*, 58:16172–16176, Dec 1998.

[146] K. Tono, H. W. Yeom, I. Matsuda, and T. Ohta. Electronic structure of the Si(001) surface with Pb adsorbates. *Phys. Rev. B*, 61:15866–15872, Jun 2000.

[147] S. Kahwaji, R. A. Gordon, E. D. Crozier, and T. L. Monchesky. Local structure and magnetic properties of B2- and B20-like ultrathin Mn films grown on Si(001). *Phys. Rev. B*, 85:014405, Jan 2012.

[148] A. P. Li, C. Zeng, K. van Benthem, M. F. Chisholm, J. Shen, S. V. S. Nageswara Rao, S. K. Dixit, L. C. Feldman, A. G. Petukhov, M. Foygel, and H. H. Weitering. Dopant segregation and giant magnetoresistance in manganese-doped germanium. *Phys. Rev. B*, 75:201201, May 2007.

[149] F. Bernardini, S. Picozzi, and A. Continenza. Energetic stability and magnetic properties of Mn dimers in silicon. *Applied Physics Letters*, 84(13):2289–2291, 2004.

[150] E. A. Karhu, U. K. Rößler, A. N. Bogdanov, S. Kahwaji, B. J. Kirby, H. Fritzsche, M. D. Robertson, C. F. Majkrzak, and T. L. Monchesky. Chiral modulations and reorientation effects in MnSi thin films. *Phys. Rev. B*, 85:094429, Mar 2012.

[151] P. W. Anderson. Localized magnetic states in metals. *Phys. Rev.*, 124:41–53, 1961.

[152] H. Weng and J. Dong. First-principles investigation of transition-metal-doped group-IV semiconductors: $R_x Y_{1-x}$ (R=Cr,Mn,Fe; Y=Si,Ge). *Phys. Rev. B*, 71:035201, 2005.

[153] W. F. Brown. Thermal fluctuations of a single-domain particle. *Phys. Rev.*, 130:1677–1686, 1963.

[154] D. Bougeard, S. Ahlers, A. Trampert, N. Sircar, and G. Abstreiter. Clustering in a precipitate-free GeMn magnetic semiconductor. *Phys. Rev. Lett.*, 97:237202, Dec 2006.

[155] M. Moreno, A. Trampert, B. Jenichen, L. Däweritz, and K. H. Ploog. Correlation of structure and magnetism in GaAs with embedded Mn(Ga)As magnetic nanoclusters. *J. Appl. Phys.*, 92(8):4672–4677, 2002.

[156] K. Sato, H. Katayama-Yoshida, and P. H. Dederichs. High Curie temperature and nano-scale spinodal decomposition phase in dilute magnetic semiconductors. *Japanese Journal of Applied Physics*, 44(30):L948–L951, 2005.

[157] A. Chakraborty, R. Bouzerar, S. Kettemann, and G. Bouzerar. Nanoscale inhomogeneities: A new path toward high Curie temperature ferromagnetism in diluted materials. *Phys. Rev. B*, 85:014201, Jan 2012.

[158] T. Devillers, M. Jamet, A. Barski, V. Poydenot, P. Bayle-Guillemaud, E. Bellet-Amalric, S. Cherifi, and J. Cibert. Structure and magnetism of self-organized $Ge_{1-x}Mn_x$ nanocolumns on Ge(001). *Phys. Rev. B*, 76:205306, Nov 2007.

[159] T. Fukushima, K. Sato, H. Katayama-Yoshida, and P. H. Dederichs. Spinodal decomposition under layer by layer growth condition and high Curie temperature quasi-one-dimensional nano-structure in dilute magnetic semiconductors. *Jpn. J. Appl. Phys.*, 45(12-16):L416–L418, 2006.

[160] L. Gu, S. Y. Wu, H.X. Liu, R.K. Singh, N. Newman, and David J. Smith. Characterization of Al(Cr)N and Ga(Cr)N dilute magnetic semiconductors. *J. Magn. Magn. Mater.*, 290 - 291, Part 2(0):1395 – 1397, 2005.

[161] Y. Nishio, K. Ishikawa, S. Kuroda, M. Mitome, and Y. Bando. Formation of Cr rich nano-clusters and columns in (Zn,Cr)Te grown by MBE. *MRS Proceedings*, 1183:FF01–11, 2010.

[162] S. Caprara, V. N. Men'shov, V. V. Tugushev, P. M. Echenique, and E. V. Chulkov. Effect of carrier confinement on exchange coupling in dilute magnetic semiconductors with self-organized nanocolumns. *Phys. Rev. B*, 79:035202, Jan 2009.

[163] L. Zeng, E. Helgren, M. Rahimi, F. Hellman, R. Islam, B. J. Wilkens, R. J. Culbertson, and David J. Smith. Quenched magnetic moment in Mn-doped amorphous Si films. *Phys. Rev. B*, 77(7):073306, Feb 2008.

[164] D. Bougeard, N. Sircar, S. Ahlers, V. Lang, G. Abstreiter, A. Trampert, J. M. LeBeau, S. Stemmer, D. W. Saxey, and A. Cerezo. Ge_{1-x} Mn_x clusters: Central structural and magnetic building blocks of nanoscale wire-like self-assembly in a magnetic semiconductor. *Nano Lett.*, 9(11):3743–3748, 2009.

[165] L. Zeng, J. X. Cao, E. Helgren, J. Karel, E. Arenholz, Lu Ouyang, David J. Smith, R. Q. Wu, and F. Hellman. Distinct local electronic structure and magnetism for Mn in amorphous Si and Ge. *Phys. Rev. B*, 82:165202, Oct 2010.

[166] A. X. Gray, J. Minár, S. Ueda, P. R. Stone, Y. Yamashita, J. Fujii, J. Braun, L. Plucinski, C. M. Schneider, G. Panaccione, H. Ebert, O.D. Dubon, K. Kobayashi, and C. S. Fadley. Bulk electronic structure of the dilute magnetic semiconductor $Ga_{1-x}Mn_xAs$ through hard X-ray angle-resolved photoemission. *Nat Mater*, 11:957–962, 2012.

[167] M. Kobayashi, I. Muneta, Y. Takeda, Y. Harada, A. Fujimori, J. Krempasky, T. Schmitt, S. Ohya, M. Tanaka, M. Oshima, and V. N. Strocov. Unveiling the impurity band inducing ferromagnetism in magnetic semiconductor (Ga,Mn)As. arXiv:1302.0063 [cond-mat.mtrl-sci], 2013.

[168] J.-H. Yao, S.-C. Li, M.-D. Lan, and T.-S. Chin. Mn-doped amorphous Si:H films with anomalous Hall effect up to 150 K. *Applied Physics Letters*, 94(7):072507, 2009.

[169] J.-H. Yao, H.-H. Lin, Y.-L. Soo, T.-S. Wu, J.-L. Tsai, M.-D. Lan, and T.-S. Chin. Room-temperature anomalous Hall effect in amorphous Si-based magnetic semiconductor. *Applied Physics Letters*, 100(9):092404, 2012.

[170] J. M. Sullivan, G. I. Boishin, L. J. Whitman, A. T. Hanbicki, B. T. Jonker, and S. C. Erwin. Cross-sectional scanning tunneling microscopy of Mn-doped GaAs: Theory and experiment. *Phys. Rev. B*, 68:235324, Dec 2003.

[171] J. K. Garleff, C. Çelebi, W. Van Roy, J.-M. Tang, M. E. Flatté, and P. M. Koenraad. Atomically precise impurity identification and modification on the manganese doped GaAs(110) surface with scanning tunneling microscopy. *Phys. Rev. B*, 78:075313, Aug 2008.

[172] U. Gösele, H. Stenzel, T. Martini, J. Steinkirchner, D. Conrad, and K. Scheerschmidt. Self-propagating room-temperature silicon wafer bonding in ultrahigh vacuum. *Applied Physics Letters*, 67(24):3614–3616, 1995.